1 - Seismological Observations of Upper Mantle Anisotropy

2 - Source Spectra of Shallow Subduction Zone Earthquakes and their Tsunamigenic Potential

Thesis by
Jascha Polet
In Partial Fulfillment of the Requirements
for the Degree of
Doctor of Philosophy

California Institute of Technology
Pasadena, California
1999
(Submitted June 29, 1998)

Acknowledgments

I would like to thank the faculty, staff and especially my fellow students at the Seismo Lab for making my graduate years at the Seismo Lab an enjoyable experience.

I benefitted from being able to work with several great scientists, with some very different points of view on science and life in general. First of all, Hiroo Kanamori has an incredible insight into seismology and the Earth, and was always willing to answer my (mostly stupid) questions. I enjoyed working and talking with Paul Silver, who was enthusiastic, supportive and taught me not to run away from controversy. Don Anderson and Don Helmberger gave me pearls of wisdom from opposite sides of the seismic anisotropy debate.

I would also like to thank all my office mates over the years : Dave, Blair, Lianxing, Craig, Xi, Leo and Javier, for putting up with me and my opinions about basketball, Seinfeld, America, the Dodgers, the job market, and sometimes even seismology. Additional thanks go to Leo and Javier for watering my orchids when I wasn't around (again: sorry Leo for killing your plant when you were out of town..). I have had interesting discussions, conversations and movie goings with many people at the Lab : of-course my CS classmates Lupei, Igor and Lianxing (our project "discussions" could be heard on the other side of the building, but were great fun), Shingo, Xi (whose flow chart is still legendary), Paul, Mark & Martha (who disproved some of my preconceptions about MIT-ers and confirmed others), Anu, all the Love Waves softball players over the years and many others.

Of course my greatest thanks go to the people who put me on this Earth in the first place : my parents (alsnog bedankt daarvoor) en Hong Kie, who was incredibly supportive and has enriched my life in many ways.

Abstract

One of the most important developments in observational seismology in the last 10 years is the worldwide increase in the number of broadband instruments and seismic networks, as well as the improved access to the data-set that these seismometers provide. A data-set of this magnitude offers nearly unlimited possibilities for research into earthquake source processes and Earth structure. The work presented in this thesis involves the application of different methods to seismological recordings, as well as an interpretation and discussion of the results.

In Chapter 1, I take advantage of the very broadband nature and small spacing of the stations of TERRAscope, one of the first digital broadband seismic networks, to determine dispersion curves for long period surface waves. This enables us to invert for an upper mantle S-wave velocity model for southern California. The Rayleigh wave, SV, model is about 4% slower than the model developed for tectonic north America. If the correction for higher modes I performed on our Love wave data measurements is accurate, the resulting SH velocity model shows about 5% anisotropy (transverse isotropy) in the upper mantle beneath southern California.

In Chapter 2, I perform measurements of shear-wave splitting on a unique data-set obtained from temporary arrays located above the Nazca subduction zone in South America. Data from SKS, and local S-wave data from deep and intermediate depth earthquakes, were used to develop a model of the anisotropy in this region. The above slab component of anisotropy in the western region, where the slab is at a depth of about 300 km and up is oriented NS and its delay time is limited to about 0.3 sec. This direction agrees with the shortening direction of the Andes and is orthogonal to that predicted by a corner flow model. To the east, the stations have EW aligned fast directions and possibly sample the Brazilian craton. The below slab component samples a zone of EW aligned

anisotropy, as well as trench parallel aligned anisotropy. The trench parallel directions can be explained by the retrograde motion of the slab in south America, and I speculate that the EW direction could suggest a tear in the slab, or a local EW orientation because of local buckling of the slab under NS compression.

In Chapter 3 I use this same method for the data of the TriNet array. Here I find an overall pattern of consistent directions of the polarization direction of the fast SKS waves, the fastest P-wave velocities and the World Stress Map maximum horizontal compressive stress directions. This suggest that the pattern of anisotropy is generally uniform in the crust and lithospheric mantle, in a layer with an overall thickness of 100 to 150 km. The alignment of most fast directions can be explained by plate-tectonic, extensional and compressional events. We also examine the detailed lateral and vertical variations of anisotropy in this region.

Chapter 4 is focussed on the differences in source spectra and tectonic setting between tsunami earthquakes, which excite anomalously great tsunamis and 'regular' shallow subduction earthquakes. We find that these unusual events have several characteristics in common: low energy release at short periods, centroid location close to the trench, updip rupture, relatively small accretionary prism, sediment subduction and a well-developed horst and graben structure of the oceanic plate close to the trench. We speculate that these events can nucleate in an unusually shallow part of the subduction zone, where sediments normally exhibit stable sliding behavior, because of the contacts between the horsts and the overriding plate. Because the earthquakes are so shallow, and there is some sediment being subducted, part of the rupture goes through sediments, making the source process slow. The true displacement (and thus the tsunami height) of these events may be underestimated because the elastic constants of the fault zone are not taken into account when converting seismic moment into displacement.

Table of Contents

List of Figures

List of Tables

Chapter 1:

Upper Mantle Shear Velocities Beneath Southern California Determined from Long-Period Surface Waves

Abstract

We used long period surface waves from teleseismic earthquakes recorded by the TERRA-scope network to determine phase velocity dispersion of Rayleigh waves up to periods of about 170 sec and of Love waves up to about 150 sec. This enabled us to investigate the upper-mantle velocity structure beneath southern California to a depth of about 250 km. Ten and five earthquakes were used for Rayleigh and Love waves, respectively. The observed surface wave dispersion shows a clear Love/Rayleigh wave discrepancy which can not be accounted for by a simple isotropic velocity model with smooth variations of velocity with depth. Separate isotropic inversions for Love and Rayleigh wave data yield velocity models which show up to 10% anisotropy (transverse isotropy). However, tests with synthetic Love waves suggest that the relatively high Love wave phase velocity could be at least partly due to interference of higher mode Love waves with the fundamental mode. Even after this interference effect is removed, about 4% anisotropy remains in the top 250 km of the mantle. This anisotropy could be due to intrinsic anisotropy of olivine crystals or due to a laminated structure with alternating high and low velocity layers. Other possibilities include: upper mantle heterogeneity in southern California (such as the Transverse Range anomaly) may affect Love and Rayleigh wave velocities differently so that it

yields the apparent anisotropy; higher mode Love wave interference has a stronger effect than suggested by our numerical experiments using model 1066A. If the high Love wave velocity is due to causes other than anisotropy, the Rayleigh wave velocity model would represent the southern California upper-mantle velocity structure. The shear velocity in the upper mantle (Moho to 250 km) of this structure is, on average, 3 to 4% slower than that of the TNA model determined for western North America.

Introduction

The seismic velocities in the upper mantle beneath the western U.S. are generally considered to be lower than average (e.g., the TNA model of Grand and Helmberger, 1984). In a broad sense, southern California is categorized as "western U.S." but it is unclear whether its upper-mantle structure is indeed similar to that represented by, for instance, the TNA model. There are in fact different lines of evidence which suggest that the southern California upper mantle has significant structural heterogeneities. Large-scale mantle high velocity zones such as the Transverse Ranges anomaly (Raikes, 1978; Hadley,1978; Hadley and Kanamori, 1979; Humphreys et al., 1990) and the Isabella anomaly (Aki,1982; Jones et al., 1994) have been found.

To investigate the upper mantle structure beneath southern California further, it is necessary to determine the structure to a relatively large depth (200 km) on the spatial scale of southern California. A useful approach to this problem is the surface wave phase velocity method. The dispersion of surface waves has been widely used to determine seismic velocity structures in the Earth's crust and mantle. In previous studies in southern California, Press (1956) and Ewing and Press (1959) used Rayleigh waves to determine crustal structures. Brune and Dorman (1963) used both Rayleigh and Love waves to study the crust and upper mantle structure beneath the Canadian shield and McEvilly (1964) determined a crust-upper mantle structure for central U.S. by inverting Rayleigh and Love

wave dispersion curves.

Due to the limited quality of the data, the earlier measurements of surface wave phase velocities in southern California were limited to periods shorter than 27 sec. Recently, Wang and Teng (1994) determined Rayleigh wave phase velocities in southern California to a period of 100 sec using broadband data obtained from TERRAscope. Stange and Friederich (1993) determined the dispersion of fundamental mode Rayleigh waves in southern Germany in the frequency range 4-50 mHz from data recorded at a broadband network. The purpose of the present study is to provide new constraints on the average velocity structure of southern California by determining surface wave phase velocities for periods up to 170 sec. This increased period range is critically important for exploring deeper structures. The main objective is to determine the overall velocity structure in the top 250 km of the upper mantle for both Rayleigh and Love waves. In view of the limited resolution of surface wave methods, we do not intend to resolve the details of the vertical variation of velocities nor do we attempt a tomographic inversion for the lateral variations within the network.

Method

In this study we use a traditional method to determine the phase velocities (e.g.,Press 1956, Aki 1961), which we will describe briefly. First the phase travel times are calculated as a function of period. This is done by computing the Fourier Transform of the surface wave train $x(t)$ for each station i:

$$\widehat{x}_i(\omega) = \int\limits_{-\infty}^{+\infty} x_i(t) \cdot e^{-i\omega t} dt$$

where ω is the angular frequency.

The phase, $\psi_i(\omega)$, of the signal is then determined by:

$$\psi_i(\omega) = \arctan\frac{Im(\widehat{x}_i(\omega))}{Re(\widehat{x}_i(\omega))}$$

The phase travel time, $t_i(\omega)$, can consequently be calculated using:

$$t_i(\omega) = -\frac{\psi_i(\omega) - \omega \cdot (t_{s_i} - t_0) + 2\pi N}{\omega}$$

where : t_{si} = starting time of surface wave signal

t_0 = origin time of event

N is an integer that can be determined unambiguously from the approximate phase velocity known for the area. When the t_i's for all stations are evaluated, the phase velocity $C(\omega)$ and the propagation azimuth $\Phi(\omega)$ within the network can be determined from the following set of equations in the least squares approximation, with the main assumption that we are dealing with a plane wave within the network.

$$\Delta_i \cdot \cos\phi_i \cdot \frac{\cos\Phi(\omega)}{C(\omega)} + \Delta_i \cdot \sin\phi_i \cdot \frac{\sin\Phi(\omega)}{C(\omega)} = t_i - t_r \quad [1]$$

$$(i=1,...,N_s-1)$$

where : Δ_i = distance of station i measured from a reference station r

ϕ_i = azimuth of station i measured from station r

t_r = phase arrival time at reference station

and N_s = number of stations
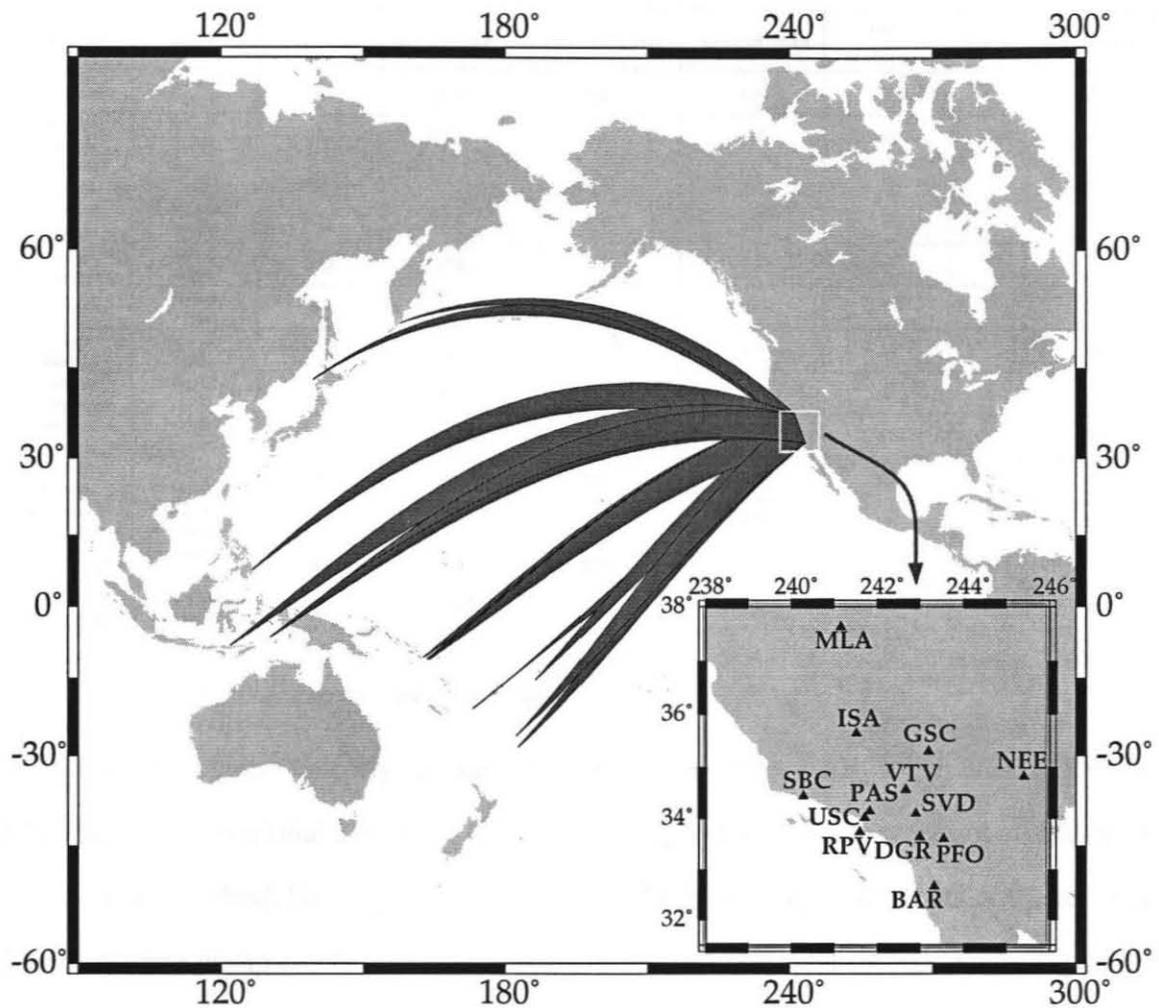
Figure 1: Great circle paths of the events used in this study. Insert shows location of TERRAscope stations in southern California, exact locations can be found on www-page http://www.trinet.org/trinetmap/station_info.list

Data Selection

The data we used for this study are long period velocity records provided by the TERRAscope network located in southern California. The locations of the stations in the network are given in Figure 1 (insert). Out of the 13 stations, PAS, GSC, PFO, SBC, ISA and BAR use the Streckeisen STS-1 seismometer and the stations SVD, USC, MLA, VTV, NEE, RPV and DGR use the Streckeisen STS-2. We equalized the response of STS-2 to STS-1

location	date	latitude	longitude	back-azimuth	magnitude	no. stations	Love	Rayleigh
Sea of Japan	July 7 1993	43.2	139.4	312	7.6	5		X
Vanuata Islands	June 30 1993	-21.1	173.1	240	6.7	10		X
Kermadec Islands	June 18 1993	-28.4	-177.2	239	6.7	11		X
Solomon Islands	June 12 1993	-10.7	162.7	255	6.1	6		X
East coast of Kamchatka	June 8 1993	51.3	157.8	314	7.1	8,7	X	
Mariana	June 6 1993	6.0	146.4	286	6.5	9		X
Tonga Islands	May 16 1993	-15.2	-173.5	236	6.7	10		X
Mindanao, Philippines	May 11 1993	7.8	126.6	292	6.6	3	X	
Solomon Islands	March 6 1993	-11.0	163.5	254	6.6	6,7	X	X
Santa Cruz Islands	March 6 1993	-10.9	164.2	254	7.0	6,6	X	X
South of Fiji Islands	March 6 1993	-26.3	-177.6	230	6.7	5		X
Banda sea	December 20 1992	-6.5	130.3	277	7.1	5	X	
Flores, Indonesia	December 12 1992	-8.2	121.9	280	7.5	5		X

Table 1: Events used in this study.

so that accurate phase velocity measurements could be made. BAR, VTV, NEE, RPV and

DGR became operational during the course of this study so their data were not available for

all the events studied. For Rayleigh waves we used the vertical components of the records.

The transverse components obtained by rotation of the horizontal records according to the

source-receiver azimuth were used for the Love wave analysis.

About 15 large events with long oceanic paths to the TERRAscope network were analyzed.

Only shallow events were used to minimize contamination of the fundamental mode with

higher mode surface waves. We determined Rayleigh and Love wave phase velocities for

ten and five of these events (Figure 1 and Table 1), respectively. We show a representative

example of these data in Figure 2. Data were rejected if the errors or fluctuations in the

determined dispersion curves were large. Two main reasons were found for these

problems: a source-receiver azimuth near a nodal direction and/or a large deviation from

the plane wavefront approximation as used in this method. A near-nodal source-receiver

azimuth can cause the source phase of surface waves to vary across the network to such an

extent that it impedes accurate phase velocity determination. We examined the shape of the

Santa Cruz Islands, Δ=86°, back-azimuth=254°, magnitude=7.0
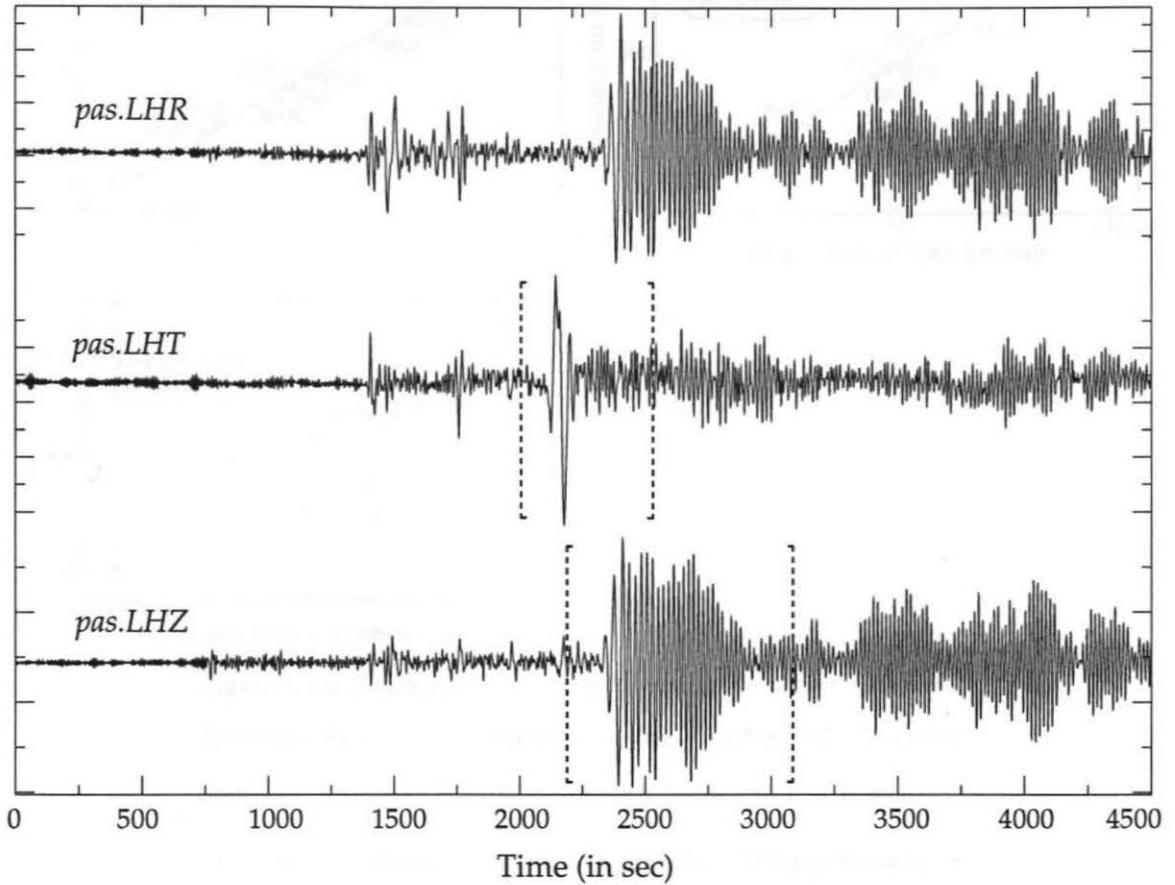
Figure 2: Long period velocity records from station PAS for the event near the Santa Cruz Islands (Table 1). Vertical lines indicate time windows used in the determination of phase velocity dispersion.

wavefront (for different frequencies) by first calculating the distance between the stations parallel to the direction of the ray as calculated in [1]. Subsequently we performed a linear regression on these points as a function of differential phase arrival time. The fit of these points on a straight line, as indicated by the correlation coefficient, determines the deviation of the wave front from a plane. Over 95% of the Rayleigh wave phase measurements used in this study were determined to have correlation coefficients greater than 0.9975 (a correlation coefficient of 1 denoting perfect fit on a straight line). For the Love wave measurements, over 90% of the measurements used in the inversion had a correlation coefficient greater than 0.9950. Figure 3 shows typical examples for the event
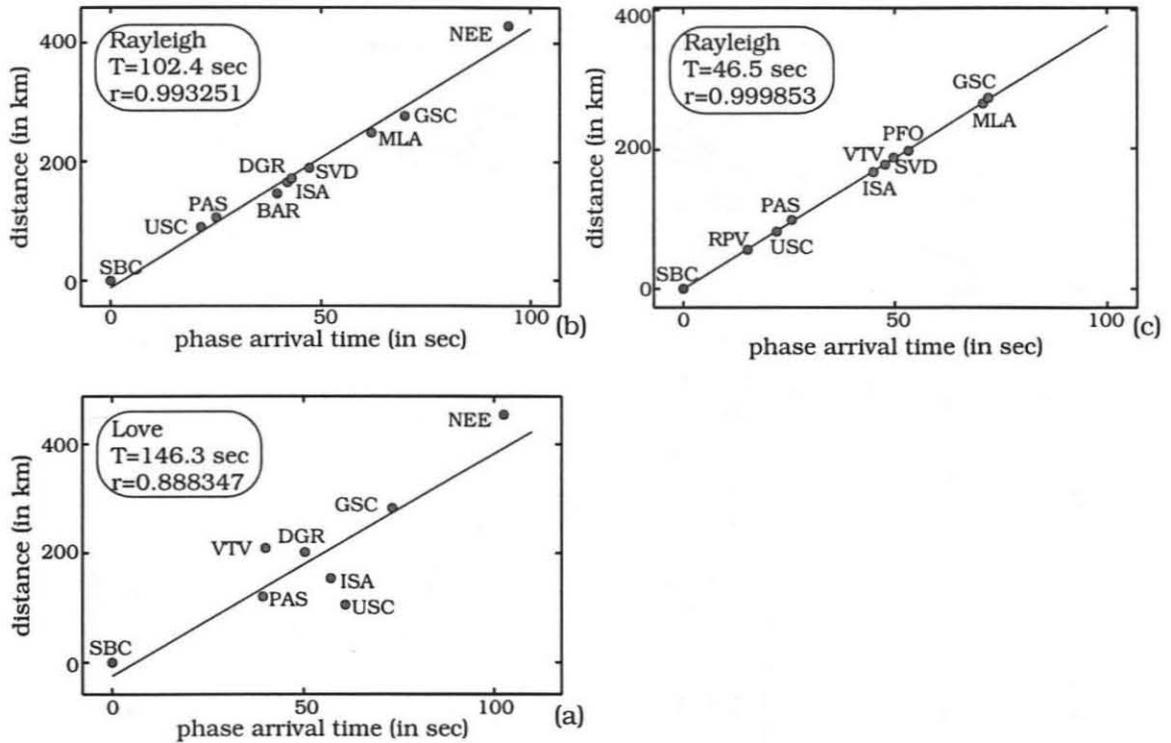
Figure 3: (a) Distance along ray direction vs. phase arrival time for Love wave data from an event near the Vanuatu Islands (Table1) for a period of 146.3 sec. The cross-correlation coefficient, r, is 0.8883.

(b) Same for Rayleigh wave data for a period of 102.4 sec. Value of r is 0.9932.

(c) Same for Rayleigh wave data for a period of 46.5 sec for the event near Tonga. R is 0.9999.

near the Vanuatu Islands (Table 1,(a) and (b)) and the event near Tonga in (c). In Figure 3(a), the Love wave measurements show a strong deviation from a plane wavefront for this event, with a correlation coefficient of only 0.8883. This could be due to the fact that Love waves are more sensitive to near surface structures (shallow lateral inhomogeneities) and probably suffer more from refraction effects from the continental margin. This data clearly shows an unacceptable deviation from the plane wave approximation (which is also obvious in the large standard error of the measured phase velocities) and thus the resulting dispersion curve was not used in our inversion. The Love wave data retained for the inversion do not have this problem. Figure 3(b) shows one of the worst fits on a plane wave for
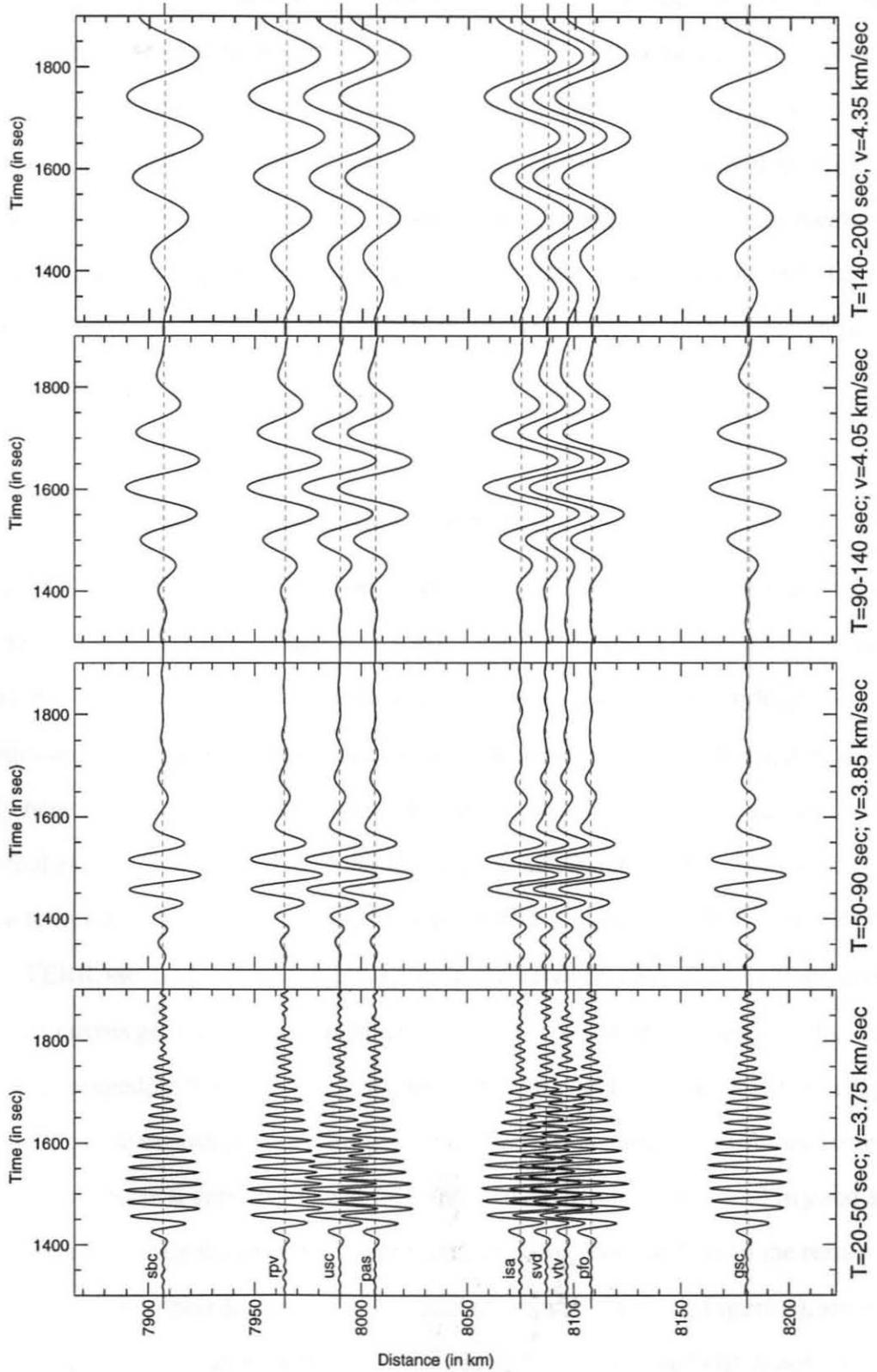
Figure 4: Reduced record sections for bandpass filtered seismograms.

the Rayleigh wave measurements which were used in this study. In Figure3(c) a more typical example is given, representative of over 95% of the used measurements. The data clearly fit a plane wave very well. We also checked for amplitude variations between the different stations and found that they very rarely exceed 10%. Coherence of the waveforms across the network is very good for all periods, and especially for periods greater than 50 sec, as illustrated by Figure4. Based on the results of these investigations, we believe that accurate determination of phase velocities in this region is possible, even though lateral heterogeneities may exist.

Data Analysis: Phase Velocity Measurements

The phase velocity values we determined are shown in Figure 5. The standard error is about ±0.07 km/sec for most data points. Love wave velocities for periods longer than 150 sec and shorter than 50 sec exhibit large scatter and are questionable. Rayleigh wave velocities are generally well-determined for periods between 20 and 180 sec, although they usually have larger errors for periods shorter than 50 sec. The dispersion curves for the individual events display some irregular fluctuations as a function of period. This is proba-bly due to interference of waves caused by the lateral heterogeneities between the source and the TERRAscope network as well as within the network, since the fluctuations of the dispersion curves generally coincide with (albeit small) deviations in the great circle direc-tion (rarely exceeding 5 degrees) and smaller correlation coefficient r for the fit to a plane wave of the phase measurements. This pattern of fluctuation varies for different events, but the average dispersion curves obtained from the different events are overall in good agree-ment (generally falling within one standard error of each other), and when the results from all the events are averaged, a smooth dispersion curve was obtained (Figure 6), showing that the effects of these lateral heterogeneities are probably averaged out. Since our objec-tive here is to determine the gross structure, rather than the details, in Figure 6 we first
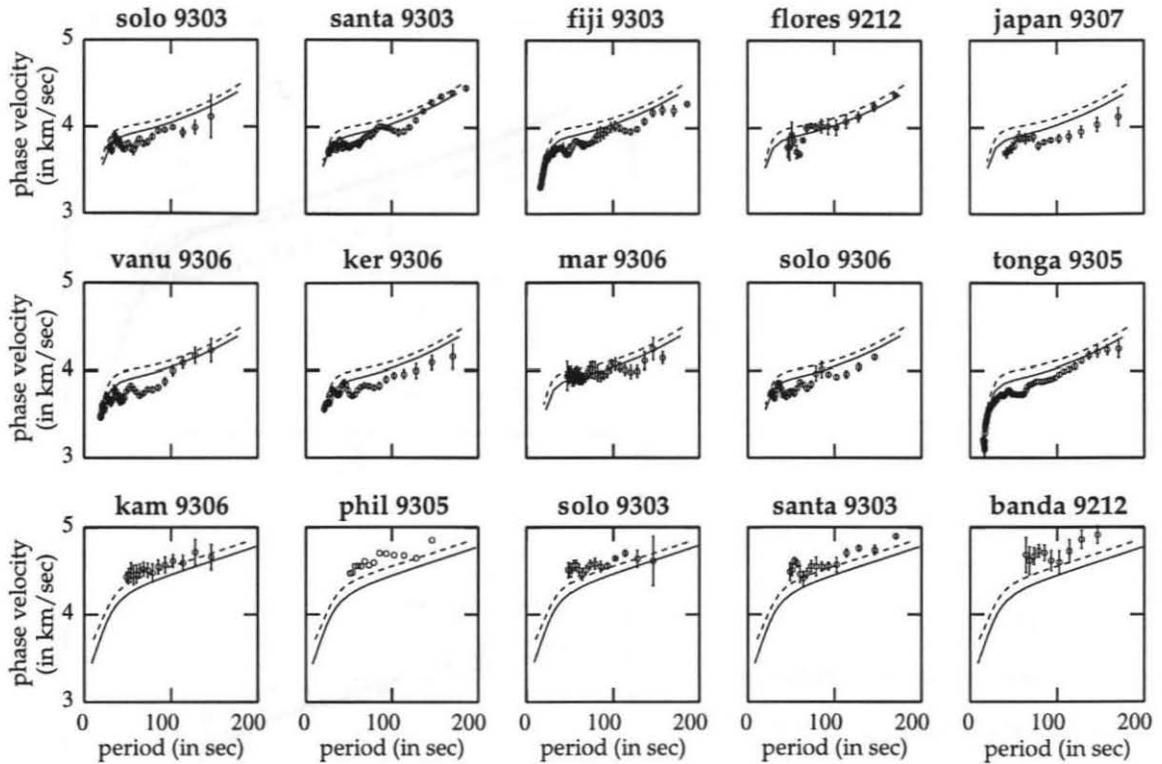
*Figure 5: Measured phase velocity values. Open circles denote Love
wave values, dark circles, Rayleigh wave values. Solid and dotted lines
indicate reference dispersion curves calculated for the TNA and the
Gutenberg model. Error bars show standard error.*

compare the observed dispersion curves with those of several standard continental models
to demonstrate the overall differences. The models used here are the Gutenberg model
(continent), JB model (continent) (parameters for both the Gutenberg as well as the JB
model were obtained from Dorman, Ewing and Oliver, 1960), SNA model (shield, Grand
and Helmberger, 1984) and the TNA model (western North America, Grand and
Helmberger, 1984). The Rayleigh wave velocities are lower than those calculated for the
Gutenberg model, the JB model and the SNA model. They are also significantly lower than
the phase velocities predicted by the TNA velocity model, with a low velocity crustal
model used for the top 32 km.

The Love wave phase velocity measurements have slightly larger errors but also are in
good agreement for the different events. In contrast to the Rayleigh waves, the average
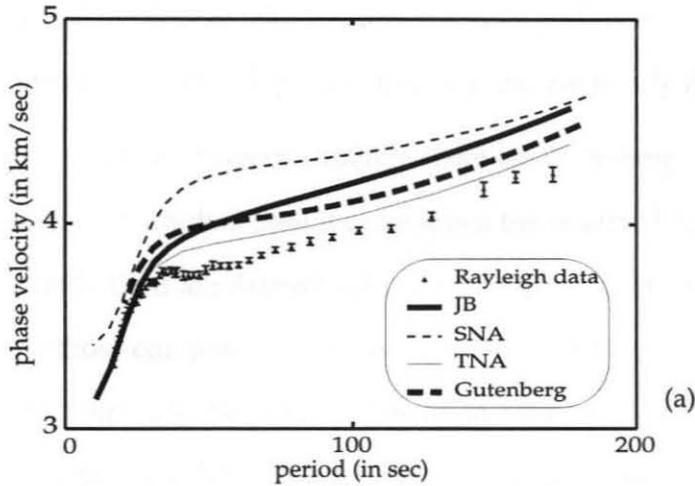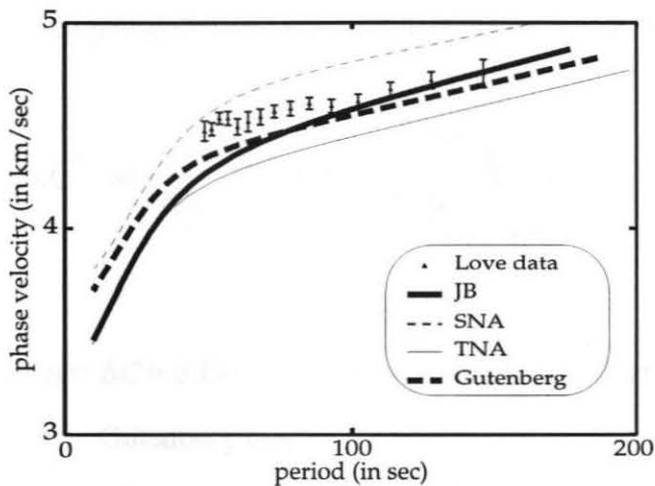
Figure 6: (a) Average Rayleigh
wave dispersion measurements and
dispersion curves calculated for JB,
SNA, TNA and Gutenberg velocity
models.

(b) Same for Love wave
dispersion.

values of Love wave phase velocities are clearly higher than those predicted by the TNA

model (Figure 6b) and are in the same range as those for the standard continental models

like the Gutenberg and JB models.

For one of the events (located in the Santa Cruz Islands) we could determine the phase

velocity using the G2 wave, coming from the opposite azimuth. The result is very similar

to that obtained from the G1 data for a period range of 80 to 150 sec (for smaller periods

the G2 wave contained substantial non-plane wave energy).

Inversion Method

Since, as mentioned earlier, our primary interest here is in the average velocity structure,

we use the simple least squares inversion method by Takeuchi et al. (1964), with the emphasis on obtaining smooth structures. We briefly describe the method in the following.

In essence, a reference structure (here the Gutenberg model) is chosen first. Then this model is perturbed until it can explain the observed dispersion curves satisfactorily. The perturbations are determined from the difference between the observed phase velocities and those computed for the reference structure using partial derivatives of phase velocity with respect to the S-wave velocity in each layer. We do not perturb density and P-wave velocity since the partial derivatives of phase velocity with respect to these parameters are relatively small. Then we solve for the following set of equations (one for each period for which phase velocity measurements have been made):

$$\Delta C = \sum_i \Delta \beta(r_i) \cdot \left(\frac{\partial C}{\partial \beta} \right)_{\alpha, \rho} (r_i) \quad (i = 1, \ldots, N_l)$$

where: ΔC = difference in phase velocity at a given period from the reference model (here: Gutenberg model)

$\Delta\beta(r_i)$ = resulting difference in velocity in layer i with Gutenberg model

N_l = number of layers

Inversion Results

As shown in Figure 5, none of the existing models can explain the averages of the Love and Rayleigh wave phase velocity measurements simultaneously. In general, the observed Love wave phase velocities tend to be faster than expected from the Rayleigh wave velocities. As Babuska and Cara (1991) demonstrated, this is a fairly commonly observed trend for many places in the world.
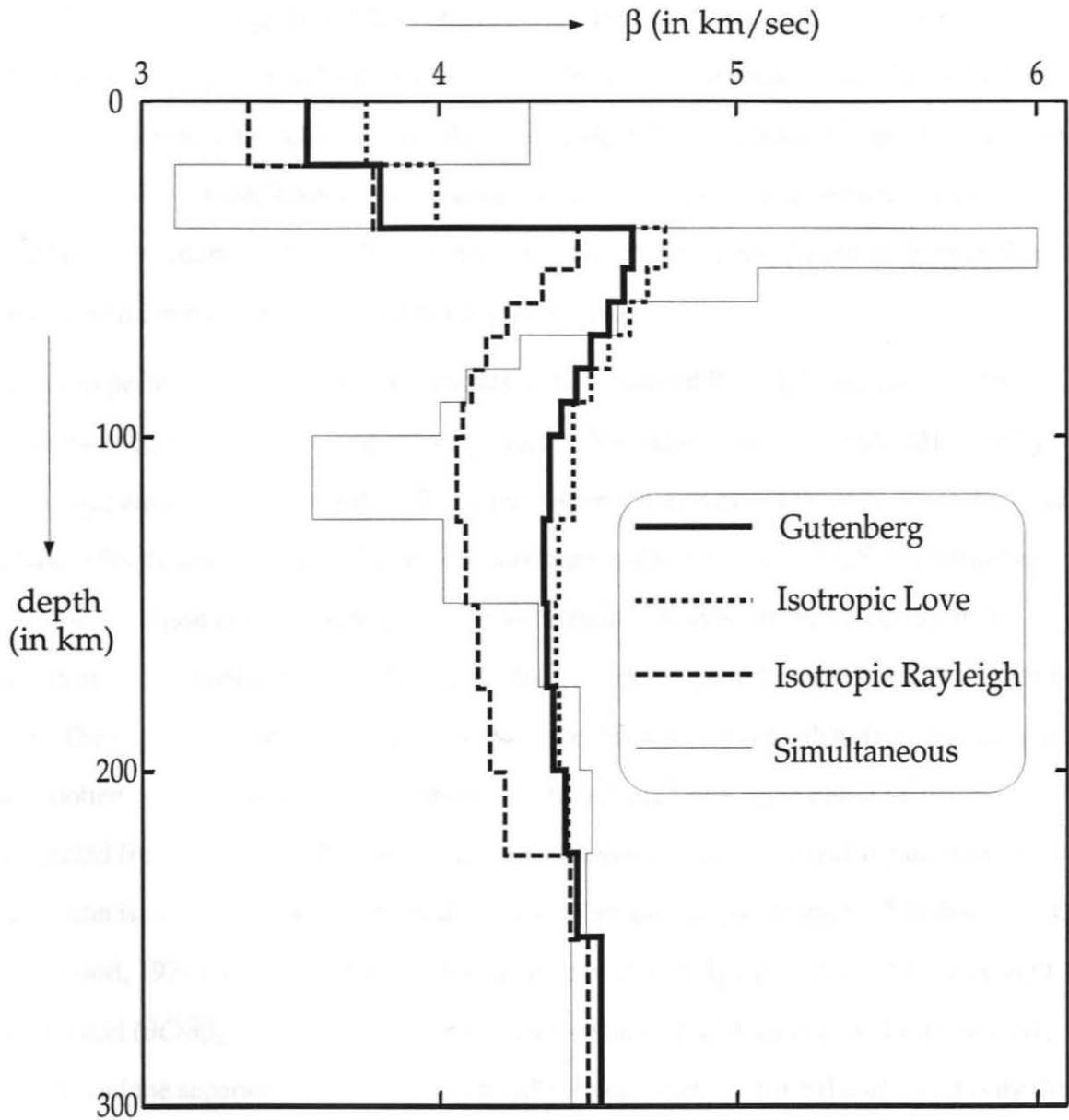
Figure 7: Shear wave velocity-depth models. Thick solid line denotes Gutenberg model, thin solid line indicates the results of the simultaneous inversion of Rayleigh and Love wave phase velocities and dotted lines show the results of the independent isotropic inversions.

An attempt to explain the Love and Rayleigh wave phase velocities (over a period range of 49-146 and 17-171 sec respectively) simultaneously with an isotropic model leads to an unrealistic velocity model as shown in Figure 7. Although we also used the shorter period (20-50 sec), noisier, Rayleigh wave phase velocities in this inversion, leaving them out

would only have a negligible effect on the gross structure. This model exhibits strong fluctuations of velocity with depth even though the inversion was damped. The relatively high velocities near the top of the mantle are a result of the greater sensitivity of Love wave phase velocity for shallower layers whereas the low velocity zone at greater depths is required to explain the slower Rayleigh wave velocity. This model is not realistic and still does not fit the measured Love wave velocities well.

We then performed independent inversions of the observed Rayleigh and Love wave dispersion curves. The resulting velocity models (SV velocity for Rayleigh, SH velocity for Love) are also shown in Figure 7 and the dispersion curves in Figure 8. The calculated phase velocity curves fit the data of both Rayleigh and Love wave well. Some damping was used in these inversions, to minimize the velocity fluctuations between adjoining layers and to minimize the velocity change for the lower layers, for which the resolution is low. The significance of the Love/Rayleigh wave discrepancy is evident from the dashed and dotted dispersion curves in Figure 8, which indicate Love wave phase velocities predicted from the Rayleigh wave model and vice versa. The performed separate isotropic inversion is not strictly correct when dealing with an anisotropic structure (Mitchell, 1984; Kirkwood, 1978). However, for the period range of this study, $(\partial C/\partial \beta_{SH}) \approx 0$ for Rayleigh waves and $(\partial C/\partial \beta_{SV}) \approx 0$ for Love waves (Figures 3 and 12 of Anderson and Dziewonski, 1982), and the separate inversion would yield correct structures for SH and SV, if only the S-wavevelocity is anisotropic. In isotropic media, P-wavevelocity has little effect on Rayleigh wave phase velocity for the depth and period ranges concerned here. In anisotropic media, Rayleigh wave phase velocity depends on the two partials with respect to vertical and horizontal P-wave velocity, $(\partial C/\partial \alpha_{PH})$ and $(\partial C/\partial \alpha_{PV})$. However, the P-wave partials are only in the range of about 20% of the S-wavepartial (Figure12, Anderson and Dziewonski, 1982), so that our conclusion on SH/SV would not be significantly affected.

A difficulty in the determination of Love wave phase velocities is the interference of higher modes with the fundamental modes (Thatcher and Brune, 1969). To avoid the
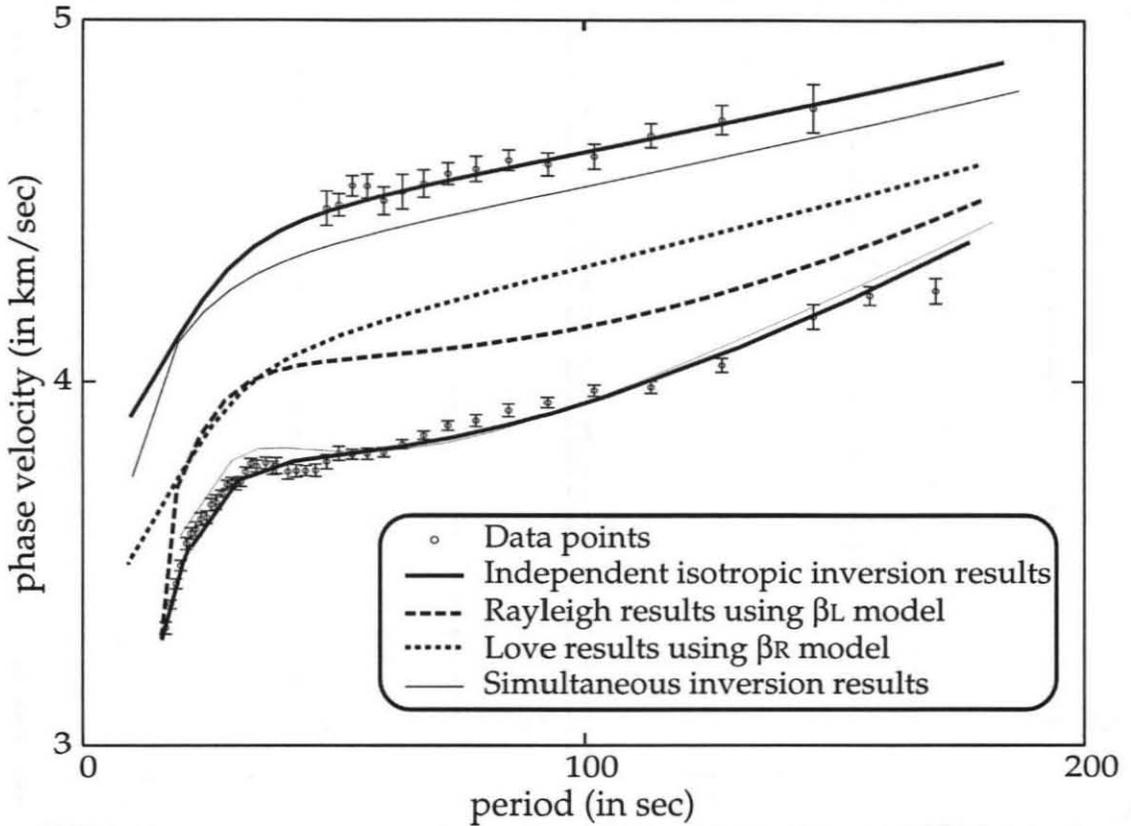
Figure 8: Observed (dot-bar symbols) and modelled (full and dotted lines) phase velocities for southern California. The error bars indicate the standard deviation of the measurements. The dotted lines show velocities predicted from the inappropriate model (β_L for Rayleigh waves and vice versa). The thick solid line indicates the results of the independent isotropic inversion and the thin solid line shows the results predicted by the simultaneous isotropic inversion.

contamination of the fundamental mode with higher mode Love waves, we chose shallow events with long paths (Knopoff (1983, 1972)) to TERRAscope. To examine the possibility of higher mode interference, we carried out synthetic tests. By mode summation, using the 1066A velocity model (Gilbert and Dziewonski, 1975), we produced synthetic seismograms for those events which were used in our Love wave phase velocity calculation. The results for two of these events are shown in Figure 9 ((a) and (b)); these are representative of all the events. As can be clearly seen in these synthetic seismograms, higher modes are present in the synthetics for Love waves in the same time window in which the fundamen-
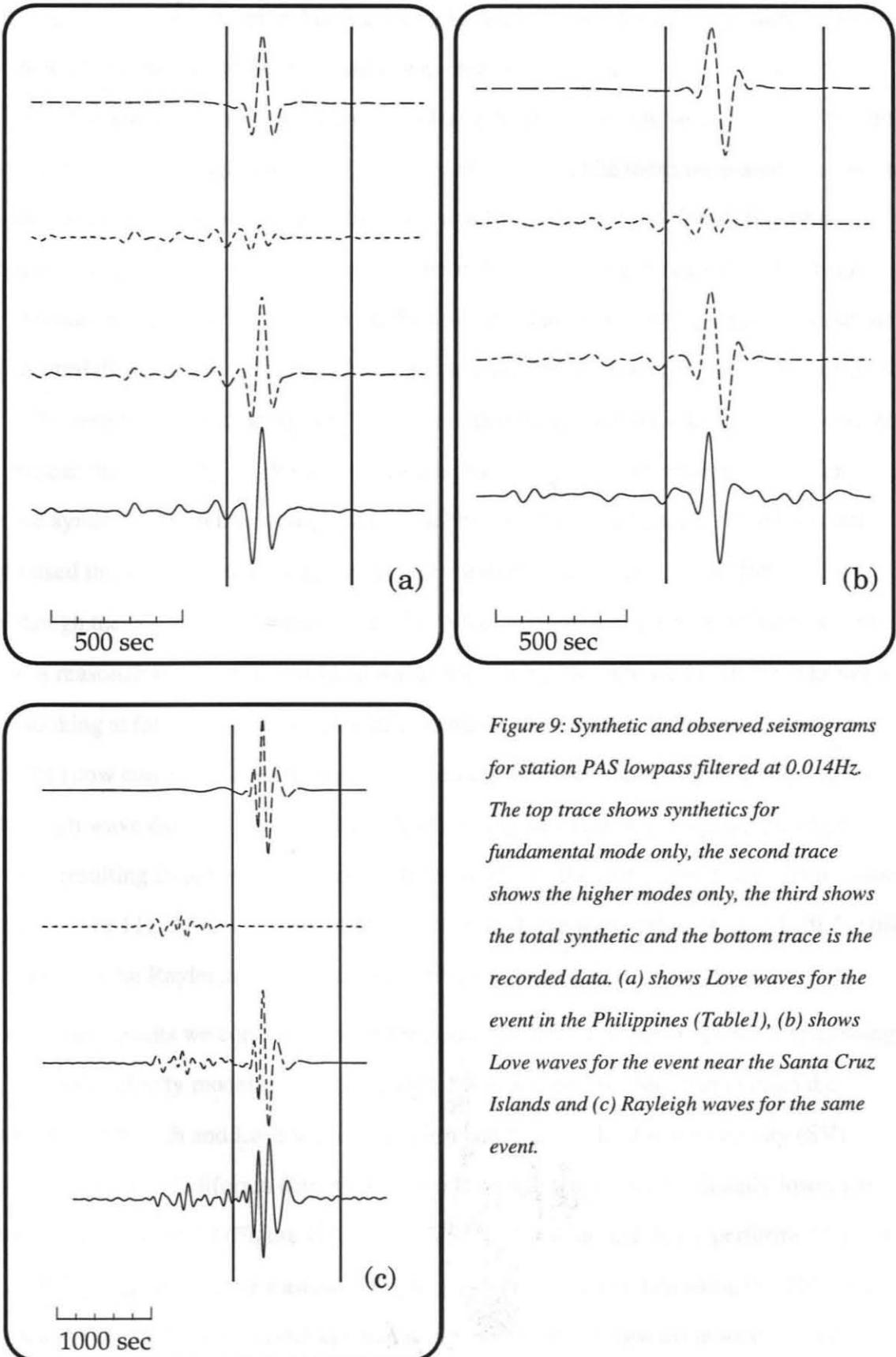
Figure 9: Synthetic and observed seismograms for station PAS lowpass filtered at 0.014Hz. The top trace shows synthetics for fundamental mode only, the second trace shows the higher modes only, the third shows the total synthetic and the bottom trace is the recorded data. (a) shows Love waves for the event in the Philippines (Table1), (b) shows Love waves for the event near the Santa Cruz Islands and (c) Rayleigh waves for the same event.

tal mode is expected to arrive. For Rayleigh waves, however, the higher modes arrive outside of this time window. By comparison of these synthetic seismograms with the recorded seismogram (lowpassed at 0.0143 Hz or 70 sec in period), we can see that the data does indeed contain higher modes. Synthetic seismograms like these were used to compute dispersion curves for the fundamental mode and for the total signal for all five of the events, using the same time windows as were used for the data. As expected, the resulting dispersion curves were the same for all the fundamental mode seismograms. Because the epicentral distance is not the same for all the events, the interference effects also differ, so that the results for the seismograms which included the higher mode Love waves were not identical, but very similar. We subtracted the phase velocities determined for fundamental mode synthetics from the average phase velocities obtained using total mode summation and used these values as a correction for our measured Love wave dispersion results. Although the correction is dependent on the velocity model used, we think that this correction is reasonable, since the computed waveform synthetics agree well with the data and we are looking at fairly long period (greater than 60 sec) wave here. We repeated the inversion for the (now corrected) Love wave data separately and simultaneously with the original Rayleigh wave data and the results are shown in Figures 10 and 11. Again, the velocity model resulting from the simultaneous inversion shows fluctuations and unrealistic velocities (Figure 11), though to a lesser degree; also the Love wave velocity model ($\beta L2$) still does not fit the Rayleigh wave data and vice versa (Figure 10).

From these results we conclude that, if the correction found by these synthetic tests using the 1066A velocity model is correct, around 4% anisotropy is needed to explain the measured Rayleigh and Love wave dispersion and that the shear wave velocity (SV) beneath southern California determined from Rayleigh waves is significantly lower than that of the TNA model (Figure 11). To confirm this last conclusion, we performed forward modelling and inverted the measured Rayleigh wave dispersion data using the TNA model instead of the Gutenberg model as our starting model. In the forward modelling, we
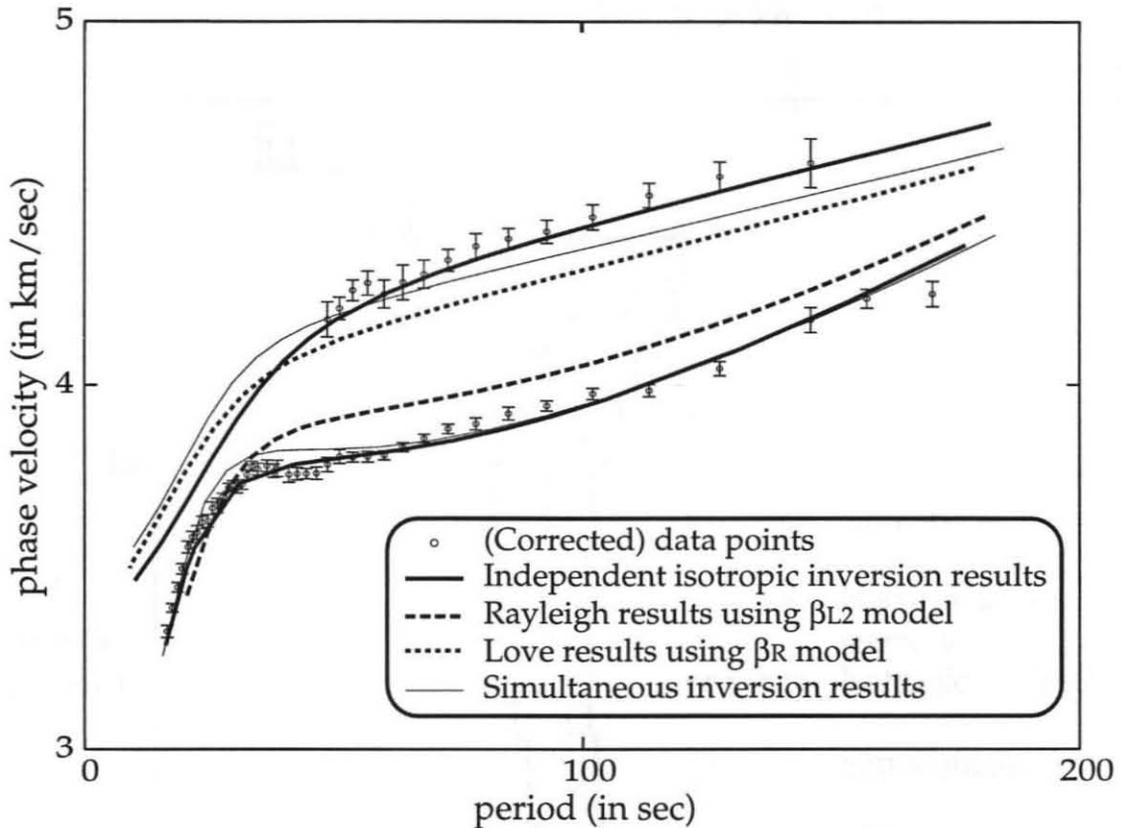
Figure 10: Same as Figure 8. Corrected Love wave data are used.

constructed three different velocity models from the TNA model by reducing the shear

velocity by 2, 4 and 6% between Moho and 250 km. These models are called TNA-2%,

TNA-4% and TNA-6%, respectively (Figure 12). Figure 13 shows the dispersion curves

calculated using these models. It is evident that our data can not be explained by TNA, or

even the TNA -2% model, but on average the data lies somewhere in between the values

predicted by the TNA -2% and -4% models.

We repeated our inversion using the Rayleigh wave dispersion data, this time with TNA as

our starting model. The resulting velocity model (Figure 12) is very similar to that obtained

using the Gutenberg model as our starting model, although the low velocity is less

pronounced at greater depths. These two models obtained from two different starting mod-

els as well as the models derived from the TNA model strongly suggest that the shear (SV)

velocity in the upper mantle beneath southern California is on average 3 to 4% slower than
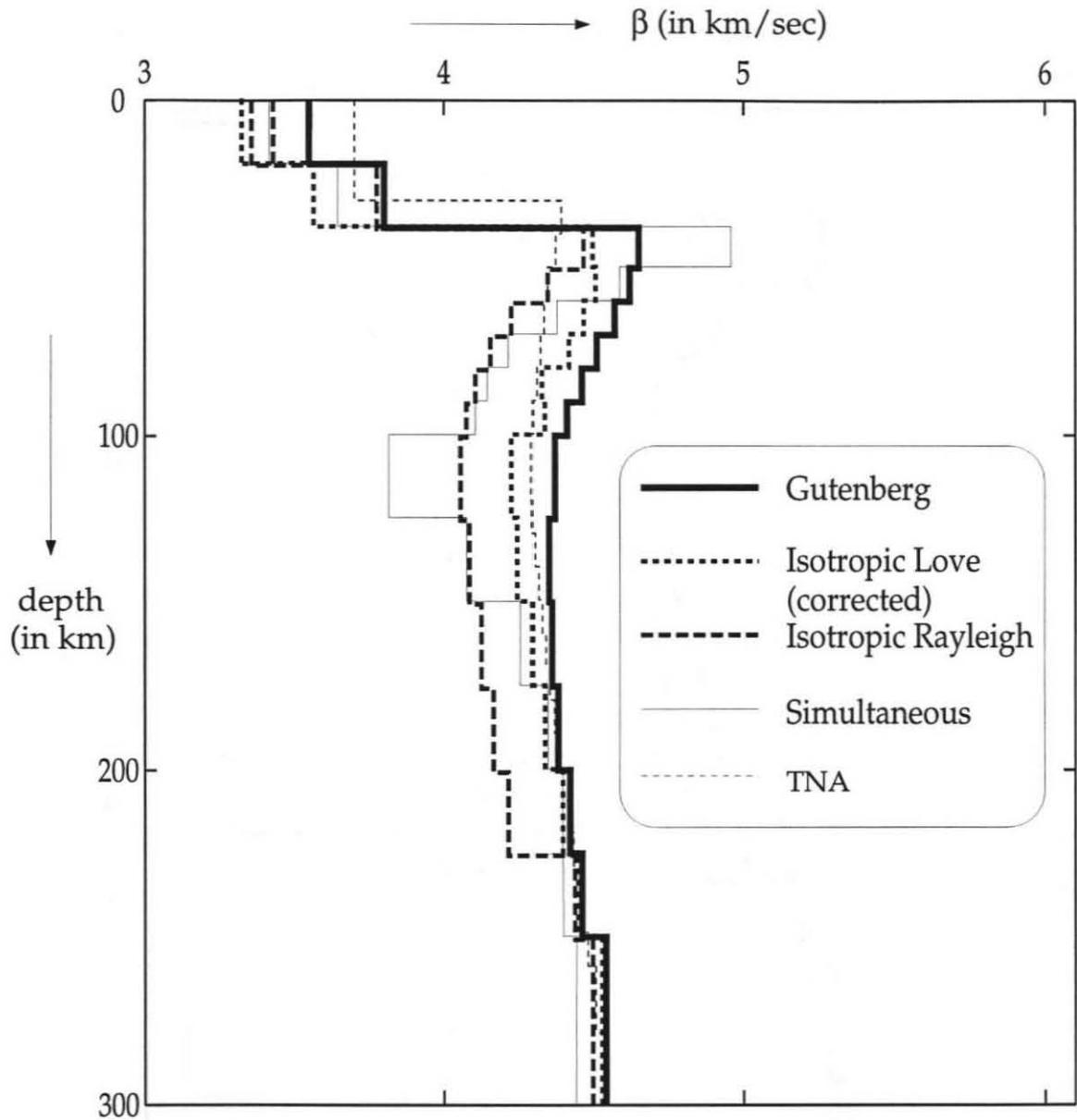
Figure 11: Same as Figure 7. Corrected Love wave data are used.

the TNA model that represents western North America.

Also, the relatively high Love wave velocity leads to an SH/SV discrepancy of about 4%. Note that we did not invert for η or P-wave anisotropy. If we include P-waveanisotropy, the required S-waveanisotropy could be somewhat smaller. However, as mentioned earlier, since the P-wavepartials are considerably smaller than the S wave partial, the overall conclusion on the SH/SV discrepancy would remain unchanged.
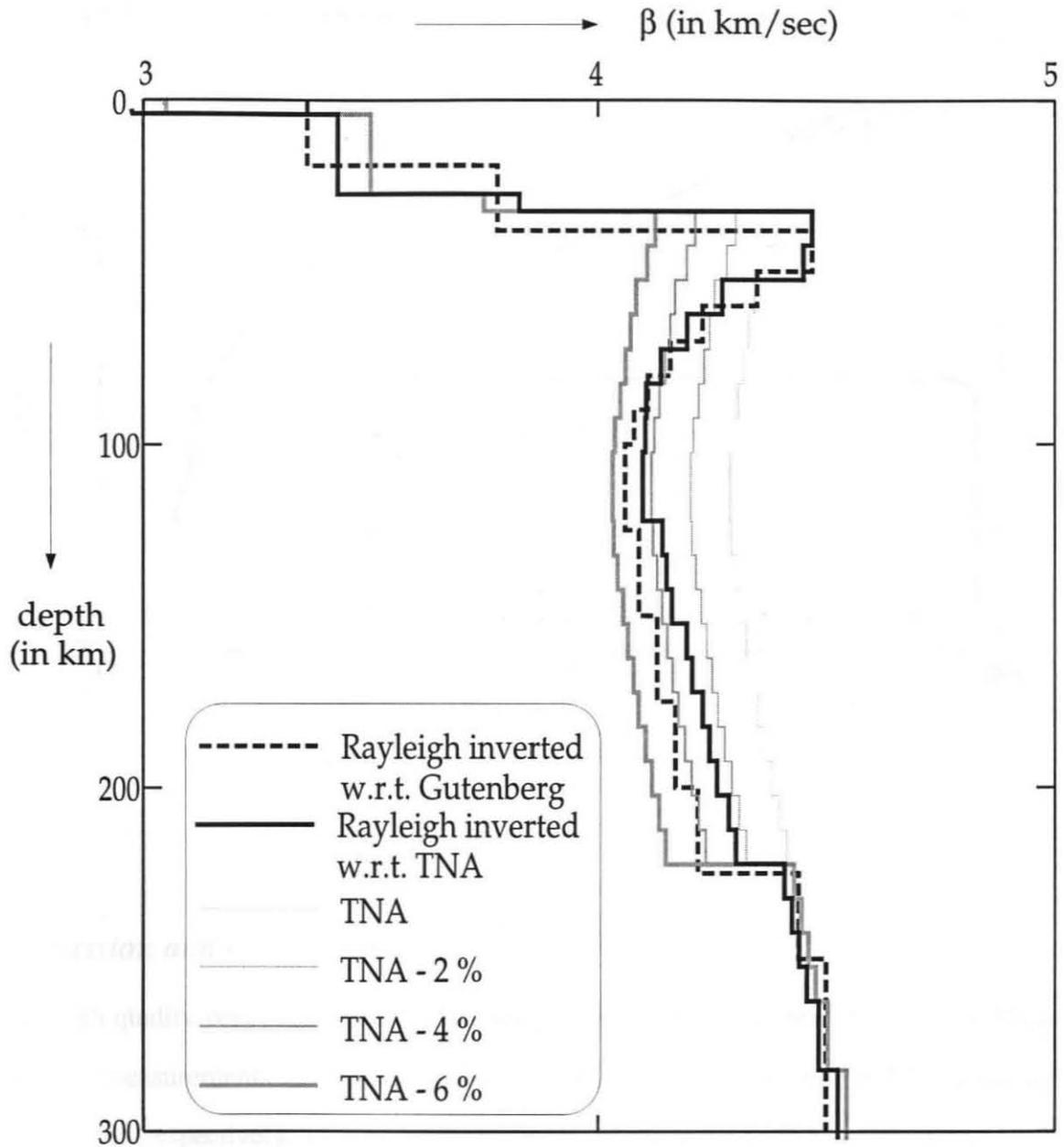
Figure 12: Shear wave velocity-depth models. The grey lines show the TNA model and the models constructed by reducing β by 2,4 and 6% from the TNA model between crust and 225 km. Also shown are the two inversion results: one with respect to Gutenberg (thick solid line) and the other with respect to TNA (thick dashed line).
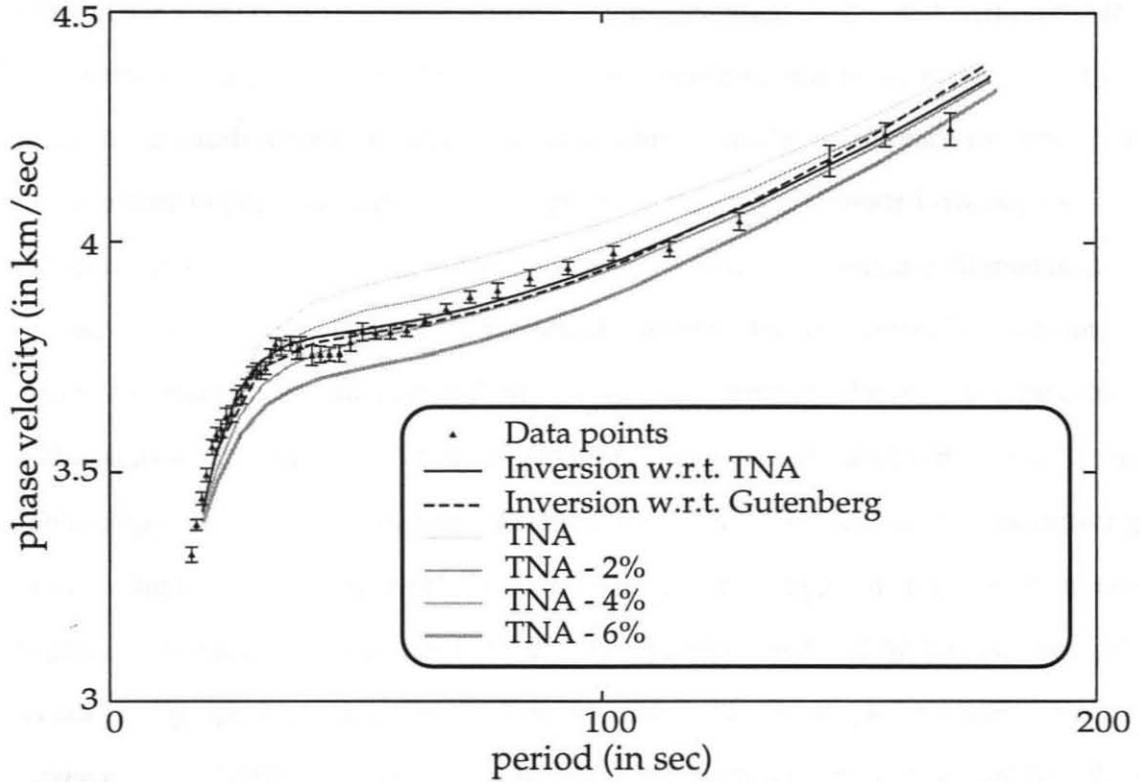
Figure 13: Dispersion curves for models shown in Figure 12, same annotation.

Discussion and Conclusions

The high quality very broadband TERRAscope data enabled us to perform accurate phase velocity measurements of Rayleigh and Love waves over a period range of 17-171 sec and 49-146 sec, respectively. The results for different events agree well, warranting an inversion for the average velocity beneath southern California down to a depth of around 250 km. It was not possible to explain Rayleigh and Love wave phase velocities simultaneously using a smoothly varying depth-velocity model. We performed a separate isotropic inversion to determine the SH/SV velocity ratio that explains the observed Rayleigh/Love wave incompatibility by a transverse isotropic model. The resulting velocity models (βR for Rayleigh, βL for Love) show an anisotropy of about 10%. However, synthetic seismograms, calculated using the 1066A velocity model, show that at least part

of this phase velocity incompatibility is due to contamination of the fundamental mode Love wave with higher modes (the Rayleigh wave phase velocities are not affected by higher mode interference). We corrected for this higher mode interference by subtracting the difference in phase velocities determined using fundamental mode Love waves synthetics, using velocity model 1066A, and using synthetics containing all modes, from the measured Love wave dispersion. We found, however, that this correction can not entirely account for the found Love/Rayleigh wave discrepancy. We offer two possible mechanisms which, separately or in combination, can explain these observations; (1) there is anisotropy (around 4% or less) present in the upper mantle in California. This anisotropy could be due to intrinsic anisotropy of olivine crystals in the upper mantle, or a laminated structure with alternating high and low velocity layers (Toksöz and Anderson, 1963), that has not been properly modelled by body wave studies. (2) The Rayleigh/Love wave discrepancy can be accounted for in another way which does not require anisotropy. Possible mechanisms include: contamination of Love wave fundamental mode by higher modes. Even if our numerical experiment suggests that this effect is not large enough to explain the observed Love/Rayleigh disparity, the proximity of the group velocities of the fundamental and higher mode Love waves could contaminate the fundamental mode more strongly than suggested by our numerical experiments using model 1066A. Another possible cause for the discrepancy is the upper mantle heterogeneity in southern California, such as the Transverse Range anomaly. It is possible that the heterogeneity affects Love and Rayleigh wave velocities differently so that it yields the apparent anisotropy. Numerical studies would be necessary to explore this possibility.

If the Love wave data are not to be used, the βR velocity model represents the upper mantle S velocity structure beneath southern California. Our results for Rayleigh wave dispersion show that the TNA model is not a representative model for the SV-structure beneath southern California. Velocities need to be 3 to 4% lower in the upper mantle to explain our measurements.

Acknowledgements

References

Aki, K., Crustal structure in Japan from the phase velocity of Rayleigh waves, Bull. Earthquake Res. Inst. Tokyo Univ. 39, 255-283, 1961.

Aki, K., Three-dimensional seismic inhomogeneities in the lithosphere and asthenosphere : Evidence for decoupling in the lithosphere and flow in the asthenosphere, Rev. Geophys. Space Phys. 20, 161-170, 1982.

Anderson, D.L. and A.M. Dziewonski, Upper mantle anisotropy: evidence from free oscillations, Geophys. J. R. astr. Soc., 69, 383-404, 1982.

Babuska, V. and M. Cara, Seismic anistropy in the earth, Kluwer Academic Publishers, Dordrecht, 217 pp, 1991.

Dorman, J., Ewing, M. and J. Oliver, Study of shear-velocity distribution in the upper mantle by mantle Rayleigh waves, Bull. Seism. Soc. Am. 50, 87-115, 1960.

Ewing, M. and F. Press, Determination of crustal structure from phase velocity of Rayleigh waves, Part 3, the United States, Bull. Geol. Soc. Am.. 70, 229-234, 1959.

Gilbert, F. and A.M. Dziewonski, An application of normal mode theory to the retrieval of structural parameters and source mechanism from seismic spectra, Phil. Trans. R. Soc. London, Series A, 278, 187-209, 1975.

Grand, S.P. and D.V. Helmberger, Upper mantle shear structure of North-America, Geophys. J. R. 76, 399-438, 1984.

Hadley, D. and H. Kanamori, Regional S-wave variation for southern California from the analysis of teleseismic Rayleigh waves, R. Astron. Soc., Geophys. J. 58, 655-666, 1979.

Hadley, D., Geophysical investigations of the structure and tectonics of southern California. Thesis, California Institute of Technology, Pasadena, 167 pp, 1978.

Humphreys, E.D. and R.W. Clayton, Tomographic image of the southern California mantle, J. Geophys. Res. 95, 19725-19746, 1990.

Jones, C.H. and H. Kanamori, Missing roots and mantle "drips" : Regional Pn and teleseismic arrival times in the southern Sierra Nevada and vicinity, California. J. Geophys. Res. 99, 4567-4601, 1994.

Kirkwood, S.C., The significance of isotropic inversion of anisotropic surface-wave dispersion, Geophys. J. R. astr. Soc. 55, 131-142, 1978.

Knopoff, L., Observation and inversion of surface wave dispersion, Tectonophys. 13, 497-519, 1972.

Knopoff, L., The thickness of the lithosphere from the dispersion of surface waves, Geophys. J. R. astr. Soc. 74, 55-81, 1983.

McEvilly, T.V., Central U.S. crust-upper mantle structure from Love and Rayleigh wave phase velocity inversion, Bull. seism. Soc. Am. 54, 1997-2015, 1964.

Mitchell, B.J., On the inversion of Love and Rayleigh wave dispersion and implications for Earth structure and anisotropy, Geophys. J. R. astr. Soc. 76, 233-241, 1984.

Press, F., Determination of crustal structure from phase velocity of Rayleigh waves part I : southern California, Bull. Geol. Soc. Am., 67, 1647-1658, 1956.

Raikes, S.A., The temporal variation of tele-seismic P-residuals in southern California, Bull. seism. Soc. Am. 68, 711-720, 1978.

Schlue, J.W. and L. Knopoff, Inversion of surface-wave phase velocities for an anisotropic

structure, Geophys. J. R. astr. Soc. 54, 697-702, 1978.

Stange, S. and W. Friederich, Surface wave dispersion and upper mantle structure beneath southern Germany from joint inversion of network recorded teleseismic events, Geophys. Res. Lett. 20, 2375-2378, 1993.

Takeuchi, H., Dorman, J. and M. Saito, Partial derivatives of surface wave phase velocity with respect to physical parameter changes within the earth, J. Geophys. Res. 69, 3429-3441, 1964.

Thatcher, W. and J.N. Brune, Higher mode interference and observed anomalous apparent Love wave phase velocities, J. Geophys. Res. 74, 6603-6611, 1969.

Toksöz, M.N. and D.L. Anderson, Generalized two-dimensional model seismology with application to anisotropic earth models, J. Geophys. Res. 68, 1121-1130, 1963.

Wang, J. and T.L. Teng, Surface-wave profiling of the lithosphere beneath the Mojave desert using TERRAscope data. J. Geophys. Res. 99, 743-750, 1994.

Chapter 2:

Shear Wave Anisotropy Beneath the Andes
from the BANJO, SEDA and PISCO experiments

Abstract

We present the results of a shear wave splitting analysis of data collected by three temporary broadband arrays located on the central western margin of South America. The BANJO array constituted an almost 1000 km long east-west transect at a latitude of 20° south, the PISCO and SEDA arrays were located between 16° and 26° south within 500 km from the continental margin. We determined the splitting parameters ϕ (fast polarization direction) and δt (delay time between fast and slow polarized shear waves) for teleseismic SKS, SKKS and PKS as well as for local S and ScS waves from intermediate to deep events. This enabled us to investigate the depth distribution of the anisotropy in the Nazca plate subduction zone. Results from local S waves suggest that although there is some anisotropy present above the slab, the main contribution to the *KS delay time for SEDA and PISCO, as well as the western BANJO stations is from below the slab. Almost all BANJO stations show EW fast directions with delay times varying between 0.4 and 1.5 sec. This direction is approximately orthogonal to the trench and the slab contours. However, the SEDA and PISCO stations, as well as results from local S deep-focus events which are located north and south of the BANJO transect, show a rotation of ϕ to approximately trench parallel fast directions.

Assuming the anisotropy is due to lattice preferred orientation (LPO) in olivine, the EW

results for the easternmost BANJO stations, where the top of the slab is deeper than 400 km, can most likely be explained by an above-slab mechanism, such as 'fossil' anisotropy associated with the Brazilian Craton. The above slab pattern of anisotropy rapidly changes near the center of the BANJO line, possibly indicating the western edge of the Brazilian craton. For the western stations we find NS fast directions and small delay times for the above slab component, which is consistent with (namely orthogonal to) the current maximum compressive horizontal stress direction according to the World Stress Map, and most easily explained by east-west shortening in the South American plate. We see no evidence for a corner flow pattern in the mantle wedge, which would predict EW fast directions. The results for the PISCO and SEDA arrays, as well as the western BANJO stations, also require deformation and flow below the slab. We interpret the combined data within the context of the mantle flow model of Russo and Silver (1994), where there is a component of trench parallel flow beneath the slab. The additional presence of a trench-normal distribution of measurements requires a separate explanation, and we specu-late that it may be due to a breach in the slab beneath these stations.

Introduction

Shear wave splitting, being a first-order anisotropy-related phenomenon, is a reliable, direct way to map the anisotropy in the mantle and crust. The well-documented close rela-tionship between anisotropy and finite strain, through the lattice preferred orientation (LPO) of mantle minerals (Nicolas and Poirier, 1976; Christensen, 1984; Mainprice and Silver, 1993), means that shear wave splitting is a powerful tool for studying the deforma-tional properties of the crust and subcontinental mantle as well as the mantle flow field. In shear wave splitting an incident shear wave is polarized into two orthogonal directions travelling at different velocities. The splitting parameters, the fast polarization direction ϕ and the delay time between the slow and fast split wave δt can provide information on the

direction of flow (sense of strain) and give some constraint on the depth extent of the anisotropy. Studies of the anisotropy of the mantle based on the splitting of various kinds of shear wave phases were first performed by Ando and Ishikawa (1982),Vinnik et al. (1984), Kind et al. (1985) and Silver and Chan (1988). The splitting of teleseismic core phases like SKS has been intensively used because of its many advantages: it has a high resolving power on the lateral variation of anisotropy because of the steep incidence angle at the station; furthermore, since SKS leaves the core-mantle boundary (CMB) on the receiver side as a naturally polarized SV wave after travelling through the core as a P wave, the presence of energy in a direction perpendicular to the back-azimuth (i.e., on the tangential component) is indicative of azimuthal anisotropy which can be restricted to the receiver side of the path. This energy will result in an elliptical particle motion in the horizontal plane. However, since the splitting parameters for SKS represent an integration of anisotropy along the nearly vertical path from the CMB to the surface, it can not resolve the depth distribution of the anisotropy.

In this study we examine seismic anisotropy in the mantle underneath the Andes by using shear wave splitting observed in teleseismic SKS, PKS and SKKS phases, as well as direct S waves from local intermediate focus earthquakes in addition to direct S and ScS waves from local deep-focus earthquakes to achieve some measure of vertical resolution. This allowed us to study flow and deformation both above the slab in the mantle wedge and below the slab, after reasoning about the contribution of the slab itself.

Russo and Silver (1994) have proposed a trench parallel flow model for the upper mantle beneath the subducting Nazca plate in South America, based on observations of trench parallel fast splitting directions of teleseismic S and SKS phases. This trench parallel flow is orthogonal to the flow pattern predicted by a two-dimensional entrained mantle flow model beneath the subducting Nazca plate and is attributed to retrograde motion of the slab and the decoupling of the slab and underlying mantle. However, in their study Russo and Silver also found several zones of ϕ directions normal to the trench and attributed these to
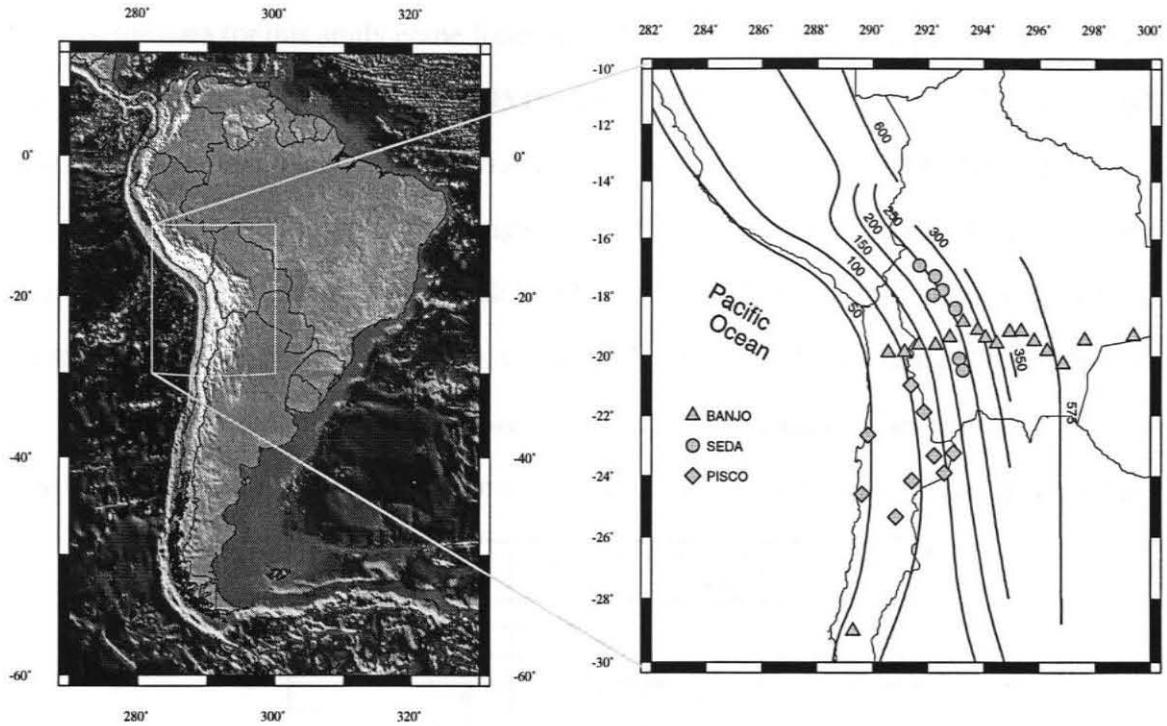
Figure 1: Shaded relief map of the location of the BANJO, SEDA and PISCO temporary networks in south America. Triangles denote BANJO stations, circles SEDA stations and diamonds PISCO stations. The contour lines plotted at 50 km intervals show the depth of the subducted Nazca slab (south of 12°S latitude after Cahill and Isacks (1992), north of 12°S latitude from Russo and Silver (1994)).

deflections of the overall trench parallel flow as a result of abrupt changes in slab dip. With the availability of the additional data from several passive seismological experiments carried out in South America involving portable broad band seismographs, viz. BANJO, SEDA and PISCO (Figure 1), we will test this model and perform a more detailed analysis of the depth and lateral distribution of the anisotropy and hence of the mantle flow in the South American subduction zone.

Data and Method

Most of the data for this study come from several passive broadband experiments that were run in South America in 1994 and 1995 (Figure 1 and Table 1). The BANJO (Broadband ANdean JOint experiment) network was a joint project between the University of Arizona and the Carnegie Institution of Washington, DTM. Other institutes involved with the operation of this network were the San Calixto Observatoria, La Paz, Bolivia, the Depto. de Geophisica, Universidad de Chile, Santiago, Chile and ORSTOM, France. This temporary array was deployed along a near east-west transect in the Central Andes across the western Cordillera, Altiplano, eastern Cordillera, sub-Andean zone and Chaco plain, spanning a

Station	Latitude	Longitude	Elevation (m)	Seismometer
BANJO network				
c1	-19.869	-69.438	1620	STS-2
c2	-19.852	-68.850	4110	STS-2
01	-19.607	-68.326	3688	STS-2
02	-19.621	-67.726	3780	STS-2
03	-19.354	-67.223	3749	STS-2
04	-18.828	-66.734	3810	STS-2
05	-19.104	-66.221	4267	STS-2
06	-19.375	-65.929	3566	STS-2
07	-19.563	-65.525	3505	STS-2
08	-19.158	-65.069	2896	STS-2
09	-19.148	-64.643	2591	STS-2
10	-19.486	-64.178	2073	STS-2
11	-19.812	-63.721	1676	STS-2
12	-20.255	-63.158	823	STS-2
13	-19.452	-62.373	396	STS-2
14	-19.297	-60.617	335	STS-2
lcoc	-29.287	-70.690	2450	CMT-3
SEDA network				
chit	-20.077	-66.886	3862	CMG40T
chuq	-17.945	-67.818	4178	CMG40T
coll	-16.922	-68.315	4329	CMG40T
lajo	-17.776	-67.479	3788	CMG40T
poop	-18.387	-67.018	3721	CMG40T
sica	-17.292	-67.749	4065	CMG40T
uyun	-20.463	-66.747	3936	CMG40T
PISCO network				
001	-24.155	-68.589	3100	STS-2
009	-23.890	-67.414	4400	STS-2
012	-23.324	-67.779	4000	STS-2
013	-23.233	-67.085	4300	STS-2
017	-21.881	-68.151	4550	STS-2
mic	-22.654	-70.175	833	STS-2
par	-24.598	-70.385	2450	CMT-3
uji	-20.972	-68.619	4350	CMT-3
vaq	-25.349	-69.166	3750	CMT-3

Table 1: Station Locations.

length of nearly 1000 km. It consisted of 16 broadband stations with STS-2 sensors and a sampling rate of 0.1 sec. Most of the stations were operated from March 1994 until September 1995. The SEDA (Seismic Exploration of the Deep Altiplano) experiment consisted of seven stations (CMG40T instruments) that were deployed in a 350 km north-south transect along the eastern boundary of the Altiplano, between La Paz and Uyuni, Bolivia between April 1994 and May 1995. The PISCO (Projecto de Investigacion Sismologica de la Cordillera Occidental) network was located in the Atacama desert of northern Chile and was a joint research program of German (GeoForschungsZentrum Potsdam, Free University of Berlin) and Chilean (Universidad del Norte Antofagasta) institutions. It was operated over a 100-day period from February till May 1994 and consisted of eight broadband stations which were equipped with three component STS-2, CMT-3 or CMG40T seismometers as well as 20 short period stations (the short period data were not used in this study because of possible problems with cycle skipping). The broadband continuous records were obtained with a 10 or 20 Hz sampling frequency. We also obtained suitable data for one event for station LVC, located in Chile, of which the data became available through the IRIS data center in 1997.

We used teleseismic recordings of SKS, PKS and SKKS phases, as well as S and ScS waves of intermediate to very deep earthquakes which were located almost directly beneath the networks or in their close vicinity (Figure 2, Appendix A). Performing measurements on all of these phases enabled us to conduct a more detailed investigation of the vertical distribution of the anisotropy in this region. The selected data had to satisfy several different criteria. The phases had to have a sufficient signal to noise ratio, a clear shear wave arrival, and had to arrive isolated on the seismogram. The incident angle to the free surface of the local S-waves had to be less than the critical angle for S-to-P conversion, which was assumed to be 40 degrees. PKS data was only used when the signal on the vertical component was negligeable, indicating no interference with a possible SKP phase. In most cases a wide bandpass filter was used (between 1 and 100 sec or between 1 and 25
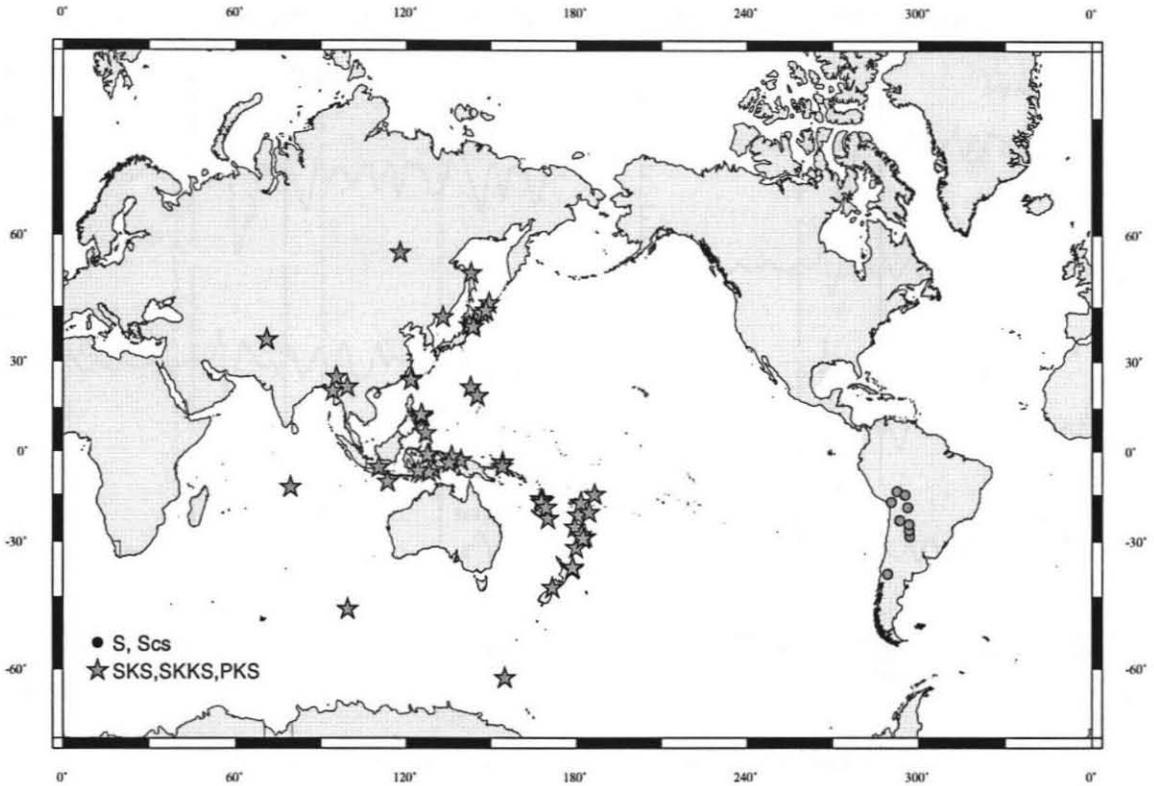
Figure 2: Events used in this study. Stars show location of events of which *KS phases were used. Circles show local S and ScS events.

sec) to filter out industrial and other noise, but retaining most of the broadband signal. Overall, we checked that this filter did not change the final result but did reduce the error in the measurements.

The method used for estimating the fast polarization direction (ϕ) and the delay time (δt) is described in detail in Silver and Chan (1991), and we show examples in Figure 3 and 4. The splitting parameters can be determined by finding the values of ϕ and δt that, when used to correct for the anisotropy, most completely remove the splitting. In cases where the polarization direction (ϕ_p) is predicted to be equal to the back-azimuth (ϕ_b), such as with SKS, SKKS and PKS phases, we can estimate the splitting parameters to be those that minimize the energy on the transverse component after correcting for all possible values of ϕ with increments of 1° and values for δt ranging between 0 and 4 sec with increments of 0.05 sec or 0.10 sec. For all S phases, the splitting parameters can be determined by

Event:1994361173252500 Sta:st01 Dist:97.0 Az:118.1 Baz:232.6 -32.003N 179.870E 228km

(a)

(b)

IASPEI 91 Tables
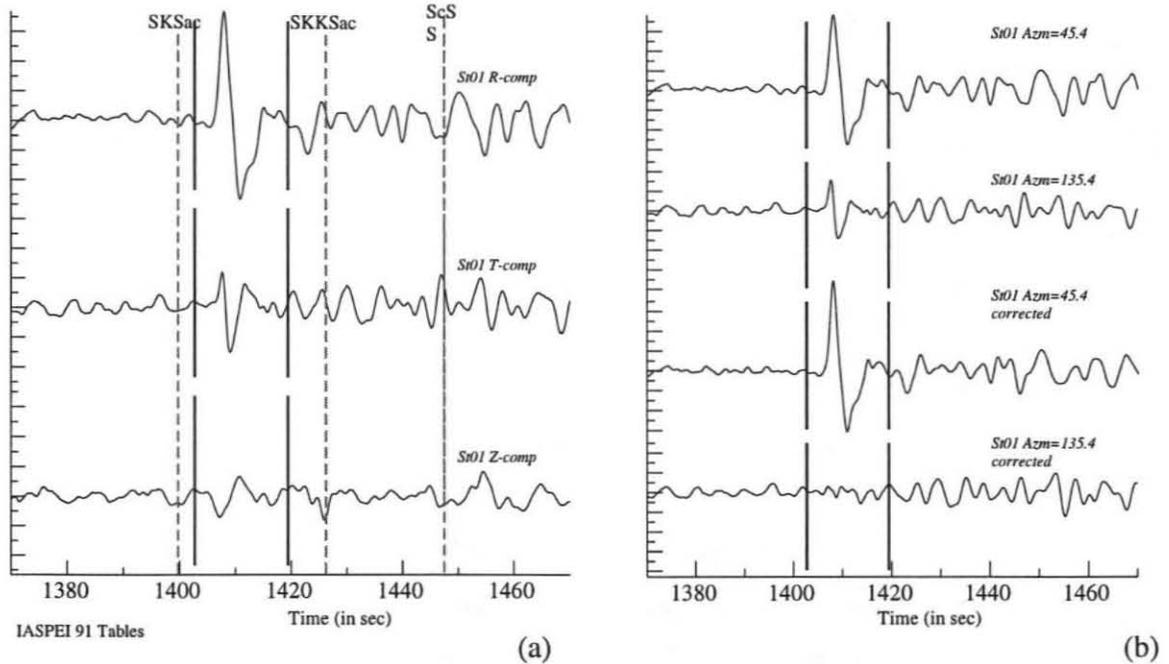
Figure 3(a): Three component broadband seismogram of SKS for BANJO station 01 and event 19943611732525 near Tonga. Predicted arrival times for IASPEI 91 are shown by dashed lines. Solid lines mark the time window used to make the measurements.

Figure 3(b): (Top two traces) The original horizontal components in the polarization direction and the direction orthogonal to it. (Bottom two traces) The horizontal components corrected for the determined values of ϕ and δt. Note that in the corrected seismogram, the energy arriving on the component orthogonal to the polarization direction ("transverse" component) has been removed.

minimizing the smaller eigenvalue of the two-dimensional covariance matrix of corrected horizontal particle motion. This is equivalent to finding the most linear particle motion. By also using this method for *KS phases, we allow for the possibility that the presence of energy on the tangential component is caused by the rotation of the ray away from the great circle path (i.e., by a dipping layer). At the same time, we estimate the azimuth of the isotropic polarization vector. In the case of S and ScS phases, this azimuth can be compared with the predicted value, when moment tensor solutions are available. Formal

(c)

(d)
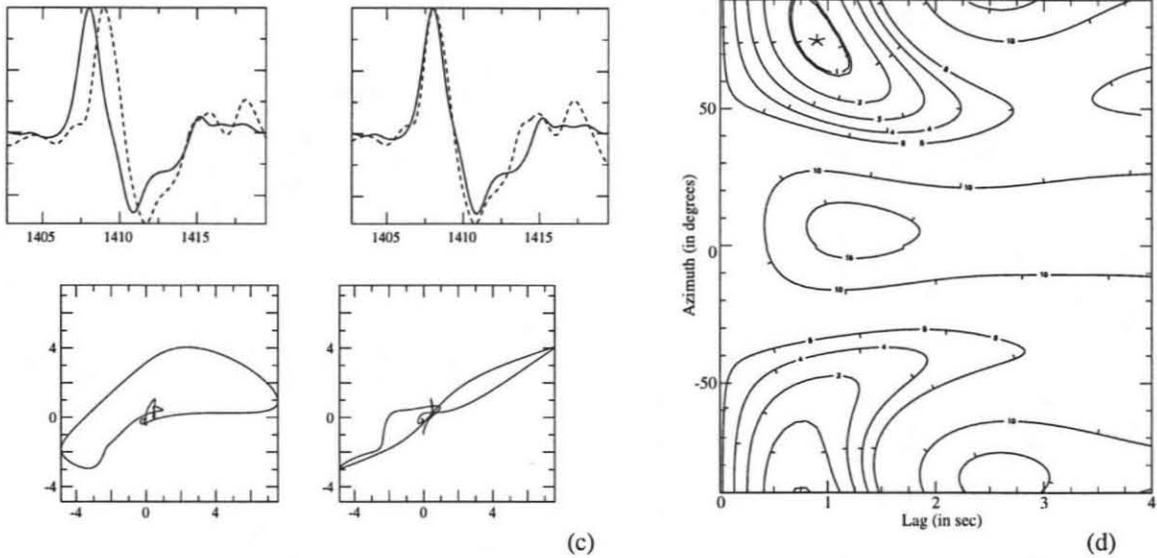
Figure 3(c): (Top two windows) Superposition of fast and slow components uncorrected (left) and corrected for delay time (right). Note the great similarity of the two waveforms. (Bottom two windows) Horizontal particle motion for uncorrected (left) and corrected (right) components.

Figure 3(d): Contour plot of the eigenvalues in ϕ, δt space. Minimum value shown as star with 95% confidence region (double contour) and multiples of that contour level.

uncertainties are obtained for all individual measurements as in Silver and Chan (1991). In the case of SKS, SKKS and PKS phases, when measurements can be made by using both procedures, we chose the measurement with the smallest error as our final result for a single event. Measurements that have error ellipses which are narrow in the ϕ direction, but elongated in the δt direction, suggest little or no splitting. Such measurements are called 'nulls' and are consistent with either isotropic material or with a fast or slow direction in the ϕ_p direction. Single splitting measurements were only deemed reliable when there was a strong correlation between the waveforms of the fast and slow component, a well constrained error ellipse, a clear elliptical particle motion, consistent results using slightly different time windows and in the case of *KS phases, consistent results using both proce-

Event:1994361173252500 Sta:uyun Dist:97.6 Az:119.7 Baz:231.8 -32.003N 179.870E 228km

(a)

(b)

(c)

(d)
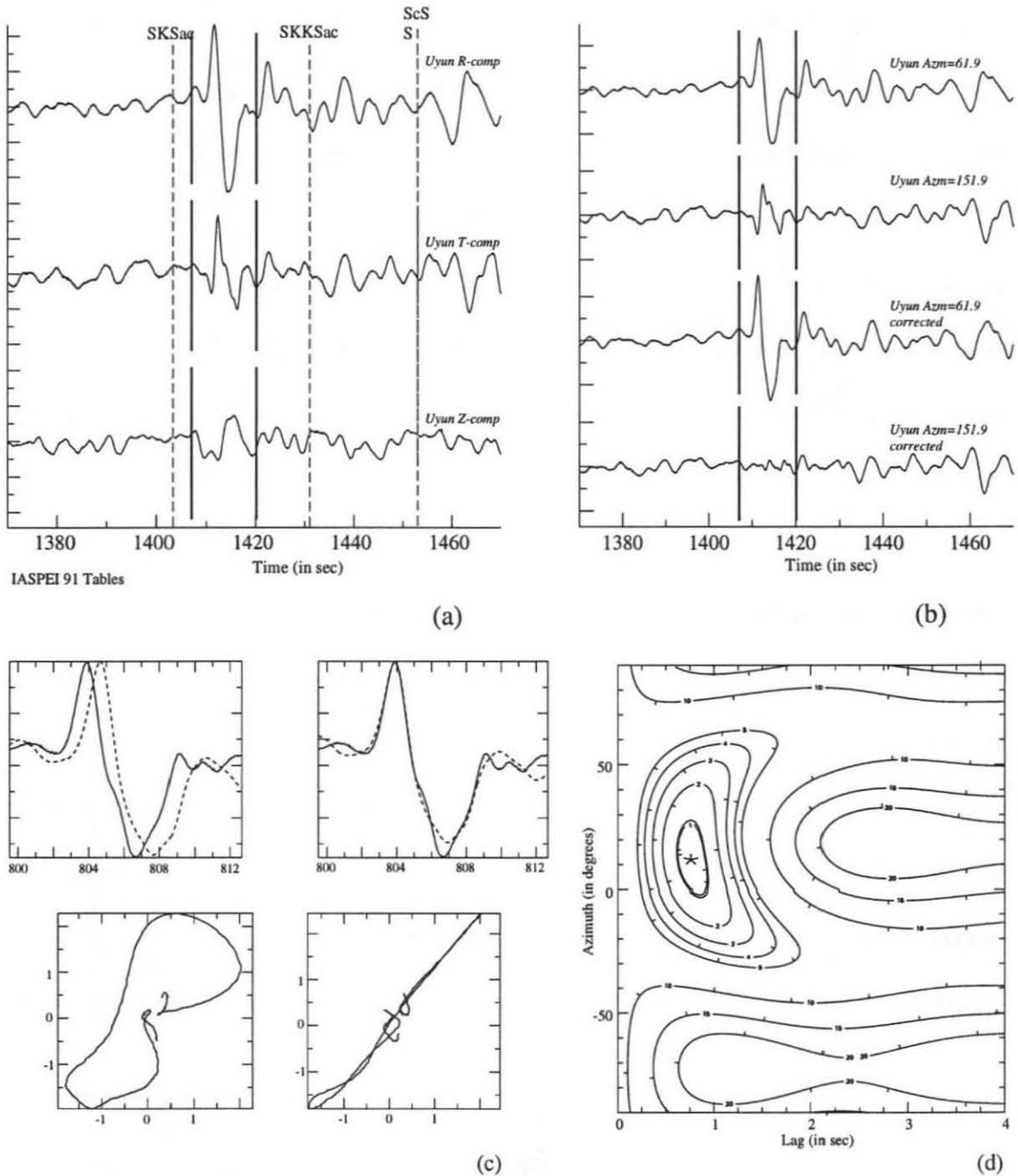
Figure 4: Same as Figure 3 for SEDA station uyun.

dures for estimating δt and φ. We show an example of a record section of split SKS waves

on the tangential component for one event near Tonga in Figure 5 as an illustration of the

data quality of one of the better events. The left-hand side of the figure shows the tangential
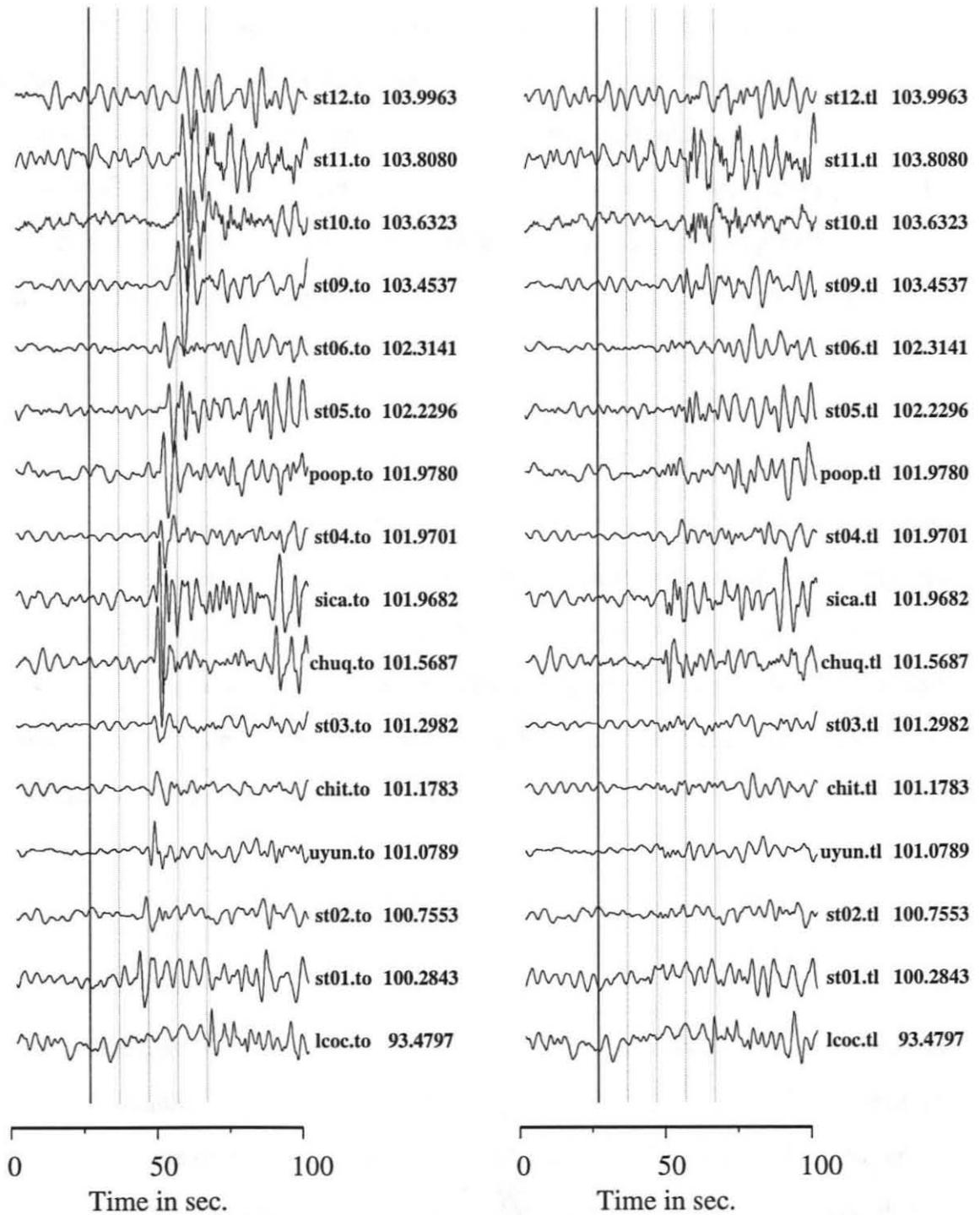
Figure 5: Record section of tangential component of SKS recorded by BANJO and SEDA stations for an event near Tonga. Left-hand side: before correction for splitting. Right-hand side: after correction . Station names and epicentral distance in degrees are indicated to the right of the traces.

traces sorted as a function of distance before we corrected for the measured anisotropy parameters. The right-hand side shows the same traces after correction (in this case all parameters were obtained by applying the method based on minimizing energy on the transverse component). This correction has removed almost all coherent energy for SKS, although obviously we can not correct for the scattered energy arriving after SKS. In almost all cases significant energy was present on the tangential traces before the correction.

We compute the final *KS result for each station by stacking the arrays of either energy on the tangential component or the value of the smaller eigenvalue of the covariance matrix and determining the overall minimum (Wolfe and Silver, 1998). This method has several advantages over simple averaging of the different measurements, most importantly, null measurements can be incorporated into the final result. By correcting all of the seismograms for these final values of δt and ϕ, we can check to see if all of the events fit these values, or if significant energy is introduced on the component orthogonal to the back-azimuth, indicating that these values of the splitting parameters conflict with the data for that event.

Station Stacks

Because the time period in which the BANJO and SEDA networks were active spanned almost 18 months, these stations recorded many suitable events over a wide range of back-azimuths (Figure 6). By examining the suite of estimated splitting parameters for an individual station, we can check to see if the splitting parameters display a dependence on initial polarization. If this is the case, the anisotropy may not be localized within a single homogeneous layer, or there may be laterally varying anisotropy, or anisotropy with a dipping symmetry axis. In the case of two or more anisotropic layers, for example, the splitting parameters exhibit $\pi/2$ periodicity as a function of ϕ_p (Silver and Savage, 1993;
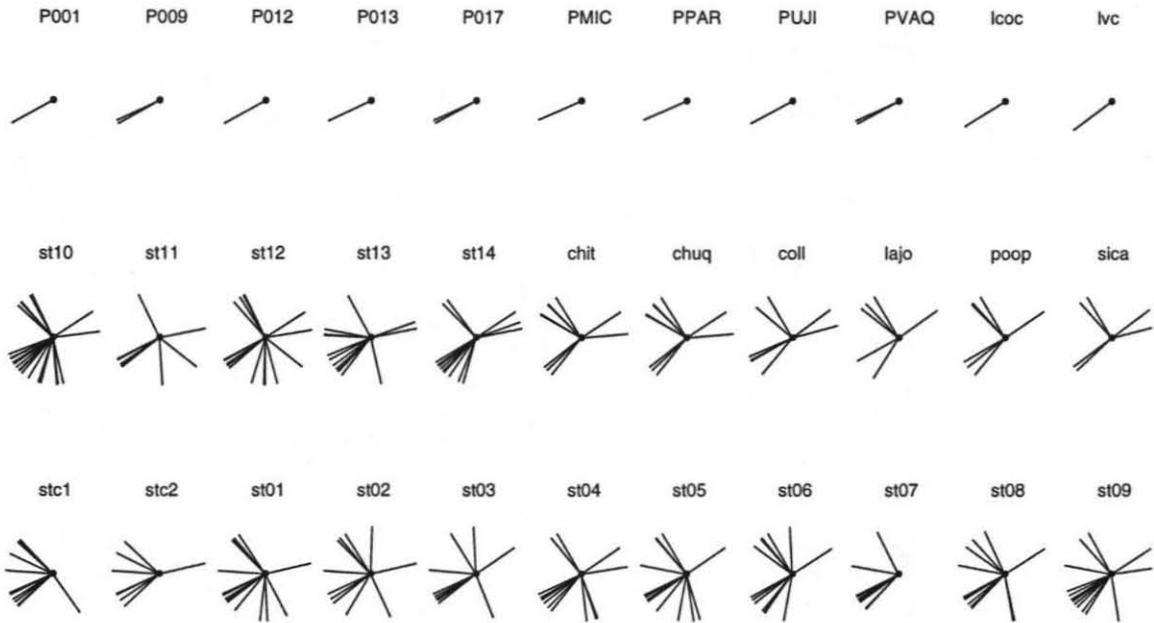
Figure 6: Rose diagrams for all stations of back-azimuth of events used in final stacks.

Silver and Savage, 1994; Rumpker and Silver, 1998). However, stacking the probability distributions for different events for an individual station produced a well constrained overall minimum, and corrected horizontal components typically showed no significant energy on the component orthogonal to the isotropic polarization direction (e.g., Figure 7 for BANJO station 13), indicating that the anisotropy is probably localized within a single homogeneous layer and can be characterized as a region with hexagonal symmetry with a subhorizontal axis of symmetry. The data we used in these stacks were *KS phases (SKKS, SKS and PKS) as well as those ScS phases of which the individual measurements agreed with the overall result (this will be discussed further in the next section). Small differences in fast direction and/or delay time are to be expected however, since lateral differences in anisotropy probably exist and although the incidence angle for the teleseismic *KS events is close to vertical, the rays still sample slightly different regions in the upper mantle. Figure 8 shows the ray paths for BANJO station st04 and for the events used in estimating the splitting parameters. Using the same stacking technique, we estimated the splitting
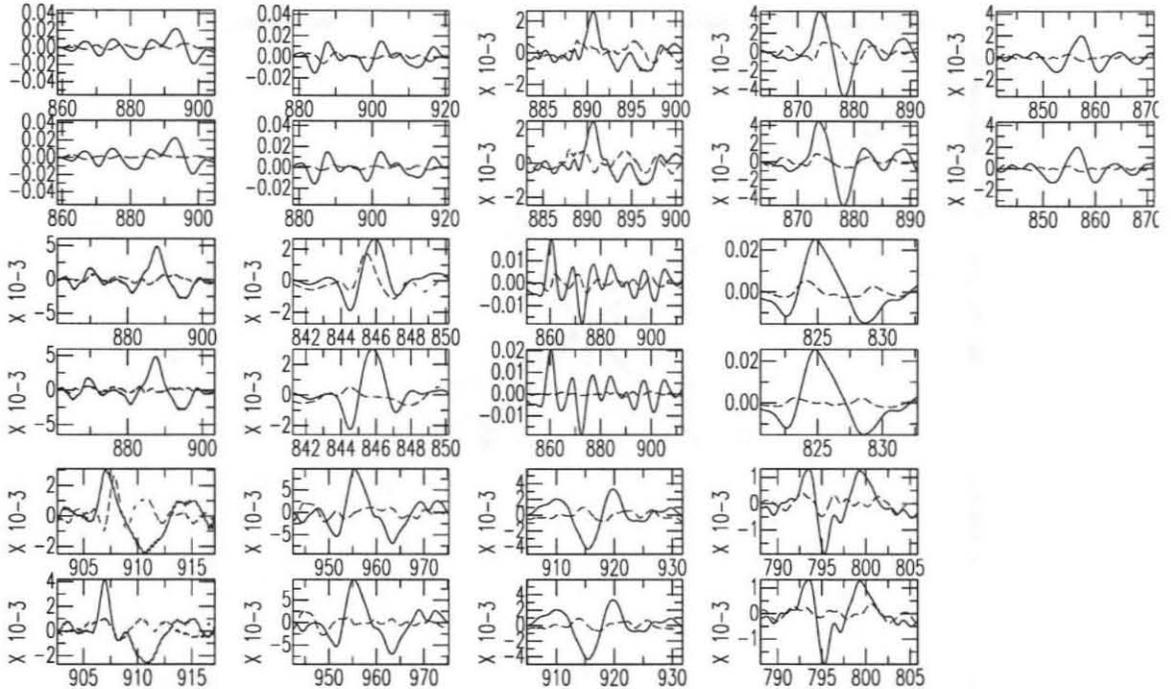
Figure 7: Original horizontal components (parallel and orthogonal to final direction of motion) for events used in *KS stack for station BANJO st13 (top windows) and horizontal components after correction for final splitting parameters (bottom windows). Dashed lines show components orthogonal to direction of motion (which is the tangential component in the case of *KS waves).

parameters for all of the PISCO, SEDA and BANJO stations. The final results are shown in Appendix A and Figure 9, together with the number of events used in the final stack. The color of the vectors indicates the reliability of the results (darker colors showing the more reliably measurements), as measured by azimuthal coverage, number of events and standard errors (signal to noise) for the single event measurements. Since only two suitable events were recorded by the PISCO network during the time of deployment and these events were almost at the same location, for several PISCO stations we could only determine the two possible fast directions resulting from null measurements, shown as two orthogonal lines with a length corresponding to a delay time of 0.25 sec. Overall, most of the measured fast directions correspond to either a trench-normal (EW) or a trench parallel aligned fast polarization direction. The BANJO array consistently shows EW fast
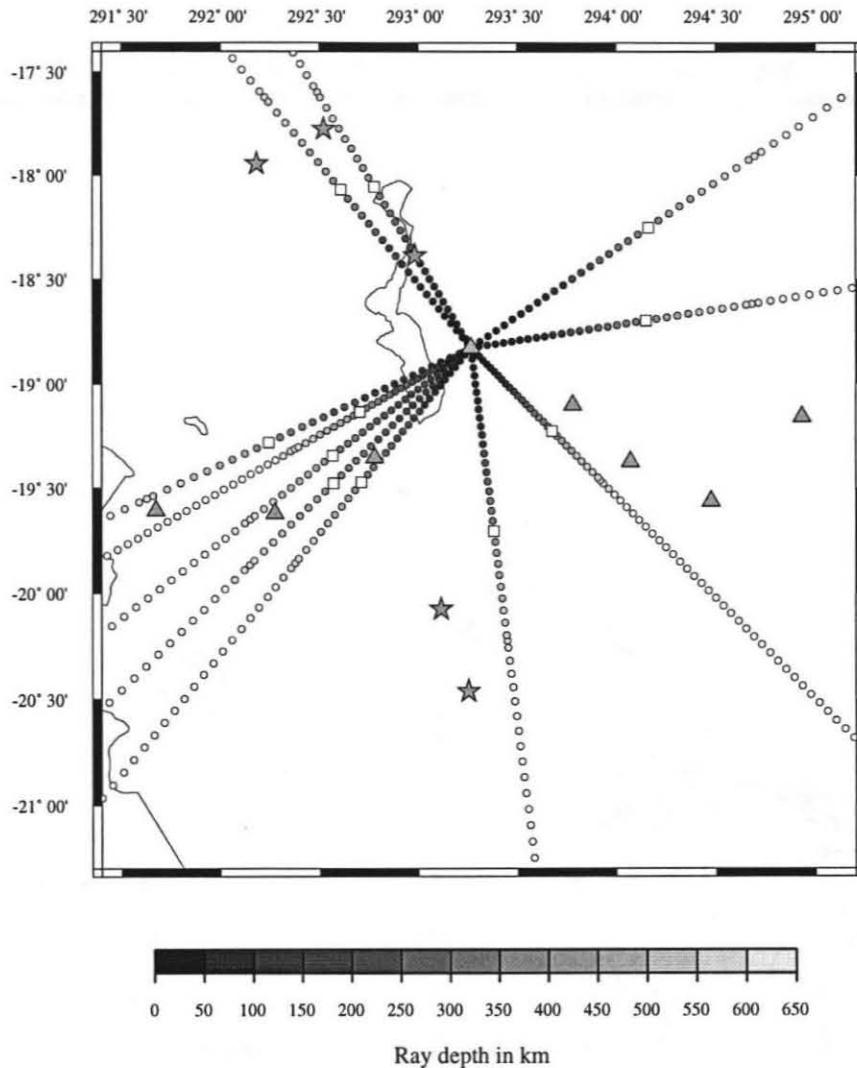
*Figure 8: Raypaths for *KS phases in station 4 stack. Stars are SEDA stations, triangles BANJO stations. White squares indicate where rays cross 410 km depth (olivine stability field).*

directions, whereas most of the SEDA and PISCO stations show a fast direction parallel to the slab contours. Both of these directions are well resolved, as can be seen in the examples of Figures 3 and 4, as well as the record section in Figure 6.

ScS measurements

Because the ScS waves sample the mantle differently than the *KS waves (Figure 10), we can use these results together with the *KS and S measurements to say something about the
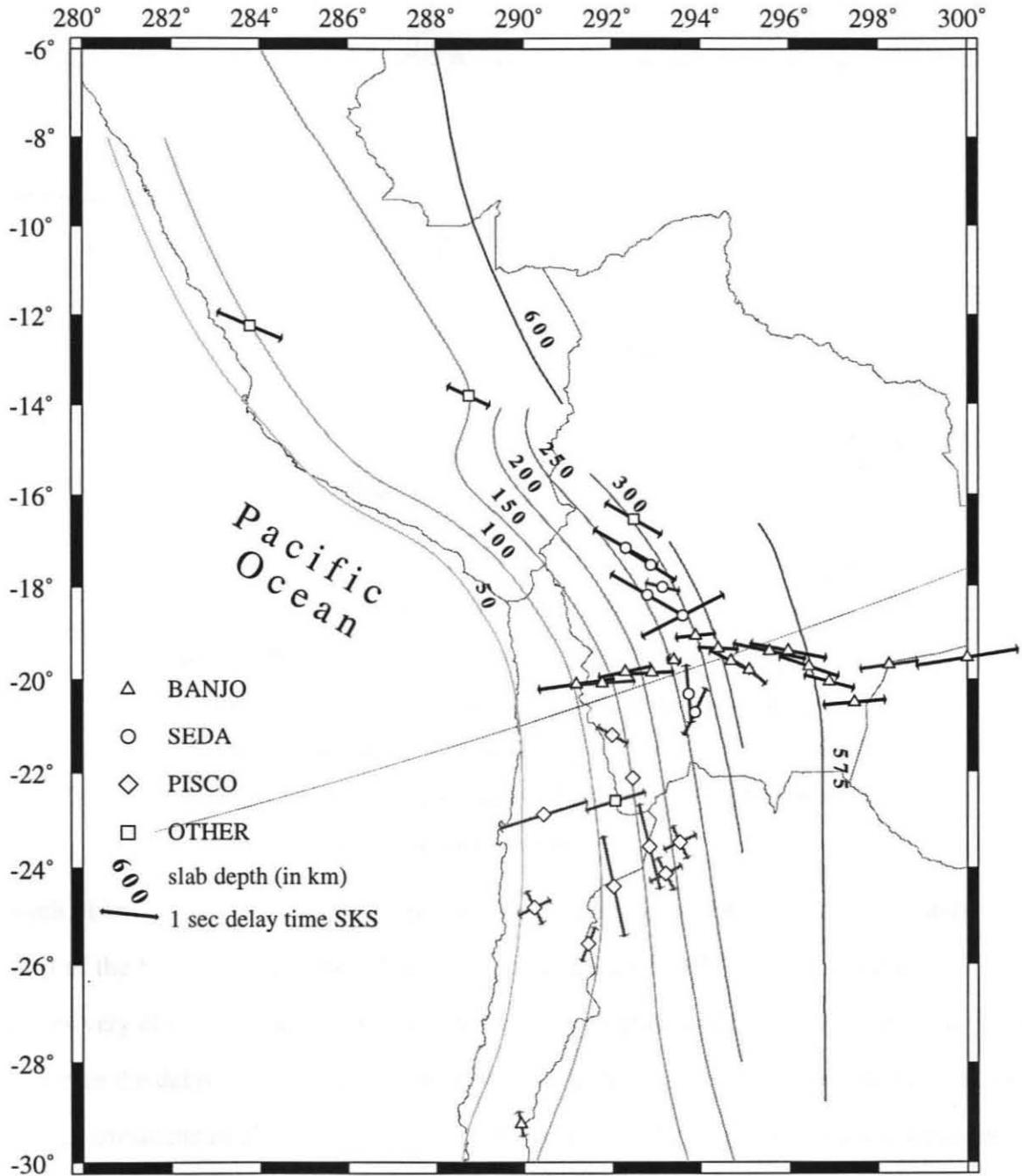
Figure 9: Map of splitting parameters for all BANJO, SEDA and PISCO stations from stacks. Arrows indicate fast polarization directions, the length of the arrows is proportional to the delay times. The dashed line indicated the symmetry line as described by Gephart (1994).
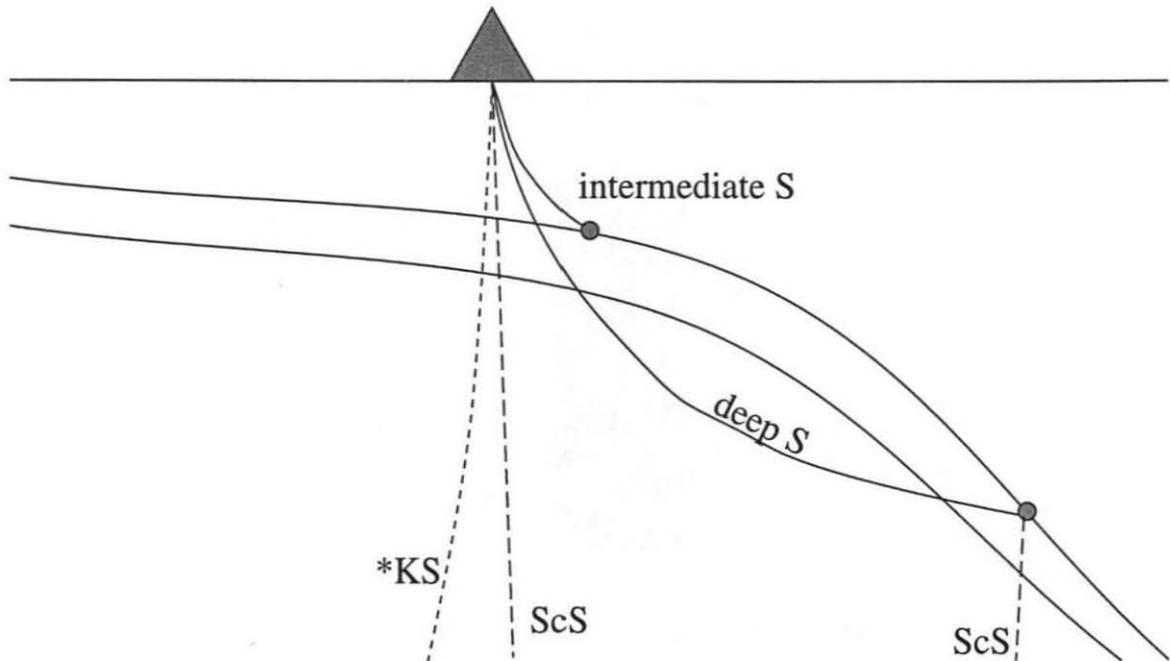
*Figure 10: Schematic view of the subducted Nazca plate, showing raypaths of various S-phases. *KS waves from tele-seismic events sample both above, in and below the slab. S waves from intermediate events in the slab directly below the region sample only the region above the slab. S waves from deep events sample both above, in and below the slab. ScS waves sample part of the mantle twice.*

depth distribution of the anisotropy in the Nazca plate subduction zone. Unfortunately, most of the ScS waves that had a high signal to noise ratio had incoming polarization angles very close, or nearly orthogonal, to the null direction and could not be used to constrain the delay time, or amount of anisotropy, although they were used in the stack to help constrain the final result. However, we found that the ScS delay times for several deep events (deeper than 500 km) were consistent (within the standard error) with the *KS delay times measured at the same stations, indicating that anisotropy in the path down from the source is negligible. We did not find any intermediate depth earthquakes with ScS waves that could fulfill our criteria for reliable measurements, because most had a low signal to noise ratio.
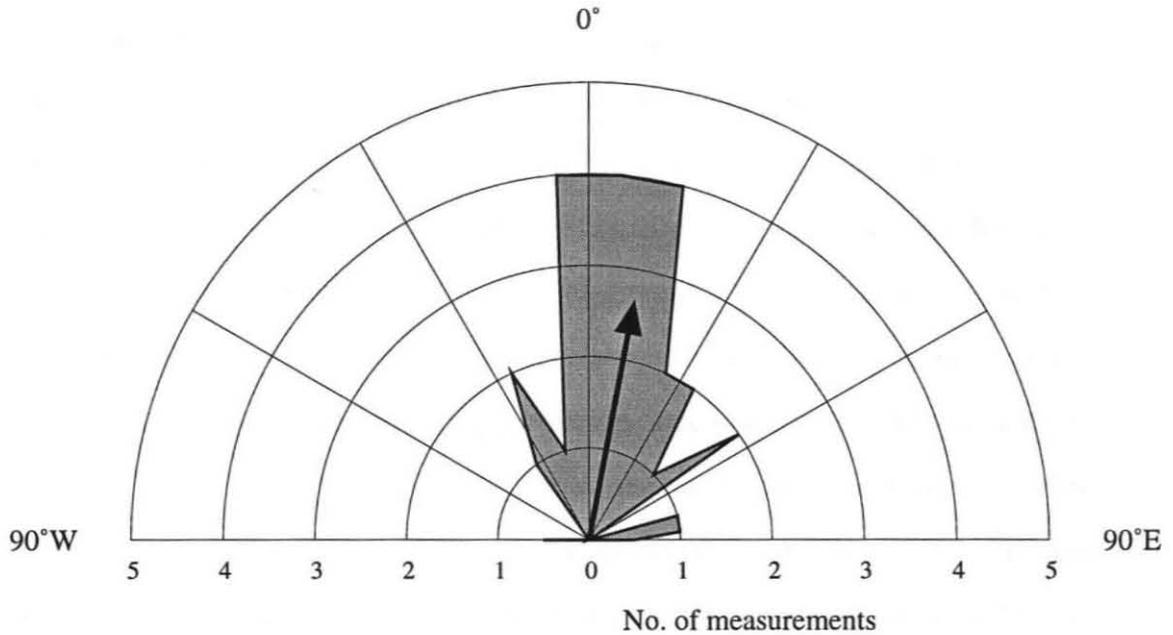
Figure 11: Rose diagram of splitting parameters found for all intermediate depth S phases, with paths above the subduction slabs, almost straight up to the stations, binned in sections of 10 degrees.

Local Intermediate and Shallow S measurements

We reviewed the data for over 50 local events, most obtained from the catalog of Myers (1998), and found 26 reliable measurements of S-wave splitting for events from 50 to 350 km deep to stations of the BANJO and SEDA networks (Figure 11). Our selection criteria were very strict: the incoming angle of incidence of the ray should be smaller than 40 degrees, which was verified by examining the energy on the vertical component of the record; there should be a high signal to noise ratio and we checked for converted P-wave arrivals which would arrive before the main S energy. We found that for many events, the scattering and the effect of the complex 3D velocity structure were too great to perform a reliable measurement. Since most of these events were fairly small (smaller than magnitude 5), we could not check the polarization angle using CMT solutions. We added

as an extra constraint that the fast direction obtained from maximizing the linearity of the corrected signal had to agree with the onset polarization direction of the data and that the delay time had to agree with the separation time of the onset of the signal when rotated into the fast/slow coordinate system. Since the delay times for this data set were fairly small (smaller than 0.5 sec), the error ellipses were usually elongated in the fast direction, but well-constrained in delay time. As the rose diagram in Figure 11 shows, the overall fast polarization direction of the above-slab anisotropy is NS, with relatively small delay times, which corrected for the non-vertical propagation direction would be approximately .3 sec or smaller. Since most of the *KS delay times are around 1 sec, this delay time is probably too small to be noticeable as a "second layer" of anisotropy, explaining why the results of *KS are so consistent with back-azimuth. As Figure 12 shows, since the direction is nearly orthogonal to the fast direction of the much larger below slab component, this layer would act to reduce the total delay time, but would not change the fast direction as a function of azimuth (curves calculated with equations from Silver and Savage, 1994), apart from a small range of polarization azimuths not covered by our data-set or interpretable as nulls. As demonstrated by Figure 13, the vertical delay times tend to increase with increasing source depth. The inferred trend suggests that there is indeed a mantle component to the above-slab path. Extrapolating the trend to 50 km depth suggests that there is a crustal component of about 0.1-0.15 sec with the rest being due to the mantle wedge. Studies in other parts of the world also yield a range in delay times of 0.1 to 0.3 sec for the crustal component of splitting, with occasional values up to 0.5 and an average of about 0.2 (Silver, 1996). Crustal delay times on the Tibetan Plateau, a region where the crust is comparably thick as beneath the Andes, also fall within this range of 0.1 to 0.3 sec (McNamara et al, 1994). Crustal delay times from a neighboring region in Peru were on the low side of this range (Kaneshima and Silver, 1995).
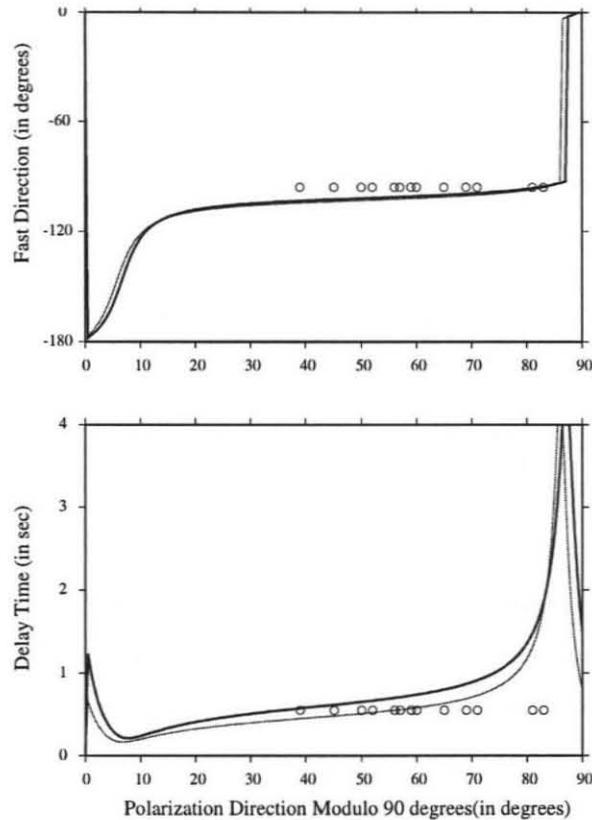
Figure 12: Curves for two layer anisotropy. Thin line shows model with bottom layer of 93 degrees fast direction and 0.70 sec delay time, top layer 13 degrees and 0.30 sec delay time, fat line from model with 95 degrees fast direction and 0.80 sec delay time bottom layer and 20 degrees and 0.30 sec delay time top layer. Circles show result from stack for station 4 and the polarization azimuth of all events used in stack. Since single events from this stack were sometimes badly constrained, splitting parameters from stack are used. Two most right circles correspond to null measurements

Local Deep S measurements

For the deep (deeper than 500 km) S wave measurements the extra constraint explained in the previous section was not necessary, because the delay times we obtained were all greater than 1 sec and the waveforms themselves were also much longer period than those
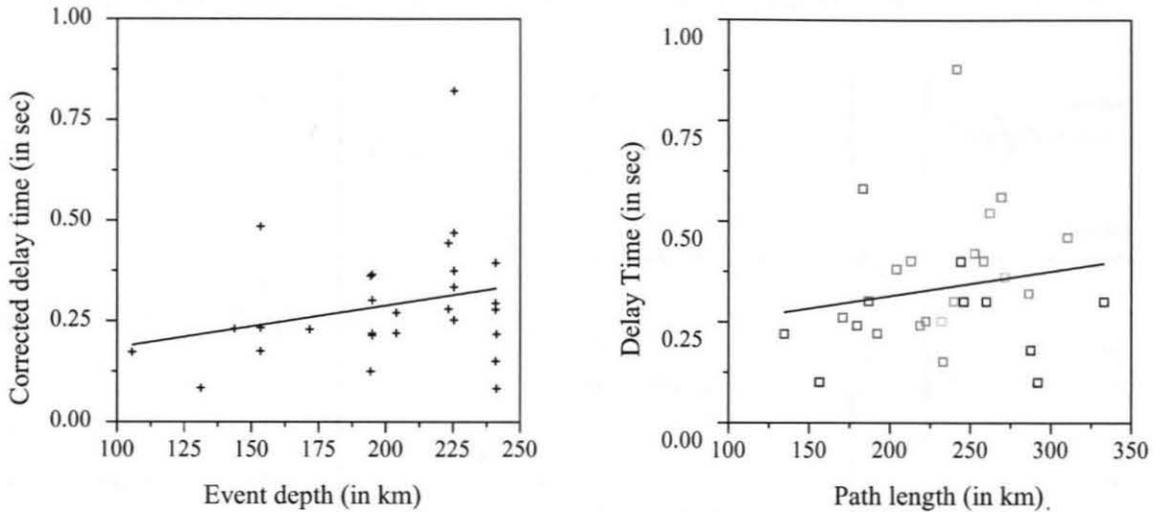
Figure 13: S-wave delay times as a function of path length and event depth. Right panel: Delay time as a function of path length. Symbols are color coded with depth from purple (shallow, 75 km) to red (deeper, 350 km). Left panel: Corrected delay time as a function of event depth. Corrected delay times were calculated by dividing the delay times by the path length and multiplying it by the event depth. This would be the delay time for a vertically incident S-wave. For most stations this delay time is smaller than 25% of the *KS delay time.

of the intermediate depth earthquakes. We found several events which were located closely together in clusters, one to the NE of the center of the BANJO line, namely the Great Bolivian earthquake of 9 June, 1994, plus an aftershock and one to the SE, the region of Santiago del Estero. We could use these events to check the reliability and repeatability of our measurements and found that the results for the different events in the same cluster agreed very well. One representative example for deep S wave splitting is shown in Figure 14.

Because of data gaps, and the constraint on incidence angle, simplicity of waveform and off-angle arrivals at the eastern stations (probably associated with the long raypath close to and in the slab), we obtained reliable results only for 4 station-events pairs. These are 4 events to station st01 of the BANJO network, which are shown in Figure 15. We plot the
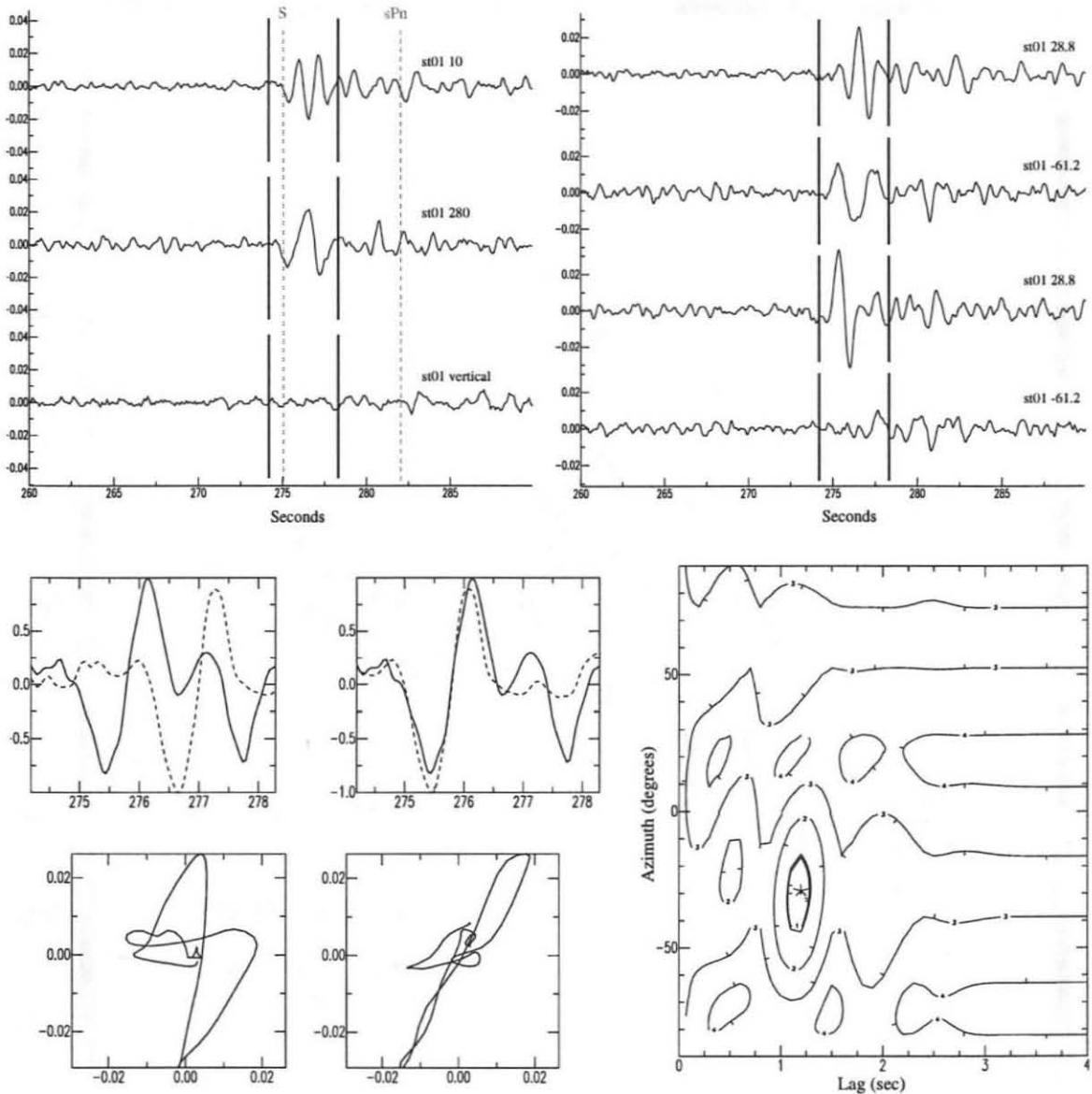
Figure 14: Same as Figure 3 for BANJO station st01 and a deep local S recording.

vectors at the intersection point of the ray with the slab, because we believe that the anisotropy is most likely beneath the slab, as we will explain in the next section. Figure 16 shows the raypaths of these waves with respect to the slab (surface interpolated from the contours of Figure 1).
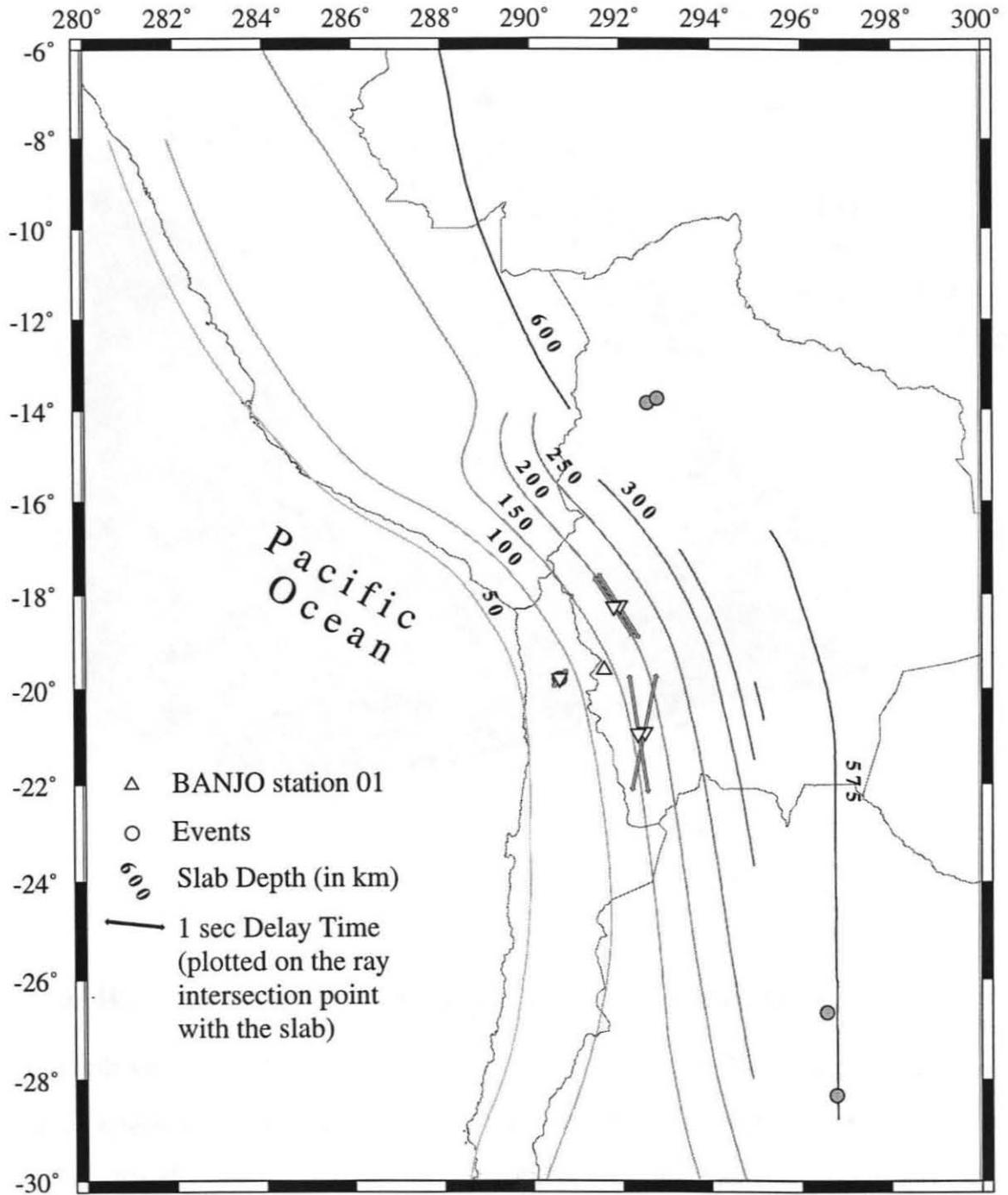
Figure 15: Results from local deep S splitting for events to station st01 of the BANJO network. Arrows are plotted on the ray intersection point with the slab. Westernmost event is shallow (intersection point is plotted on the event location).
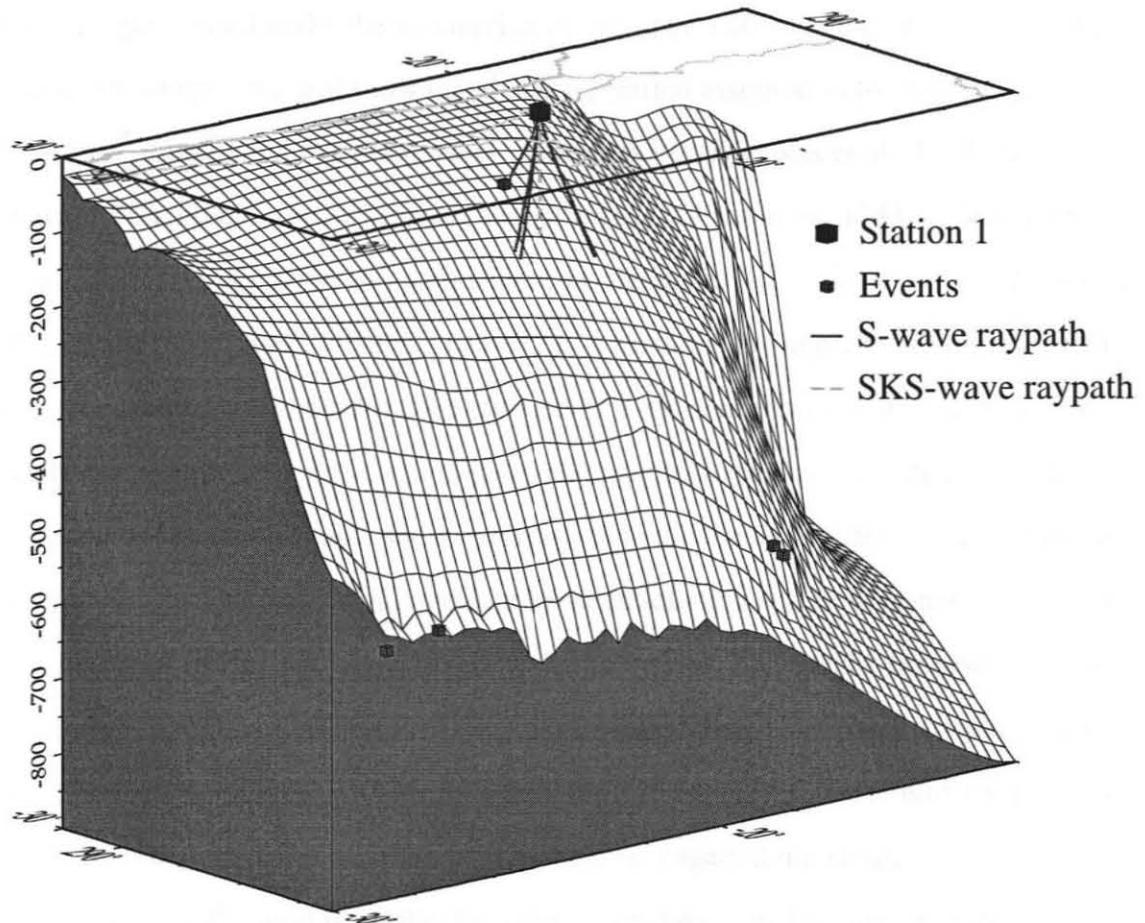
Figure 16 : Raypath geometry for events plotted in Figure 15. The shaded surface is interpolated from the slab contours in Figure 1.

Shear Wave Splitting and Anisotropy in the Upper Mantle

The Earth's upper mantle shows significant seismic anisotropy, due to the preferred crystallographic orientation ("lattice preferred orientation") adopted by its minerals in response to deformation. Thus, the measurement of shear wave splitting parameters can provide us with information about the flow and/or stress patterns in the upper mantle.

However, several important steps have to be made before we can relate these splitting parameters to deformational patterns. First, we have to know the relationship between between splitting and anisotropy, then between anisotropy and strain and finally between

strain and tectonic/geologic processes. The relation between splitting and anisotropy is fairly straightforward under the assumption of one or two homogenous anisotropic layers (later in this chapter we will show that this is a justified assumption for the regions we investigated). Secondly, from laboratory measurements (Nicholas et al., 1983; Zhang and Karato, 1995), observations of mantle xenoliths (e.g., Christensen, 1984; Mainprice and Silver, 1993; Ji et al., 1994) and theoretical considerations (e.g., MacKenzie, 1979; Ribe, 1989; Chastel et al., 1993), there appears to be a remarkably simple relation between the a-axis concentration and the structural frame: the a-xis concentration of mantle samples is usually contained within the foliation plane and parallel to the lineation direction. Recent experimental results on simple shear deformation in olivine aggregates suggests that the a-axis concentration may be intermediate between foliation and flow planes and that for large strains (> 150%) it will tend to follow the flow plane. This would, however, introduce only a slight obliquity of perhaps 10 degrees (sometimes seen in natural samples) with respect to the foliation plane.Thus, for a horizontal lineation direction (either vertical or horizontal foliation plane) and for a near-vertical propagation direction, the fast-polarization direction is parallel to the lineation direction. The third relationship is the least well-known in this problem. However, several observations have been made which give us some clues about the relation between strain and tectonic/geological processes. From measurements in ultramafic tectonites, it has been shown that the lineation direction ,and hence the olivine a axis concentration, is usually oriented subparallel to the spreading direction. (Christensen, 1984). The rapidly accumulating data on SKS anisotropy in orogenic areas point to a dominant orientation of the fast-polarization direction parallel to the trend of mountain belts (Silver, 1996). Thus, by combining laboratory measurements with observations from the field as well as previous measurements of shear wave splitting, we can deduce mantle deformational regimes consistent with our splitting results.

Interpretation

To understand the implications of these splitting measurements on the anisotropy and ultimately the geodynamics of the Nazca plate subduction zone, we need to distinguish several areas where the splitting might have originated. The local shallow and intermediate depth S-wave measurements constrain the above-slab component of the anisotropy. There appears to be very little coherent splitting in the crust: stc1 and stc2 show hardly any splitting for two events almost directly under the stations at 50 km depth. However, this is also where the crust is thinnest. Receiver functions point to a 70 km deep crust under the central BANJO stations, but unfortunately, there were no shallow events in this region. Previous studies have shown that most of the crustal anisotropy arises from cracks in the top 10 km, so that crustal splitting should not be a function of crustal thickness. For the intermediate-depth events we find larger delay times of up to .35 sec for the western and central stations when corrected for non-vertical raypath.

The overall fast polarization direction of the anisotropy is in the NS direction, which places an important constraint on the flow/deformation field in the mantle wedge. In particular, it is inconsistent with the traditional model of two-dimensional corner flow. This model has a very simple anisotropic prediction, namely a fast direction that is parallel to the relative plate motion direction, which is nearly EW (e.g., Ribe, 1989). Any kind of 'delamination' of the upper plate should also produce the same EW direction. On the basis of the NS direction, neither of these options appears likely. The NS directions can be simply explained by the EW shortening that is occurring in the process of making the Andes. Geologic estimates of shortening (see Russo and Silver, 1996), GPS estimates of shortening across the Andes (Norabuena et al. 1998), and stress directions tabulated in the World Stress Map (Zoback, 1992), all show that the direction of contemporary shortening is EW. As with other compressional zones, such as Tibet (McNamara et al., 1994), the directions of ϕ are orthogonal to the shortening direction. From the data that presently exist on active convergent margins, it appears that the fast polarization direction is controlled by

the sense of strain in the overlying plate (either trench-normal shorting or trench-normal extension), rather than the mantle flow field (see Silver, 1996).

The contribution of the slab and subslab mantle are constrained by the deep local S waves and the *KS phases. The slab itself appears to contribute little to the anisotropy. There are two expected directions for the stations that we have examined: a fossil direction of +45°, based on the orientation of fracture zones, and EW, corresponding to the APM direction of the Nazca plate. There are no stations that yield this former direction, and the latter direction could account for the EW observations of the BANJO stations, but not for the other stations that are at a high angle to EW. We therefore conclude that the slab contribution is negligible.

Assuming the anisotropy extends no deeper than 400 km (limit of olivine stability field), the *KS stacks should be representative of the region below the slab for the western and central BANJO and SEDA stations, and for the above-slab region for the eastern BANJO stations. We can draw several conclusions (see Figure 17): first, because the eastern BANJO stations show EW fast directions, and the splitting intermediate-depth local events show an NS fast direction and much smaller delay times, there must be an abrupt change in anisotropic properties above the slab close to the location of stations st06/st07: NS directions for ϕ and small delay times to the west, EW directions and larger delay times to the east. Examination of both body wave (Myers et al., 1998) and surface wave tomography (van der Lee et al., 1998) reveal this location to be the probable boundary between Andean-related deformed mantle to the west and stable Brazilian craton to the east. The splitting found for the most eastern BANJO stations, as well as those further to the east (James et al., 1995), suggest that the Brazilian craton is characterized by directions that are roughly consistent with those found east of station st07.

Finally, the deep local S waves should experience most of the splitting beneath the slab, because the above-slab component of the raypath is constrained to be small, compared to the measured delay time. We thus take the intersection point of the ray with the slab and a
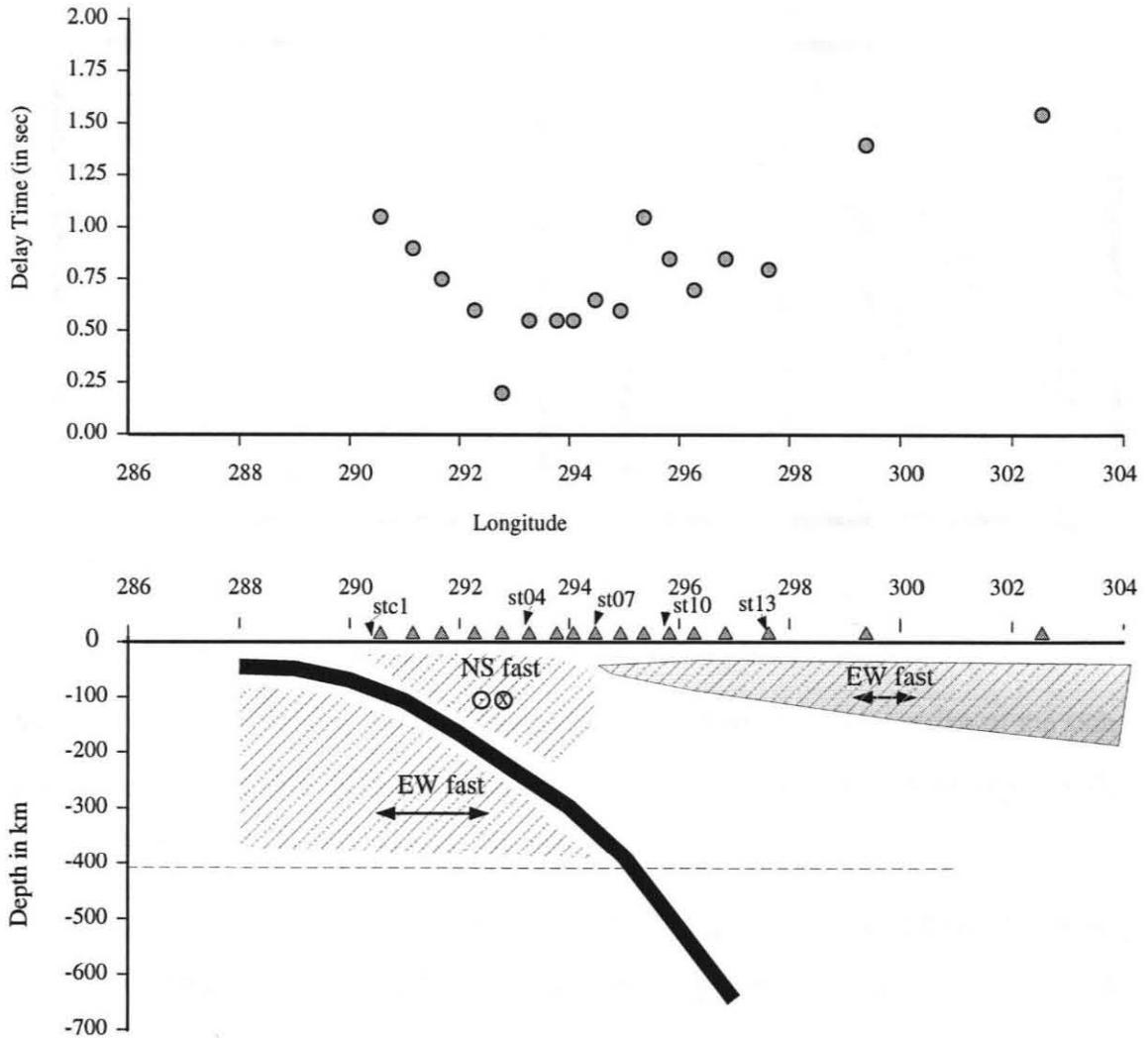
Figure 17: Delay time for BANJO network as a function of longitude and
suggested model of anisotropy in this region. Rightmost station is station
ptmb from Brazilian study (James et al., 1995).

few hundred kilometers below, as the likely location of the anisotropy. Since the slab itself

probably does not contribute to the measured splitting, the actual source of the anisotropy

should be more than 50 km deeper than this intersection point. The fact that these delay

times are greater than those of the *KS stacks, can be attributed to the non vertical raypath

through the anisotropic region. Calculations show (Figure 18) that the fast polarization

direction measured at the receiver should not differ much from the symmetry-axis

direction, based on models using symmetrized olivine (Keith and Crampin, 1977) and
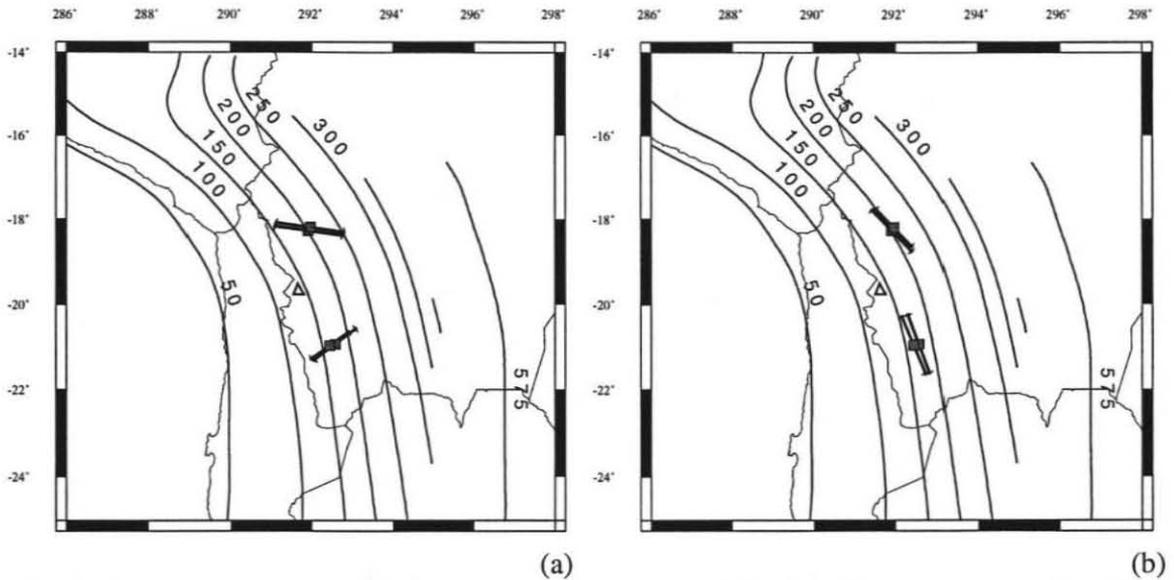
Figure 18: Predicted splitting measurements for (a) a slab entrained model, (b) a trench parallel model. Triangle shows location of st01.

assuming that the symmetry axis is either horizontal and parallel to the strike of the slab (trench-parallel), or parallel to the APM direction with a plunge equal to the apparent dip of the slab. The difference is perhaps 10-20 degrees.

A simple model for below-slab anisotropy is shown in Figure 19. It consists of an EW strip of material 150 km wide with an EW trending symmetry axis. Both north and south of this strip, the symmetry axis is horizontal and parallel to the local strike of the slab. One important question is whether such abrupt changes in anisotropy can be produced by such a deep below-slab model. Recent analysis by Rümpker (1998) has addressed this question, for the specific case of estimating apparent splitting parameters for a wavefield in the vicinity of a vertical discontinuity between two distinct anisotropic regions. He has generated a synthetic vertical wavefield for such a model, and has found that for waves with period of 6 sec, there exists a transition zone of about 50 km resulting from this boundary. The width is a very weak function of depth of the anisotropic discontinuity. It is, however, a stronger function of period. A strip 150 km thick with 50 km transition zones to the north and south could account for the observations. The only additional complication is that the rays are not exactly vertical, and as a result, rays arriving to each station sample roughly a
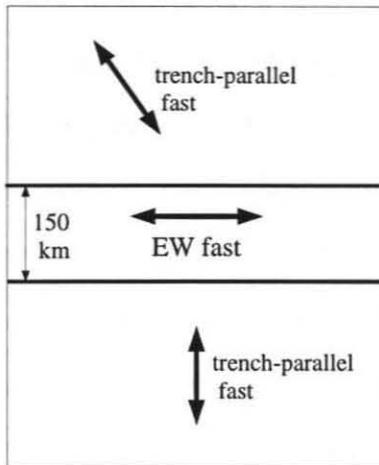
Figure 19 : Model of below slab anisotropy.

coned-shaped region around the station. However, for the northern transition zone, the SEDA stations only sample a region clockwise from south to east (see Figure 6), and since the southern station is located to the south-east of the northern one, their rays do not overlap. For the southern transition zone, st02 has only one ray coming from the south-east. However, this ray is from a local deep ScS phase, which would have a more steeply incident ray than the ones shown in Figure 8. Thus, there is again no overlap.

It is clear that no single process can account for this pattern. The pattern can not be explained solely by slab-entrained flow, as this would predict values of ϕ that are nearly parallel to the east-west absolute plate motion (APM) direction of the Nazca plate (Russo and Silver, 1994). A model of trench-parallel flow is more consistent with the SEDA observations, as well as the local deep-focus S observations at BANJO station st01. The pattern of flow from the retrograde slab model of Russo and Silver (1994) predicts trench orthogonal directions with southwards flow south of the stagnation point (or line) and northwards flow to the north of the stagnation point. The cause of this flow pattern is the retrograde motion of the slab, the decoupling of the slab and the underlying mantle, and a partial barrier to mantle flow at depth. The PISCO stations reveal a more complex pattern of both trench parallel and trench normal directions. These stations, however, have the fewest number of observations and we therefore place less weight on them in our

interpretation. In any event, a trench parallel flow model can not account for the EW trending stations of the BANJO network. It has been noted previously (Russo and Silver, 1994) that in regions with abrupt changes in dip, such as the zone beneath Peru, there is an abrupt change from trench parallel to trench normal values of ϕ. This could either be due to a contortion in the slab, with the flow field locally following the abrupt change in slab dip, or else a breach in the slab and flow through the slab at this point. In the zone beneath the BANJO stations, there is no indication of an abrupt change in slab dip. Yet this region possesses some very special qualities. In particular, the BANJO line almost exactly coincides with the symmetry line of the central Andean orogen as found by Gephart (1994), based on the shape of the topography and the subduction zone as defined by the Wadati-Benioff zone. The zone is also the center of the so-called Arica bend. The curvature of the bend in the slab of the continent and the slab itself has become accentuated over the last 30 my (Russo and Silver, 1996). We thus consider two possible explanations for the pattern beneath BANJO. The first is that the increasing curvature of the slab produces NS compression in the subslab mantle beneath the Arica bend, and consequently an EW value of ϕ. Another possibility is that Nazca slab has actually buckled along this line and there is a breach in the slab, with mantle material flowing through the slab. Both interpretations are supported by the modeling of Creager et al. (1995), who showed that the geometric constraints associated with the concave oceanward bend in the trench and Andes force along-strike compression in the subducting slab. At this stage there is no obvious sign of a breach, although the slab seismicity (or absence of seismicity) allows such a possibility (see Figure B1, Appendix B). Maps of Harvard CMT solutions in this region suggest that there exist rapid variations in focal mechanism in the general vicinity of the symmetry line (Figure 20). Two unusual normal faulting mechisms just north of the line might be suggestive of bending of the slab in this region. Additionally, there exist indications of anomalous volcanism in this area (Figure B2, Appendix B). More definite conclusions would require a detailed investigation of this area, which is beyond the scope of this chapter.
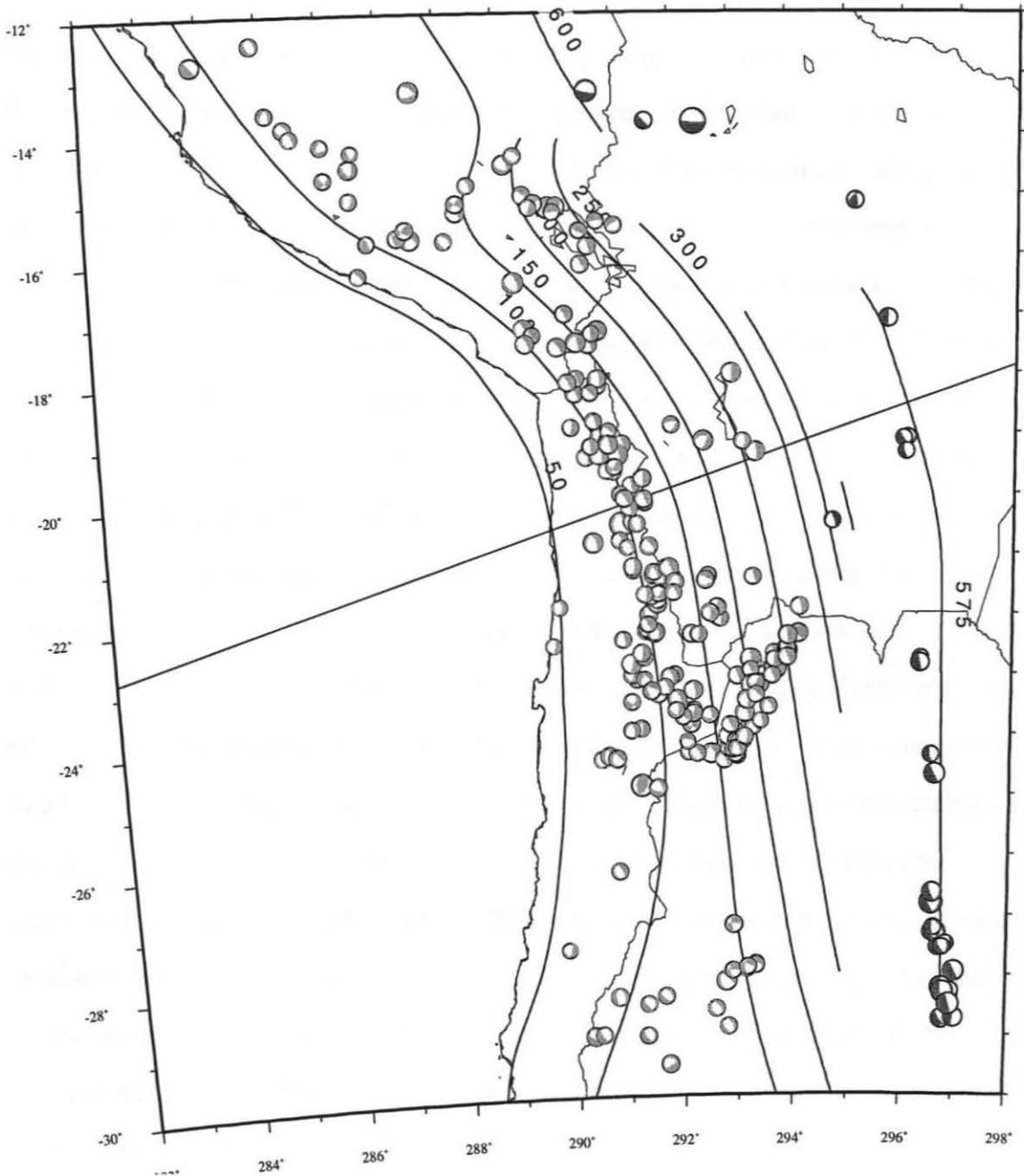
Figure 20: CMT solutions from Harvard catalog in area of interest. Light colored focal spheres are plotted for 100-300 km deep earthquakes and dark mechanisms for 300-700 km deep events. Symmetry line from Gephart (1994) is also plotted.

Comparison With Other Subduction Zone Studies

One of the principal results of interest from these splitting measurements is the direction of the fast shear wave polarization azimuth with the respect to the subduction zone and local geology. In recent years there have been several studies of subduction zone anisotropy, using both temporary a well as permanent network data, focussed on resolving this issue. Silver and Chan (1991) pointed out that most theories of mantle dynamics for convergent margins would predict that the fast shear wave direction is to be parallel to the relative plate motion between the downgoing and overlying plate, or in the absolute plate motion direction. Previous studies of the Kuril-Kamchatka subduction zone (Kaneshima and Silver, 1992; Fisher and Yang, 1994) have found a fast shear wave azimuth sub-parallel to the convergence direction, as have Fischer and Wiens (1996) for the Tonga subduction zone. However, most of these studies have limited depth resolution and/or sample only the region above the subducting slab rather than below. As summarized by Kaneshima and Silver (1993), the delay times observed above the slab, in the mantle wedge, are generally small, in the same range as crustal values (0.1 -0.3 sec), although values approaching 0.5 sec have been found. The observed fast polarization directions appear to reflect the state of strain in the above slab wedge, being parallel to transpressional features in compressional back-arc environments (Shih et al., 1991; Fouch and Fisher, 1996) and parallel to the extension direction in the case of back-arc extension (Fouch and Fisher, 1996). No evidence has been found for the manifestation of the traditional mantle wedge model of corner flow.

Other observations of shear-wave splitting for studies concentrating on flow below the subducting slab have found fast directions sub-parallel to the strike of subduction, e.g., Vinnik and Kind (1993) for the Kurile-Kamchatka subduction system, Fouch and Fischer (1996) for the NW Pacific, as well as Gledhill and Gubbins (1996) for the Hikurangi subduction zone of New Zealand, indicating that this below slab flow model may be dominant in the world's subduction zones.

Conclusions

We have examined the depth dependent anisotropy of the Nazca plate subduction zone, by determining the fast polarization directions and delay times of teleseismic SKS, SKKS and PKS phases, as well as local ScS and intermediate to deep S waves, from the data from three temporary broadband experiments (BANJO, SEDA and PISCO).

We find no evidence for corner flow above the subducting slab, with mostly trench parallel fast directions and small delay times for local intermediate depth S phases. This direction is orthogonal to the direction of contemporary maximum compressive horizontal stress, according to the World Stress Map, which would agree with the alignment of the fast olivine axis under this stress field. However, we see a clear change in character, going from West to East, which can be interpreted as the edge of the Brazilian craton, with strong EW aligned fast direction and bigger delay times for the eastern BANJO stations.

Below slab fast directions vary from orthogonal to the trench for the BANJO stations to parallel for the SEDA and PISCO stations. We interpret these directions in terms of the retrograde flow model of Russo and Silver (1994). This model can be viewed as the flow field resulting from a plate (or slab) slowly falling down and rolling back to the West. In this situation, the BANJO stations may be situated right above a breach in the slab, or a point in which there is north-south compression induced by an increasingly curved slab.

Acknowledgments

References

Ando, M. and Y. Ishikawa, Observations of shear-wave velocity polarization beneath

Honshu, Japan: two masses with different polarization in the upper mantle, J. Phys. Earth, 30, 191-199, 1982.

Cahill, T. and B.L. Isacks, Seismicity and shape of the subducted Nazca plate, J. Geophys. Res., 97, 17503-17529, 1992.

Christensen, N.I., The magnitude, symmetry and origin of upper mantle anisotropy based on fabric analyses of ultramafic tectonites, Geophys. J. R. Astron. Soc., 76, 89-111, 1984.

Fischer, K.M. and D.A. Wiens, The depth distribution of mantle anisotropy beneath the Tonga subduction zone, Earth Planet. Sci. Lett., 142, 253-260, 1996.

Fischer, K.M. and X. Yang, Anisotropy in the Kuril-Kamchatka subduction zone structure, Geophys. Res. Lett., 21, 5-8, 1994.

Fouch, M.J. and K.M. Fischer, Mantle anisotropy beneath northwest Pacific subduction zones, J. Geophys. Res., 101, 15987-16002, 1996.

Gephart, J.W., Topography and subduction geometry in the central Andes - Clues to the mechanics of a noncollisional orogen, J. Geophys. Res., 99, 12279-12288, 1994.

Gledhill, K. and D. Gubbins, SKS splitting and the seismic anisotropy of the mantle beneath the Hikurangi subduction zone, New Zealand, Phys. Earth Planet. Inter., 95, 227-236, 1996.

Kaneshima, S. and P.G. Silver, Anisotropic loci in the mantle beneath central Peru, Phys. Earth Planet. Inter., 88, 257-272, 1995.

Keith, C.M. and S. Crampin, Seismic body waves in anisotropic media; synthetic seismograms, Geophys. J. R. Astron. Soc., 49, 225-243, 1977.

Kind, R., G.L. Kosarev, L.I. Makeyeva and L.P. Vinnik, Observations of laterally inhomogeneous anisotropy in the continental lithosphere, Nature, 318, 358-361, 1985.

Mainprice, D. and P.G. Silver, Constraints on the interpretation of teleseismic SKS

observations from kimberlite nodules from the subcontinental mantle, Phys. Earth Planet. Inter., 78, 257-280, 1993.

McNamara, D.E., Owens, T.J., Silver, P.G., and F.T. Wu, Shear wave anisotropy beneath the Tibetan Plateau, J. Geophys. Res., 99, 13655-13665, 1994.

Nicolas, A. and J.P. Poirier, Crystalline Plasticity and Solid State Flow in Metamorphic Rocks, Wiley, London/New York, 444 pp, 1976.

Ribe, N. M., Seismic anisotropy and mantle flow, J. Geophys. Res, 94, 4213--4223, 1989.

Rümpker G. and P. G. Silver, Apparent shear-wave splitting parameters in the presence of vertically-varying anisotropy, Geophys. J. Int., submitted, 1998.

Russo, R.M. and P.G. Silver, Trench-Parallel Flow Beneath the Nazca Plate from Seismic Anisotropy, Science, 263, 1105-1111, 1994.

Savage, M. and P. G. Silver, Mantle deformation and tectonics: Constraints from seismic anisotropy in western United States, Phys. Earth Planet. Int., 78, 207-227, 1993.

Silver, P.G., Seismic anisotropy beneath the continents: Probing the depths of geology, Annu. Rev. Earth Planet. Sci., 24, 385-432, 1996.

Silver, P.G. and W.W. Chan, Implications for continental structure and evolution from seismic anisotropy, Nature, 335, 34-49, 1988.

Silver, P.G. and W.W. Chan, Shear wave splitting and subcontinental mantle deformation, J. Geophys. Res., 96, 16429-16454, 1991.

Silver, P.G. and M.K. Savage, The interpretation of shear-wave splitting parameters in the presence of two anisotropic layers, Geophys. J. Int., 119, 949-963, 1994.

Vinnik, L.P. and R. Kind, Ellipticity of teleseismic S-particle motion, Geophys. J. Int., 113, 165-174, 1993.

Zoback, M.L., 1st-order and 2nd-order patterns of stress in the lithosphere - the World Stress Map project, J. Geophys. Res., 97, 11703-11728, 1992.

Chapter 3:

Anisotropy Beneath California:

Shear Wave Splitting Measurements Using

a Dense Broadband Array

Abstract

We have determined shear wave splitting patterns for the western United States. We found that the overall pattern of fast directions agrees very well with that of the Pn anisotropy model by Hearn (1996). In general, this measured fast direction is orthogonal to the maximum horizontal compressive stress direction shown in the World Stress Map (1997). This suggests that the pattern of anisotropy is generally uniform in the crust and lithospheric mantle, in a layer with an overall thickness of 100 to 150 km, as estimated from the SKS delay times. This implies that this upper mantle layer has experienced a similar stress condition and deformational history. The alignment of most fast directions can be explained by plate-tectonic, extensional and compressional events.

A more detailed investigation revealed small-scale lateral variations between closely located stations for the same event, and also between SKS and SKKS for station-event pairs and evidence of vertical variations of anisotropy. We grouped stations for which enough data were available according to the behavior of splitting parameters as function of polarization azimuth. Group 1, largely consisting of stations in and to the west of the Los Angeles basin, does not show any variation with azimuth. Group 2, consisting of stations close and to the east of the San Jacinto fault can be fit better with a 2 layer model, including a thin

layer in which the fast direction is parallel to the San Andrea Fault (SAF -parallel anisotropy) on top of a thicker layer in which the fast direction is EW (EW-fast layer). Station SVD, located on the SAF, shows smaller variations and is not part of this group, needing only a very thin upper layer. However, the variation with polarization azimuth of these two groups is small and thus the assumption of a single anisotropic layer is adequate. Finally, Group 4, Berkeley stations close to the Hayward and San Andreas faults, was fit with a model with a thicker layer of SAF-parallel anisotropy on top of an EW-fast layer. However, because of the many free parameters involved in fitting, many other models are possible. Because of the limited constraints available for an inverse calculation, a better approach would involve the construction of physically realistic forward models and checking the fit with the data.

When more data and more stations become available in the southern California region, with the expansion of the TriNet array, the dividing lines between the different groups can be drawn more precisely. This will give a better indication of the lateral extent of the two layer anomaly and whether it can be interpreted as in terms of processes associated with the San Andreas fault system or another explanation is more likely.

Introduction

Shear wave splitting results obtained from teleseismic SKS waves give us important information that can be used to examine seismic anisotropy and the related history of deformation of the strain field. Measurements of anisotropy are one of the few tools available to seismology that can tell us about the current or past dynamics of the deeper Earth, especially its upper mantle (Kind et al., 1985; Silver and Chan, 1991). California, in particular, is an interesting region dynamically because of its plate tectonic complexities. The western United States is also one of the most seismographically densely covered regions in the world, enabling a detailed investigation of the local anisotropic parameters

and their geographical variation.

Our interest is in the lithospheric (and asthenospheric) pattern of anisotropy and its relation to the shallow and surfacial measurements of stress that have been performed over recent years. This study re-examines earlier work by Savage and Silver (1993), Ozalaybey and Savage (1995) and Liu et al. (1995), and adds many more stations and more data at stations used in those papers. We also investigate lateral variations of anisotropy, as well as vertical variations (e.g., two anisotropic layer models). The previous studies found evidence for alignment of the fast direction of anisotropy in a direction parallel to the San Andreas fault (SAF-parallel anisotropy) in the crust and upper mantle, as well as a deeper EW oriented fast direction (EW-fast anisotropy). This feature was interpreted as the asthenospheric flow in the slabless window left behind the Farallon plate.

Method

The method we used for measuring the anisotropic parameters of fast polarization direction and delay time has been described briefly in the previous chapter and in detail in Silver and Chan (1991). Our data set consists of TriNet, Anza, Berkeley and United States Seismic Network broadband recordings of SKS and SKKS phases, mainly from deep events along the western Pacific rim. Previous authors (Savage and Silver, 1993; Ozalaybey and Savage, 1995; Liu et al., 1995) have examined a small subset of this data. We have re-analyzed (and re-interpreted) some of these data, and added a substantial new data-set, consisting of more events and newly installed stations. The combined stations of these four networks (Figure 1 and Appendix C) form a dense seismic array that is ideally suited for the investigation of lateral variations of anisotropy. Also, this large data-set provides convincing evidence for the interpretation of shear wave splitting as being caused by anisotropy and not lateral structural inhomogeneities, if consistent splitting parameters are found over a wide geographic area.
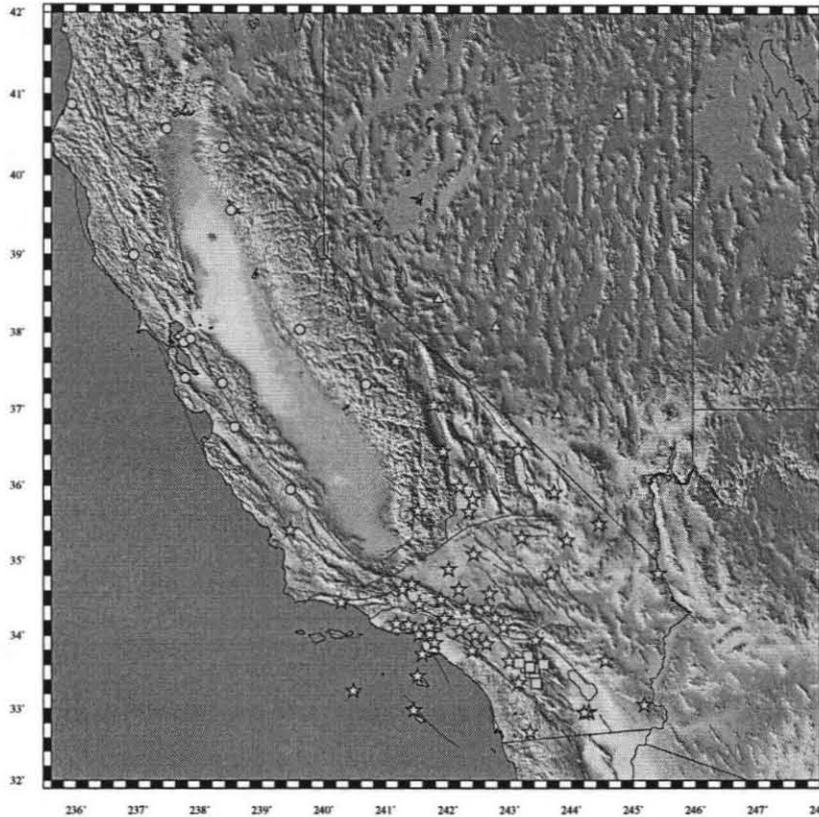
*Figure 1 : Map of stations used in this study. Stars indicate stations of
the TriNet network, circles Berkeley Network , triangles USSN network
and the squares show the Anza network stations.*

For many of these stations we were able to obtain data for only a small number of events,
either because of data availability problems (USSN and Anza) or because the station has
only been active for a short duration of time (TriNet). However, because part of the TriNet
network has been active for almost a decade as the TERRAscope network, we have stations
for which better azimuthal coverage can be obtained, and that can be used as "calibration
points". This means that in our interpretation we will assume that, barring any discrepancies
in the existing observations between the stations, simple splitting parameters for the well
covered station (no variation with back-azimuth) suggest that the nearby located station
probably also sees an anisotropically uncomplicated region.

Unfortunately, in this region we are at one clear disadvantage from South America (Chapter 2), in that there are no S-waves from local deep and intermediate-depth earthquakes we can use to obtain more information about the variation of anisotropy with depth. Studies of local shallow S-waves of 15 km and up suggest that anisotropy in this part of the crust is limited to a delay time of about 0.2 sec or less (Li et al., 1994). Further depth resolution can be obtained from comparing splitting characteristics of closely located stations.

Data

To illustrate the quality and coverage of the data, Figures 2(a) and (b) show the transverse component of the data collected for a recent (September 1997) deep event near Fiji, before and after correction for anisotropy, using our measurements of fast direction and delay time. These traces were filtered with a very broadband Butterworth bandpass filter between 1 and 100 sec to eliminate the long-period noise present in the records of some stations.

The data quality shown in Figure 2 is representative of the events we used. In general, most of the selected events had deep source depths which enhanced the sharpness and signal to noise-ratio of the SKS or SKKS arrival. No events were found in the back-azimuthal range of 20 to 180 degrees that were suitable for the measurement of reliable splitting parameters. We were able to use measured splitting parameters from other events to correct for the predicted splitting in data from this range, and found that the corrected data showed no sign of a transverse signal above noise level. This indicates that this data is also consistent with the measured splitting parameters.

For two stations, it proved impossible to measure reliable splitting parameters, e.g., well-constrained error ellipse, clear elliptical particle motion before correction and linear afterwards, and good signal to noise-ratio, even when taking into account a possible rotation of the waveform away from the back-azimuthal direction. These two stations, ISA (we took into account that the horizontal components for this station were originally not N
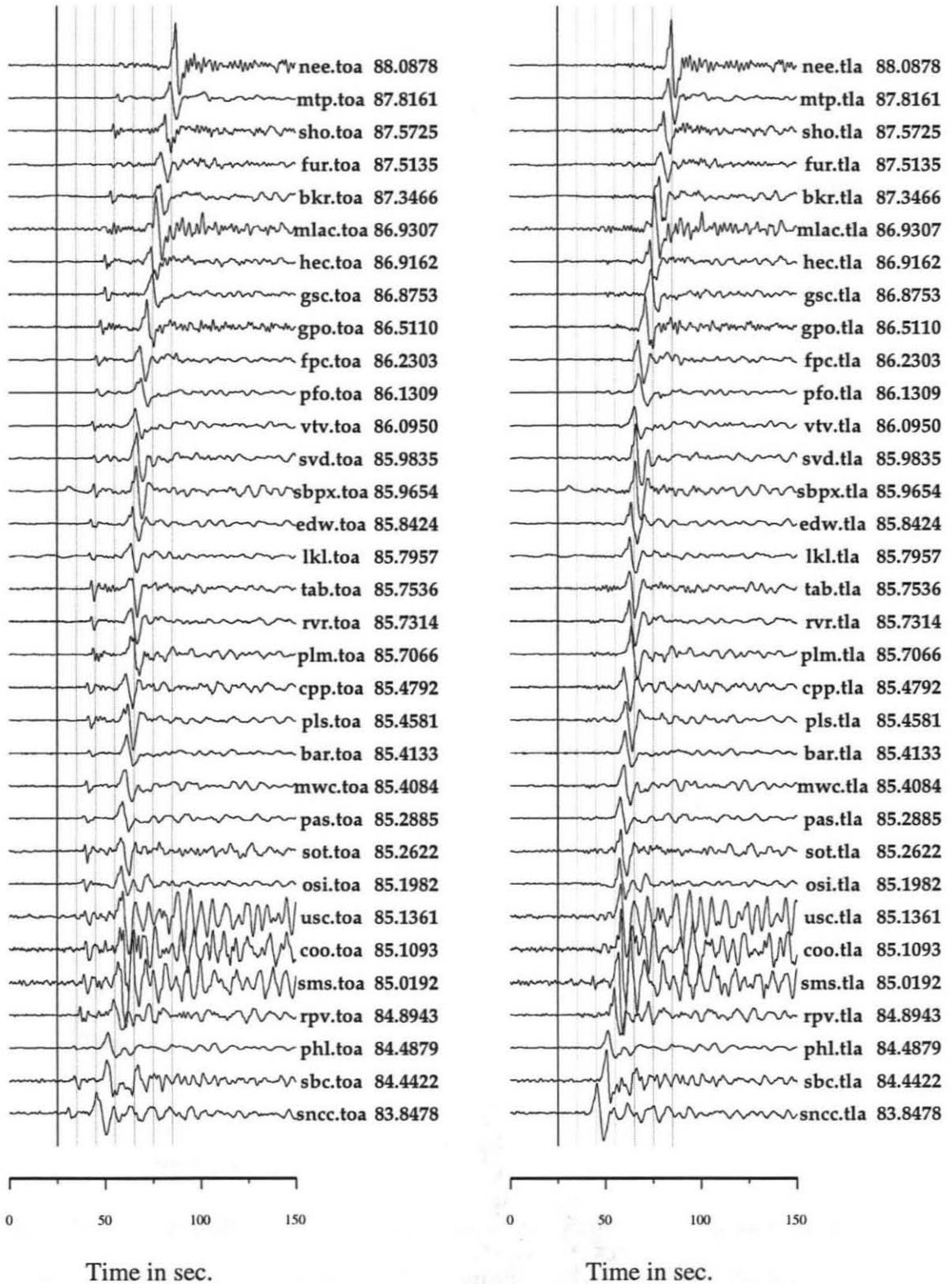
Figure 2(a): Record section of original (left) and corrected (right)

transverse components for a deep event near Fiji, recorded by TriNet.

Numbers to the right of the traces give the epicentral distance in

degrees. Traces are aligned on the origin time of the event.
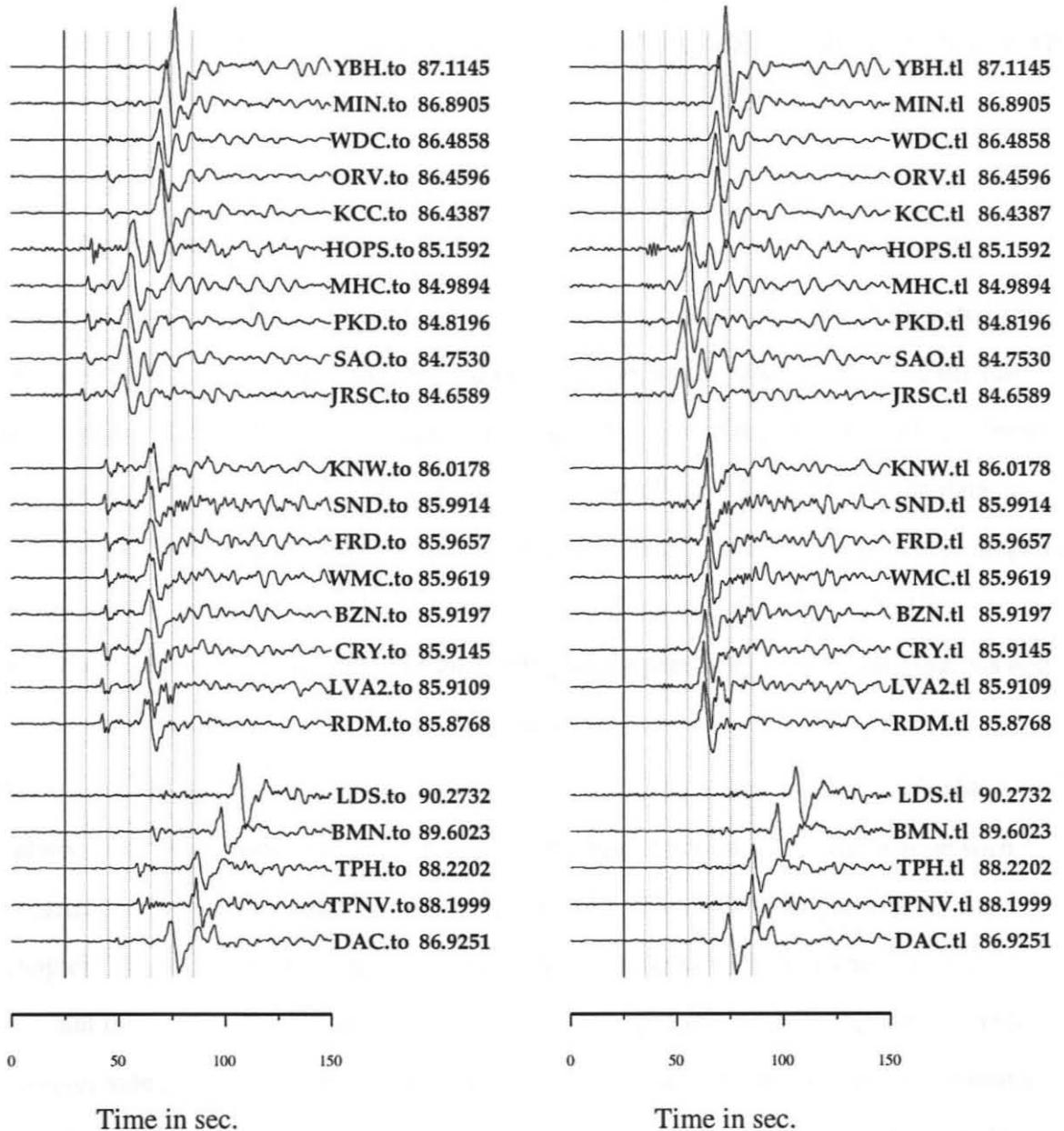
Figure 2(b): Like 2(a) for the Berkeley, Anza and USSN network stations
(from top to bottom).

and E aligned) and MLAC, are located above some of the greatest known crustal and

upper mantle velocity anomalies in the western United States, namely the Isabella anomaly

(e.g., Raikes, 1978) and the Mammoth Lakes Volcanic region, respectively. We believe

that these lateral heterogeneities in the upper mantle beneath the stations caused great

complexity in the waveforms and made reliable anisotropy measurements impossible. For all other stations, however, we were able to perform at least one high-quality SKS splitting measurement.

The Big Picture

In Figure 3 we first plot all determined fast directions and delay times (from this study) for the western U.S.. The delay times are indicated by the length of the arrows and the fast direction by the direction of the arrows. In general, these results are consistent for almost all stations. Small variations were found, and because of the high quality of the data, a detailed analysis can be performed, which we will focus on in later sections of this chapter. In this section, however, we will focus on the overall picture of the western U.S. anisotropy. For clarity, we provide figures of splitting parameters for smaller regions and include station names on the maps in Appendix C.

We do not give single splitting values for every station, because there are resolvable (although in most cases small) differences in the fast direction and/or delay time with polarization azimuth and angle of incidence, as we will show in later sections of this chapter. Thus, an average value would not be representative and would not take into account this extra information. If an average value were to be used in the correct ion for receiver side anisotropy, e.g., in the analysis of transverse isotropy near the core-mantle boundary using S phases, significant and in most cases avoidable errors may be made.

In the southern California region west of the San Andreas, all stations show a consistent EW fast direction, with delay times varying between 1 and 1.5 seconds. This range of delay times implies a layer of anisotropic material of 100 to 150 km thick with 4% anisotropy, a value thought typical for sheared mantle rock. A small crustal contribution may be included; studies of crustal anisotropy in this region suggest delay times smaller than 0.1 to 0.3 sec (Li et al., 1994). To investigate the relationship between these anisotropic splitting
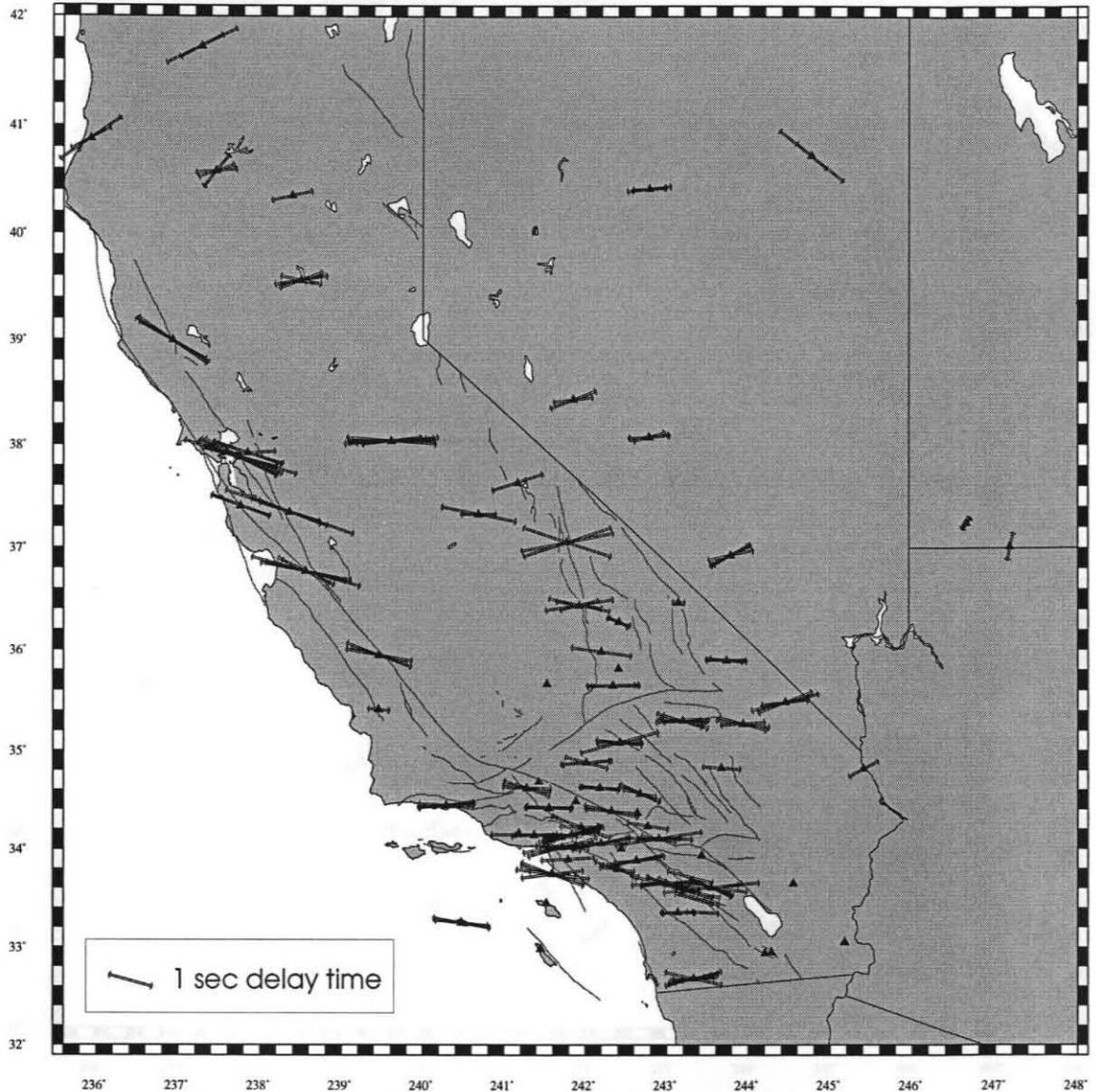
Figure 3: Map of all splitting measurements (from this study). Arrows are plotted on the station locations, their direction indicates fast direction and their length is proportional to delay time. Major California fault systems are also shown. More detailed maps including station names can be found in Appendix C.

parameters and the crust further, we plot Figure 3 again, but now include the measurements of maximum compressive stress direction from the World Stress Map (1997) in Figure 4. These directions were determined mostly from borehole break-outs and crustal focal mechanisms, and thus give an indication of the very shallow, crustal stress regime in the
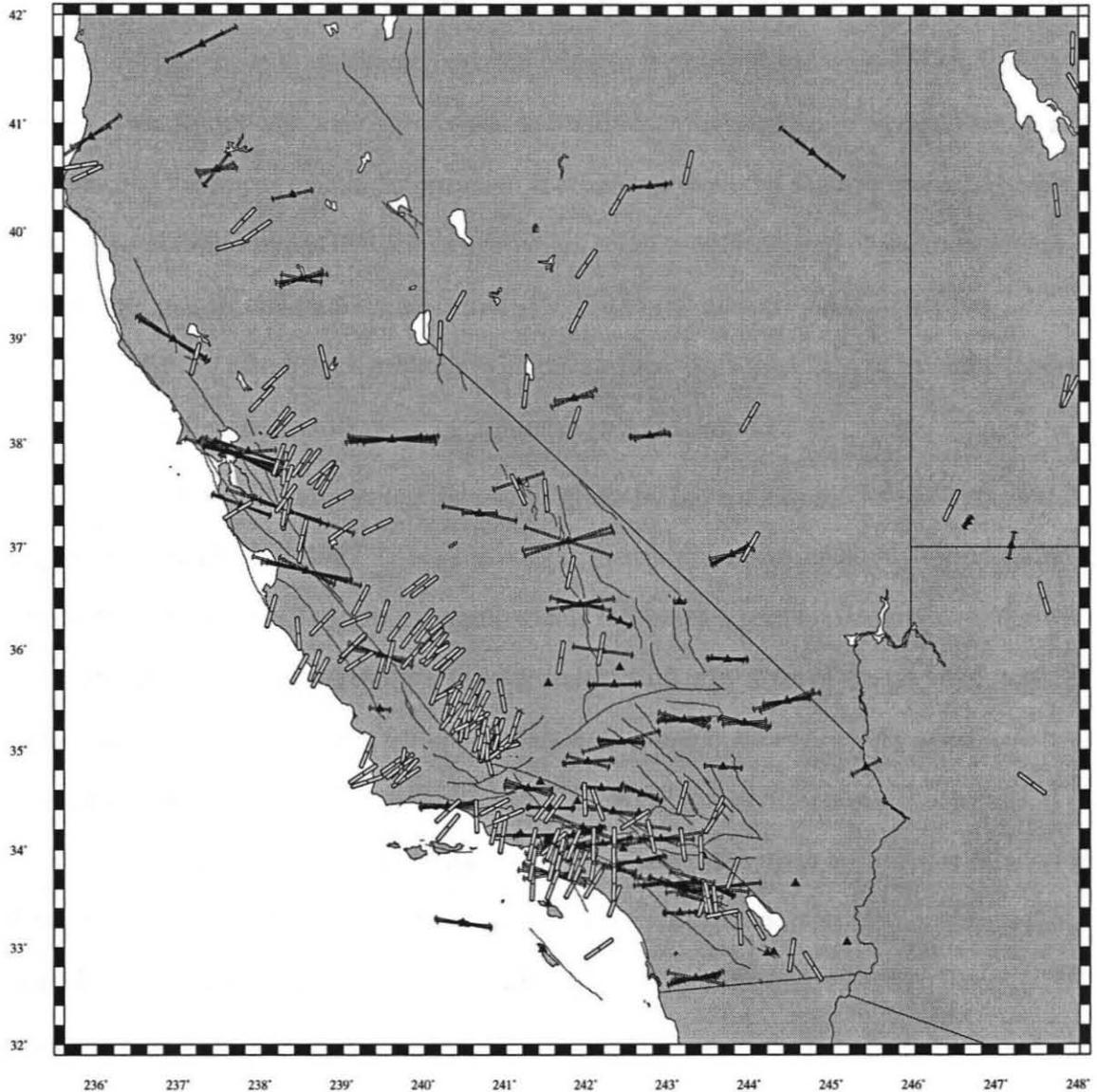
Figure 4: Map of splitting parameters and high quality World Stress
Map stress indicators. WSM stress indicators are plotted in white
arrows in the direction of maximum horizontal compressive stress. Only
A and B quality measurements are used.

area. We only used those measurements which were given an A or B quality rating. Many

studies of transpressional collision zones have found that the measured fast splitting direc-

tion is aligned with the transpressional zone (e.g., McNamara et al. 1994; Silver et al., 1993

and see Silver, 1996, for an overview). Thus, the fast direction is orthogonal to the

maximum compressive stress in these regions. Overall, we find that there is a correlation

between the World Stress Map (WSM) vectors and our determined fast directions, in that most seem to be close to orthogonal to each other in the central and southern California regions. This agrees with the observations in transpressional regions described earlier, and suggests that the upper mantle deformation is consistent with the shallow stress indicators. This interpretation implies that the fast direction reflects deformation of the mechanical lithospheric mantle and thus suggests that 100-150 km of anisotropic material has experienced stress conditions coherent with the surface. This thickness of the lithosphere is greater than the 80 km estimated by Humphreys and Hager (1990).

Another useful comparison for our data-set is given by the anisotropic Pn tomography (Figure 5) from Hearn (1996). These anisotropic measurements sample only the uppermost mantle lid, whereas SKS splitting measurements represent a vertical integral over the whole upper mantle. These results should correlate well only if there are no large vertical variations in anisotropy within the upper mantle. In general, there is a very good correlation between the Pn fast velocity and SKS splitting fast directions. Since the direction of the fastest P-wave velocity in olivine,which is the main anisotropic mineral in the upper mantle, is aligned with the a-axis of olivine, and the polarization direction of the fast SKS wave also coincides with this a-axis, these two directions should be the same if the same material is sampled.

In central California we find fast directions of about N60. The measurements for stations HOPS, BRIB, BKS, MHC, JRSC, SAO and PKD are all very consistent with each other, and show some variation with back-azimuth (more about this in later sections of this chapter). Interpretation of the splitting parameters for these stations is more difficult. Previous authors have focussed on the proximity of these stations to the SAF to explain these results; however, stations at similar distances from the SAF in southern California do not show this amount of complexity, suggesting that it is more likely a regional problem.

In southern California as well as the Basin and Range and the Mojave Desert, we find mostly EW directed fast direction and delay times varying between 1 and 1.5 seconds. In
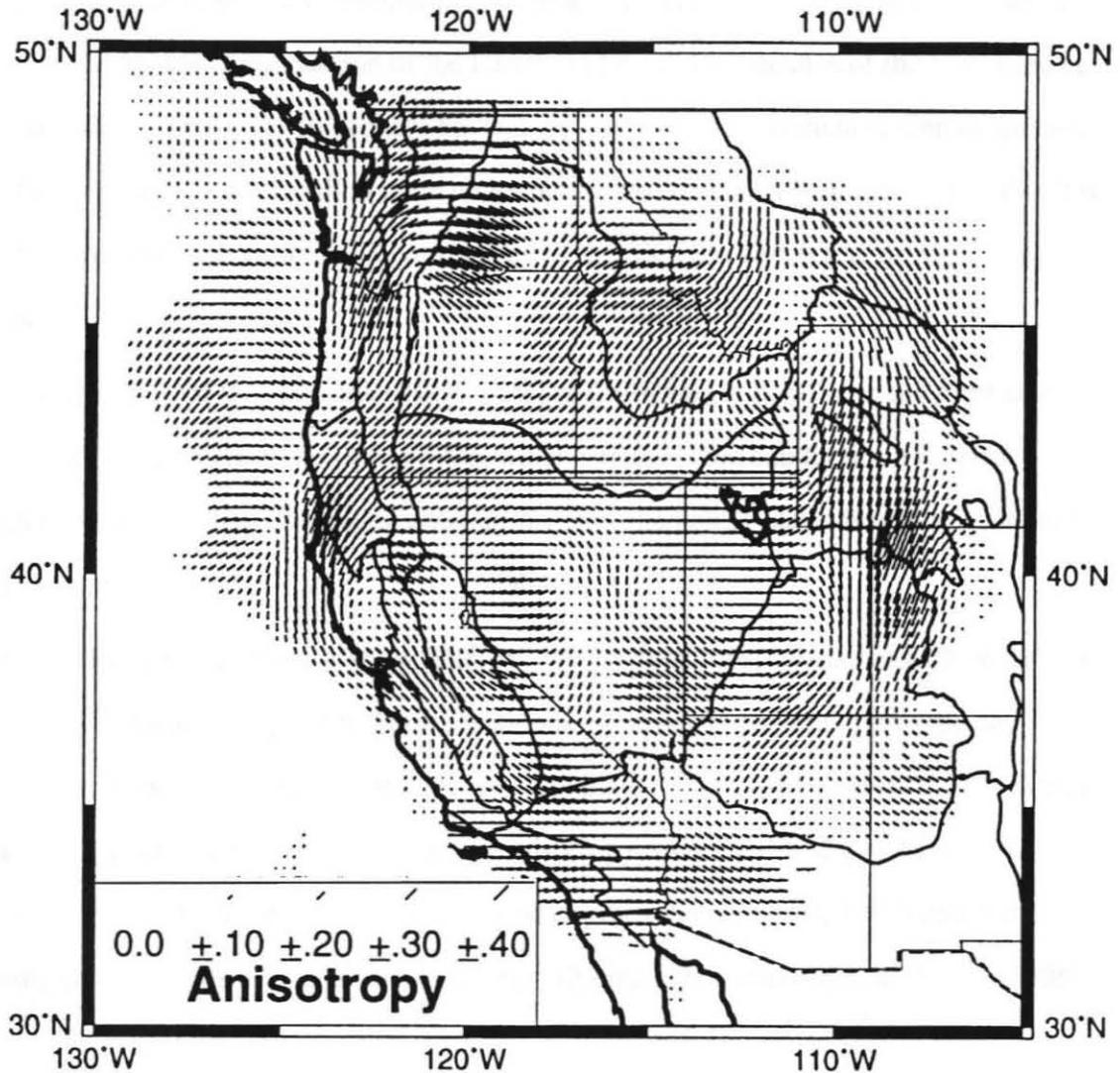
Figure 5: Pn anisotropy model from Hearn (1996). The line segments
are drawn parallel to the direction of highest velocity and the line
segment length is proportional to the amount of anisotropy.

the case of simple shear, a mineral will align its principal slip system with the direction of

shear (Ribe, 1989; Zhang and Karato, 1995), which requires the least energy. For olivine

the principal slip direction coincides with the a-axis and thus also with the fast splitting

direction. In the case of California and the San Andreas Fault system, this mechanism

would predict alignment of the fast direction with the SAF. The measured EW fast

direction thus indicates that shear at the plate boundary does not dominate the deformation

in this area. This EW anisotropic orientation is perpendicular to the late Cenozoic

north-south compression in southern California (Liu et al., 1995). Alternatively, this direction could be due to subduction of the Farallon plate, either because of the EW directed shear induced on the asthenosphere beneath the continent, or remnant frozen in anisotropy in the remnants of the Farallon plate under the North American plate. However, this last hypothesis does not explain the consistency of the SKS, Pn and WSM directions in this area.

The orientation of the fast direction in northern California is parallel to the northeast subduction direction of the Gorda plate, which suggests that subduction-related deformation (NE-SW directed internal shearing of the Gorda plate) is responsible for the anisotropy observed at stations YBH, WDC and ARC.

The western Nevada stations show ENE-WSW fast directions, consistent with observations made by Savage et al. (1990). This direction is inconsistent with both present-day extension (-60 to -80 degrees) and the absolute plate motion (+55 degrees). However, this fast direction can be interpreted as fossil anisotropy associated with pre-Miocene extension, of which the direction is about 68 degrees (Savage et al, 1990) under the assumption that the a-axis of olivine alligns with the extension direction (Silver, 1996).

Detailed Analysis

Regional Consistencies/Separate Station Analysis

One diagnostic which is of particular interest is the variation of splitting measurements with back-azimuth, especially for the data from stations close to the San Andreas fault, which have been previously interpreted with models of two-layer anisotropy (Savage and Silver, 1993; Ozalaybey and Savage, 1995). To investigate this variation closely, we re-analyzed all events given in the Table of Ozalaybey and Savage (1995), provided by the authors as an electronic supplement, for several key stations. The first station we investigated was station PAS (Figure 6), located in Pasadena, about 40 km west of the San
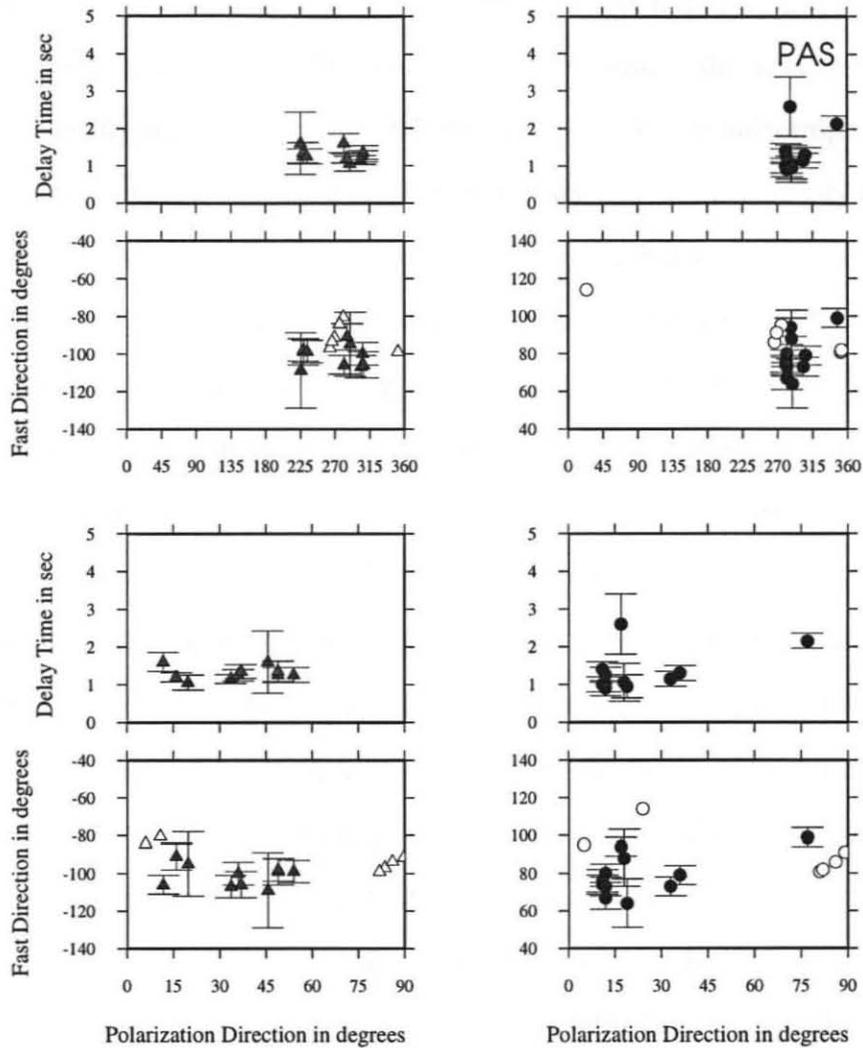
Figure 6: High-quality measurements of fast direction (φ) and delay time
(δt) as a function of polarization direction (φ_p) modulo π/2 (bottom 4
panels) and back-azimuth (top 4 panels) for station PAS. Solid triangles
represent measurements done in this study from SKS or SKKS, while
closed circles show measurements from Ozalaybey and Savage (1995).
Open symbols represent null-measurements.

Andreas Fault (Figure 1, Appendix C). Our measurements are plotted in Figure 6, and for

comparison we also plot the SKS and SKKS measurements from Ozalaybey and Savage

(1995) (from here on this paper will be referred to as OS95). We have chosen not to use the

S-wave splitting measurements because of known problems with this phase, including

possible contamination by source side anisotropy, and deep mantle transverse isotropy.

We plot these measurements in Figure 6 as a function of back-azimuth, to show the event coverage, and also as a function of ϕ_p (polarization direction, so the direction of particle motion in the horizontal plane) modulo $\pi/2$. In the case of double anisotropic layers, we would expect the estimated splitting parameters to vary with $\pi/2$ periodicity as a function of ϕ_p (Silver and Savage, 1994). It is clear from this figure that station PAS shows no sign of double-layer splitting. The measured fast direction is very consistent, and although there are some variations of delay time with ϕ_p, this can not be attributed to double layer splitting, because of the consistency in fast direction, and can be more easily explained in terms of small lateral variations in the strength of anisotropy, since these rays do not all sample the exact same region. We will discuss this in more detail later in this Chapter, when examining the variations in splitting parameters between different stations and between SKS and SKKS. Several events from OS95 have been omitted from our set of measurements because of a low signal to noise ratio of the data, and the unreliability of the measurements. An example of data that was not used in our analysis is shown in Figure 7. In general, however, our conclusion about this station agrees with theirs, in that this data can be interpreted as single layer, EW fast, anisotropy, with an average delay time of about 1.2 sec. Several other stations for which data was available for a range of back-azimuths showed similar results: USC, RPV, CMB and BAR fast directions and delay times had no significant variation with back-azimuth. Most of these stations, however, did not have as many good signal-to-noise ratio events as station PAS.

Station SVD of TriNet (Figure 8) is particularly interesting because it is located almost on top of the San Andreas fault system. This station was modelled by OS95 with a double anisotropic layer, partly based on the results for another nearby station, but because of a lack of more measurements, interpreted as having a lack of fault-parallel anisotropy. The overall anisotropy can be described as EW fast direction, with an average delay time of about 1.2 sec, which is overall very similar to station PAS. Although there is a sizeable gap of about 30 degrees in our data coverage, the obtained measurements show a very similar

Event:1991.56   Sta:PAS   Dist:104.1   Az:14.8   Baz:346.4   40.400N   79.200E   33.0km
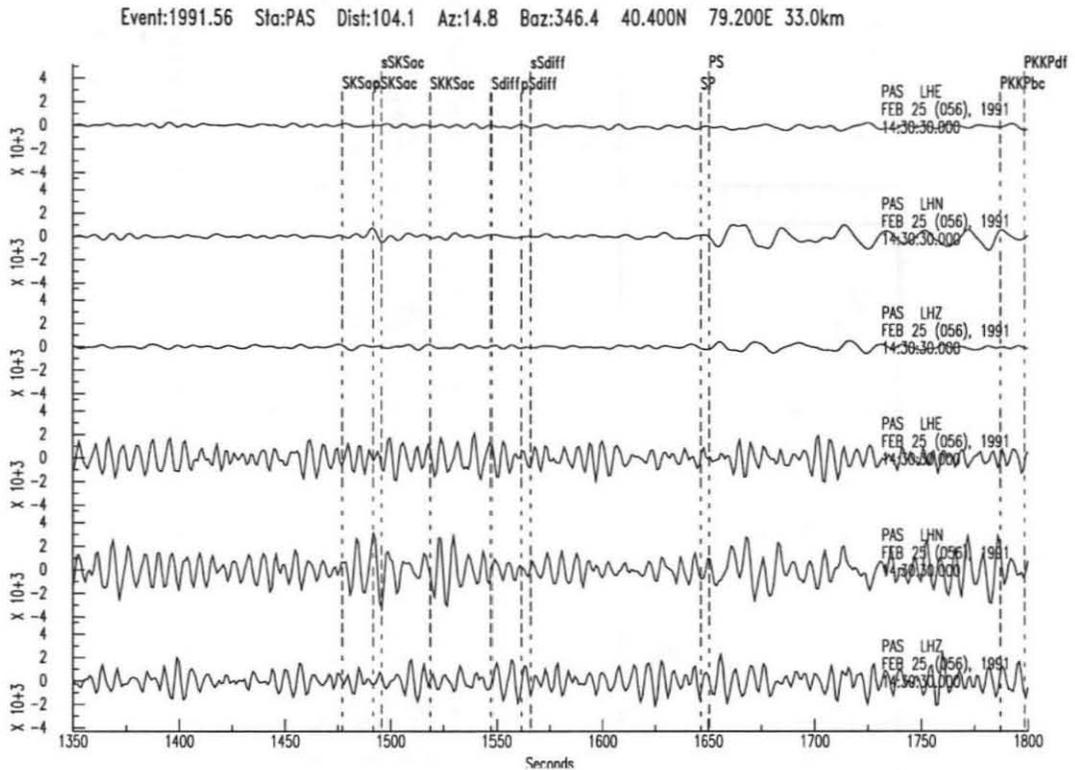
Figure 7: Example of PAS data used in OS95, but omitted from this study. The bottom three traces have been bandpass filtered between 1 and 100 sec (as the traces in Figure 2), the upper traces between 10 and 100 sec.

fast direction for all back-azimuths. Delay times, however, seem to consistently decrease with polarization azimuth. We computed the curves for the two layer models suggested by OS95, based on observation at stations PFO and LAC (models A and B, respectively, in Table 1), for a frequency of 0.1 Hz and included these in Figure 8. We also include our own forward model (model C) to give an indication of the range of models that fit the data. A model with a thin layer on top of the overall anisotropic pattern of EW aligned fast polarization direction, and 1.20 seconds of delay time, explains the data quite well. However, to the first order, the assumption of a one-layer model is adequate. This thin, fault parallel, upper layer could represent the effect of finite strain associated with the relative plate motion between the North American and Pacific plates. A delay time of 0.30 sec or less could reside in the crust.
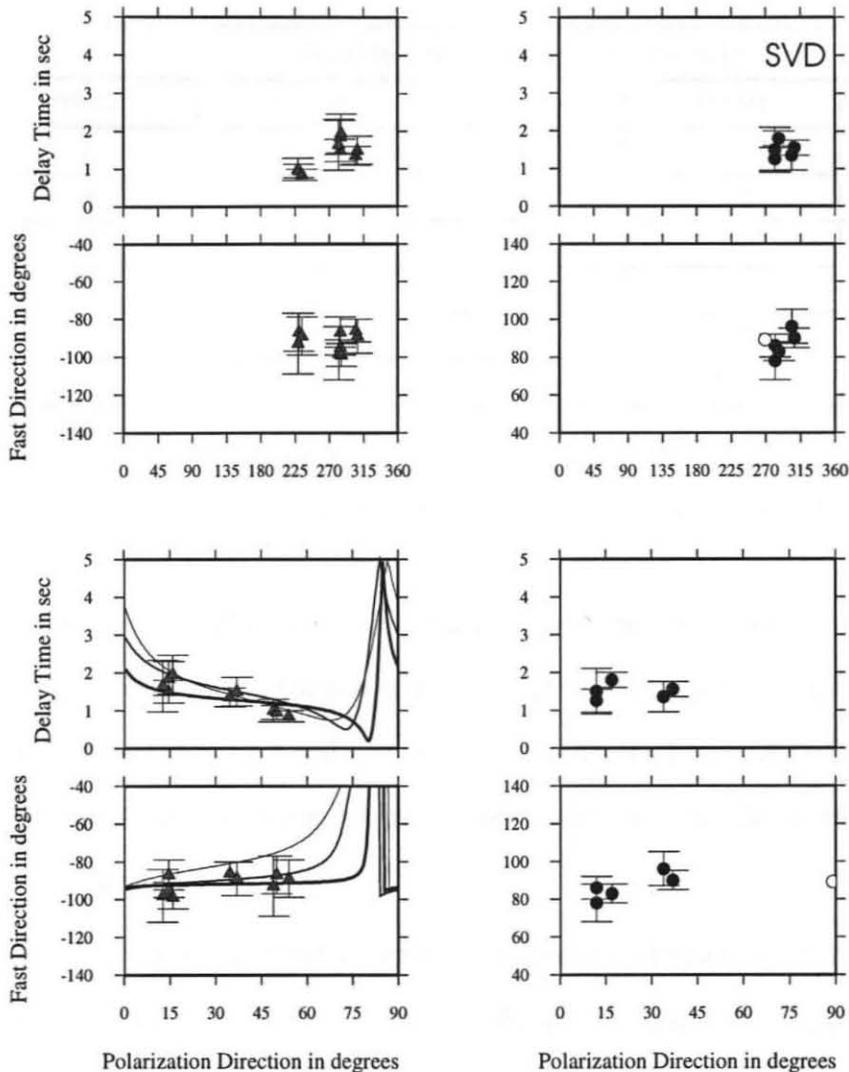
Figure 8: As Figure 6, for station SVD. Curves in bottom left 2 panels

correspond to two layer models A (thinnest line), B and C (fattest line) in

Table 1.

Station PFO has been modeled in various papers with different results (Liu et al., 1995;

OS95; Helffrich et al., 1994). In Figure 9 we present the most complete data set yet. We

have added data from stations GSC, VTV and DGR, which show the same general trend.

These stations show indications of double layer splitting: a decrease of delay time and an

increase in fast direction with increasing polarization azimuth. This general trend is fit

quite well, with the forward model D. Again, a thin layer is added on top of the EW fast

layer, which fits the stations to the west. Since this model seems to extend to stations at

more than 100 km away from the SAF to the east, it is not necessarily related to the San

Double anisotropic layers models				
Model	ϕ_1 (deg)	δt_1 (sec)	ϕ_2 (deg)	δt_2 (sec)
A	70	1.20	110	0.60
B	50	0.80	105	1.10
C	80	1.20	120	0.20
D	80	1.20	140	0.50
E	90	1.40	135	1.00
F	90	1.40	135	0.70

Table 1: Models of two anisotropic layers used in the study. The $(\phi_2, \delta t_2)$
and $(\phi_1, \delta t_1)$ values correspond to splitting pairs of the upper and lower
layer, respectively.

Andreas Fault system. However, the fast direction of the top layer is more or less parallel to the direction which would be predicted by shear from this fault. Once more data is added for more stations to the west and east of the SAF (stations LUG, LKL, SBPX, EDW and FPC and more are already installed, but did not have many recorded events yet), this problem can be analyzed more precisely.

Another station for which OS95 suggested the presence of a two layered anisotropic structure is station BKS of the Berkeley network (Figure 10), also located close to the SAF at a distance of 40 km, in northern California. This station was modelled with an upper layer with fast direction locally parallel to the strike of the SAF (delay time of 1 sec) and a lower layer with EW fast direction (delay time 1.40 sec). The measurements for this station are very similar to those of stations SAO, MHC, PKD, JRSC and HOPS, all Berkeley network stations. A temporary network deployed in central California, close to station MHC, also shows results consistent with BKS (Hartog, 1998). These stations all yield splitting parameters that are indicative of an anisotropic system that is more complicated than the simple one layer model. Possible explanations for this more complex set of measurements include: a dipping symmetry axis, a double anisotropic layer system or a system of more complex vertically-varying anisotropy (Ruempker and Silver, 1998). The double layer model
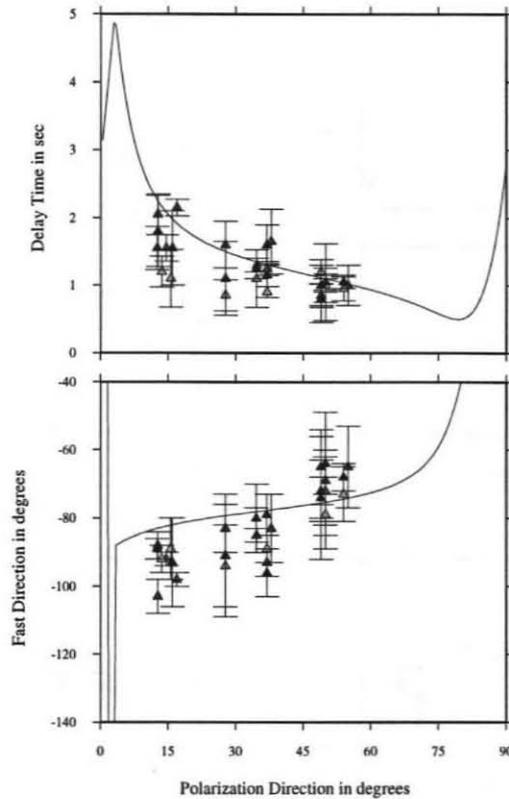
Figure 9: As Figure 6, for the group of stations of PFO, GSC, DGR and VTV. Line shows predicted two layer curves for model D in Table 1.

suggested by OS95 seems to fit the data quite well (Figure 10). This model consists of a lower layer with ϕ~90±27 degrees and δt~1.40±0.5 sec and an upper, fault parallel, layer of ϕ~135±25 and δt~1.00±0.50 sec. Because of the greater number of free parameters in this inversion, the trade-offs between the model parameters are quite large. We found that a model with only a 0.70 sec delay time in the upper layer could explain the data just as well (Figure 10). The range of possible models is so large that inverting for a model probably is not a reasonable solution to this problem; fitting the data with a physically realistic forward model is possibly a better method to pursue. This group of stations in central California showed the most clear signs of variation of splitting parameters with back-azimuth. Of course, for some stations, only a couple of measurements could be made, so the possibility of a complex anisotropic structure can not be excluded.
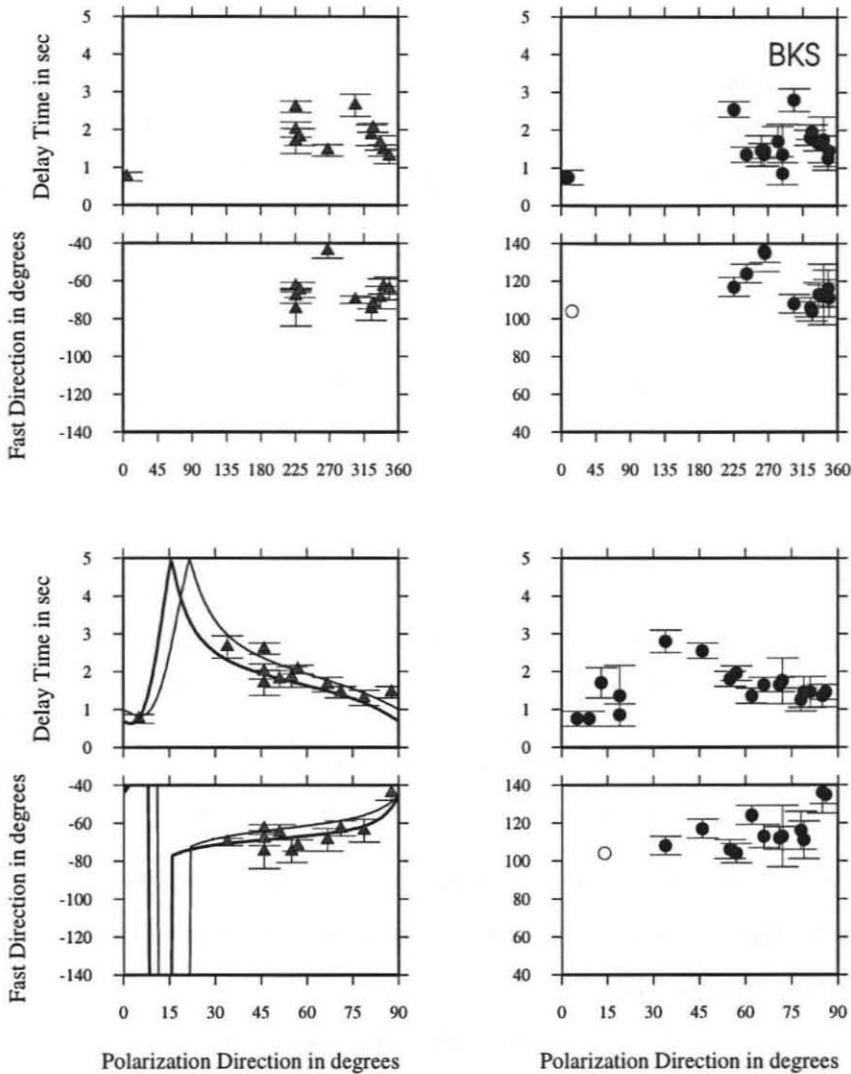
Figure 10: As Figure 6 for Berkeley station BKS. Thin line shows curves predicted by model E, fat line for model F (both in Table1).

SKS/SKKS Variation

Because of the high quality of this data-set, we were able to look at small variations in measurements using SKS and SKKS for the same event, to investigate the lateral heterogeneity in anisotropy. For a deep event near Sulawesi (Figure 11), the SKS recorded at PAS showed $\phi\sim77\pm12$ degrees and $\delta t\sim0.95\pm0.25$ sec, whereas SKKS measurements were determined at $\phi\sim72\pm8$ degrees and $\delta t\sim1.30\pm0.20$ sec. These fast directions are consistent, but the difference in delay time is resolvable, as the seismograms in Figure 11 show. We also
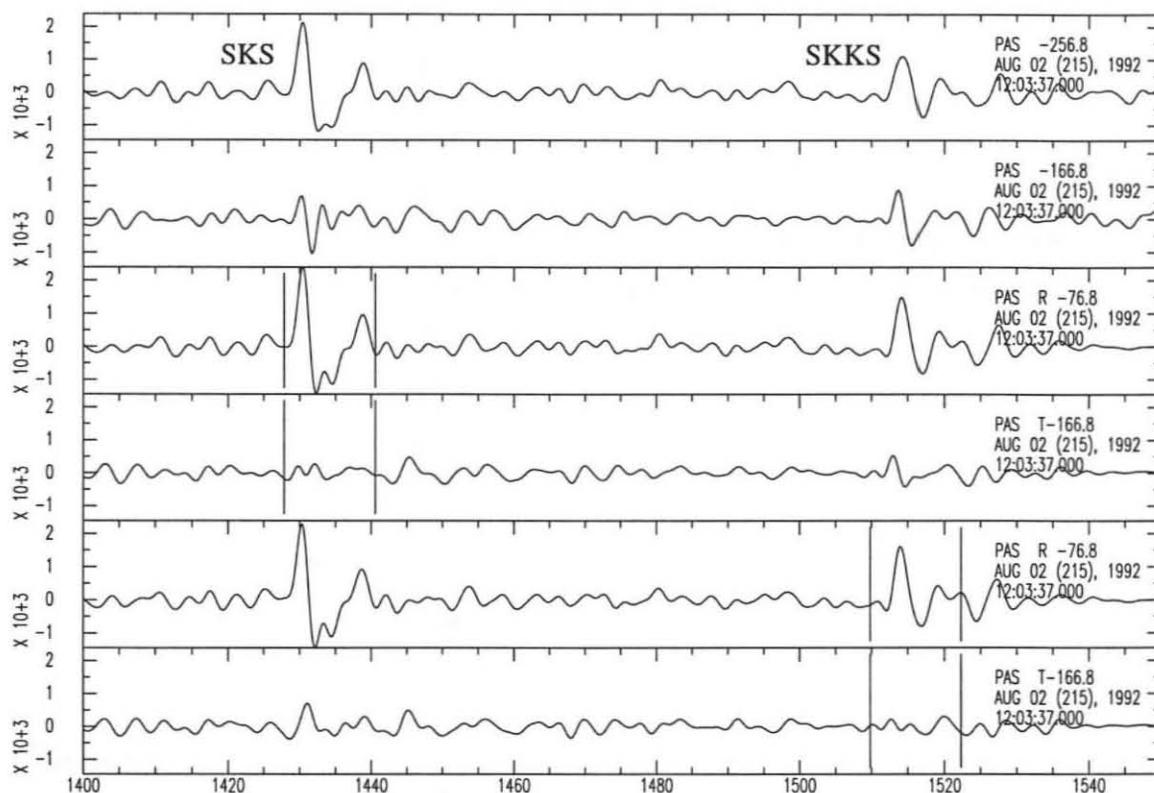
Figure 11: Top 2 traces: Original radial and transverse components seismgrams. Middle 2 traces: Radial and transverse seismograms after correction for SKS splitting. Bottom 2 traces: Radial and transverse seismograms after SKKS splitting correction.

attempted to stack the grids for the two phases, as described in Chapter 2, but found that the final result did not remove the transverse component for either phase. Unfortunately, this event occurred in 1992, when not many stations were on-line, but station GSC shows a similar delay time difference between the two phases. Another event, near Flores, showed similar results, in somewhat noisier data. This variation in delay time suggests that small variations of delay time with back-azimuth can also be expected, caused by lateral variations in the strength of anisotropy, since the rays sample slightly different regions (Figure 12).
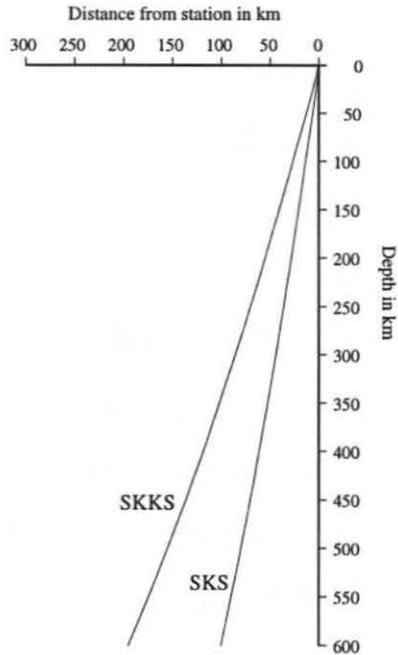
Figure 12: SKS and SKKS raypaths to station PAS for seismograms shown in Figure 11.

Conclusions

We have determined SKS and SKKS splitting measurements for more than 40 stations in the western United States. A comparison with shallow stress indicators, and a Pn anisotropy model for this region suggests that the overall deformational pattern which causes this anisotropic fabric may be pervasive and consistent throughout the crust and lithosphere. Most measured fast directions can be explained by plate tectonic processes or are consistent with late Cenozoic compressional (southern California) and pre-Miocene extensional (Basin and Range) events.

A detailed analysis of this data-set reveals signs of vertical anisotropy variations at some stations, and small but resolvable difference between SKS and SKKS splitting in the same event-station pairs. Most obvious is the variation of splitting parameters with polarization azimuth for stations of the Berkeley network in central California; these stations can be fit with a two-layer model, the upper layer with a fast direction of 135 degrees and delay time of 0.7 sec, the bottom layer with EW fast direction and a delay time of 1.40 sec. The top layer would fit with anisotropy aligned with shear on the SAF system, and the bottom layer

could be connected to past subduction. However, since the suite of models that can fit the data is so large, because of the number of free parameters, a more useful approach will involve the construction of several realistic forward models, and checking the fit with the data.

Other, much smaller, variations were seen in stations to the south. SVD can be fit better by including a thin layer with fast direction parallel to the SAF, on top of the overall EW fast direction, 1.2 sec delay time lower layer. Stations around and west of the LA basin show a consistent one layer model. Another group of stations close to and east of the SAF show some signs of vertical variation. Again, this could be due to a thin layer with a fast direction parallel to the SAF on top of the EW lower layer, but since the lateral extent of these stations extends to fairly great distance from the SAF, more stations should be analyzed to confirm these results and determine the total eastward extent of this anomaly.

Acknowledgements

References

Hartog, R., SKS splitting underneath central California
(http://emerald.ucsc.edu/~renate/SKS.html), 1998.

Hearn, T.M., Anisotropic Pn tomography in the western United States, J. Geophys. Res., 101, 8403-8414, 1996.

Helffrich, G., Silver, P.G., and H. Given, Shear-wave splitting variation over short spatial scales on continents, Geophys. J. Int., 119-561-573, 1994.

Humphreys, E.D. and B.H. Hagar, A kinematic model for the late Cenozoic development

of southern California crust and upper mantle, J. Geophys. Res., 95, 19725-19746, 1990.

Kind, R., Kosarev, G.L., Makeyeva, L.I. and L.P. Vinnik, Observations of laterally inhomogenous anisotropy in the continental lithosphere, Nature, 318, 358-361, 1985.

Li, Y.G., Teng, T. and T.L. Henyey, Shear wave splitting observations in the northern Los Angeles Basin, southern California, Bull. Seism. Soc. Am., 84, 307-323, 1994.

Liu, H., Davis, P.M. and S. Gao, SKS splitting beneath southern California, Geophys. Res. Lett., 22, 767-770, 1995.

Nicholas, A.N. and Christensen, N.I.C., Formation of anisotropy in upper mantle peridotites - a review, in Composition, Structure and Dynamics of the Lithosphere-Asthenosphere System, Geodyn. Ser. 16, edited by K. Fuchs and C. Froidevaux, 111-123, AGU Washington, D.C., 1987.

Ozalaybey, S. and M.K. Savage, Shear wave splitting beneath western United States in relation to plate tectonics, J. Geophys. Res., 100, 18135-18149, 1995.

Raikes, S.A., The temporal variation of tele-seismic P-residuals in southern California, Bull. Seism. Soc. Am., 68, 711-720, 1978.

Ribe, N.M., Seismic anisotropy and mantle flow, J. Geophys. Res., 94, 4213-4223, 1989.

Rümpker, G. and P.G. Silver, Apparent shear-wave splitting parameters in the presence of vertically varying anisotropy, submitted to Geoph. J. Int, 1998.

Savage, M.K., Silver, P.G. and R.P. Meyer, Observations of teleseismic shear-wave splitting in the Basin and Range from portable and permanent stations, Geophys. Res. Lett., 17, 21-24, 1990.

Savage, M.K. and P.G. Silver, Mantle deformation and tectonics:

constraints from seismic anisotropy in western United States, Phys. Earth Planet. Inter.,

78, 207-228, 1993.

Silver, P.G. and W.W. Chan, Shear wave splitting and subcontinental mantle deformation, J. Geophys. Res., 96, 16429-16545, 1991.

Silver, P.G. and M.K. Savage, The interpretation of shear-wave splitting parameters in the presence of two anisotropic layers, Geophys. J. Int., 119, 949-963, 1994.

World Stress Map (http://www-gpi.physik.uni-karlsruhe.de/pub/wsm), 1997.

Zhang, S. and S. Karato, Lattice preferred orientation of olivine aggregates deformed in simple shear, Nature, 375, 774-777, 1995.

Chapter 4:

Source Spectral Characteristics of Recent Large Shallow Subduction Zone Earthquakes and the Role of Sediments in Tsunami Excitation

Abstract

We have examined the source spectra of recent, shallow subduction zone earthquakes in the period range of 1 to 20 seconds, by computing the moment rate functions of teleseismic P-waves. After comparing the source spectral characteristics of 'tsunami earthquakes' with regular events, we found that the former have an anomalously low energy release in this frequency band, with respect to their moment magnitude, although their spectral drop-off is comparable.

Most earthquakes in this study conformed to the simple model of earthquake nucleation in a zone of compacted and dehydrated sediments, which ruptured up-dip until the stable sliding friction regime of unconsolidated sediments stopped the propagation. Sediment starved trenches, e.g., near Jalisco, can produce very shallow slip, because the fault material supports unstable sliding.

All tsunami earthquakes ruptured up-dip, with the centroid located close to the trench axis. These subduction zones all have a small size accretionary prism and a thin layer of subducting sediment. Ocean surveys show that the ocean floor close to the trench is highly faulted in these regions. We suggest that the horst and graben structure of a rough subducting oceanic plate will cause contact zones with the overriding plate, making shallow

earthquake nucleation and up-dip propagation to the ocean floor possible. The rupture partly propagates in sediments, making the earthquake source process slow.

Two factors have to be considered in the high tsunami generating potential of these events. First, the slip propagates to shallow depths, causing great deformation of the ocean floor. Second, the measured seismic moment may not represent the true earthquake displacement, because the elastic constants of the source region are not taken into account.

Introduction

In the last 10 years, several shallow subduction zone earthquakes have excited destructive tsunamis, giving rise to more than 1500 casualties in the period 1992-1994 alone. To mention just a few examples of these tsunamigenic earthquakes: the 1992 Nicaragua and Flores Island earthquakes, 1994 Kuril Island event and the 1996 earthquake of the coast of Peru.

In general, tsunamis are caused by large shallow earthquakes beneath the ocean floor. Thus the size of the event is one of the most important parameters to determine its tsunamigenic potential. A great shallow earthquake, of course, can always be expected to be followed by a substantial tsunami, caused by the displacement of water near the ocean floor. However, another subclass of earthquakes, "tsunami earthquakes," poses a special problem.

We will use the following definition of the term "tsunami earthquake" in the rest of this paper : an earthquake that directly causes regional and teleseismic tsunamis that are greater in amplitude than would be expected from its seismic moment magnitude. With this definition we exclude tsunamis caused by landslides which resulted from earthquakes, events that only locally caused big tsunamis, and we limit the definition to use moment magnitude and not surface wave magnitude, thus slightly modifying the definition given by Kanamori (1972) and excluding big events for which the surface wave magnitude saturates. Our primary interest in this paper is in comparing the source spectral properties of "regular" earthquakes with those of "tsunami earthquakes." We will also discuss the mechanism,

rupture direction, hypocentral location and tectonic setting of these earthquakes, in an attempt to investigate more closely the origin of the tsunamigenic potential of these events.

It has been well known from earlier investigations that one characteristic of tsunami earthquakes is the discrepancy between the surface wave magnitude and the moment magnitude of the earthquake (the M_S being much smaller). Since surface wave magnitude is determined by the energy in surface waves with a period of 20 seconds and the moment magnitude measurement is based on longer periods for big events, this is an indication of the greater energy release in longer periods (or the "slow" character) of these tsunami events. In addition to this line of evidence, there have been field surveys of first-person accounts, which describe the motion of the earthquake as being much more like a weak "rolling motion" than the usual impulsive character of comparable local events. In case of the Nicaragua earthquake, some felt a very feeble shock before the tsunami, with most not feeling the earthquake at all (Ide et al., 1993), and for the Java event earthquake-induced ground shaking was not experienced by the coastal residents interviewed in Bali and Java (Synolakis et al., 1995). In general, a tsunami earthquake is described as having a long source time function and a slow and smooth rupture. Several explanations have been proposed concerning the more efficient (with respect to its M_S) tsunami generating mechanism for these events, for example, the anomalously long source process time, which causes a large discrepancy between true seismic moment and conventional magnitude measurements made at shorter periods (Kanamori,1972), poor excitation of surface waves by nearly horizontal faults (Ward,1982) and sources in sedimentary rocks would produce larger tsunamis than sources in typical crustal rocks for given seismic moment (Okal,1988).

In this paper, we are interested in investigating the source spectra of shallow subduction zone earthquakes in a quantitative way, using broadband teleseismic P waveform recordings of worldwide seismic stations to determine the source spectra up to 1 Hz. We will then compare these source spectra with the moment found by centroid moment tensor

(CMT) inversion of very long period surface waves. We will also examine the other parameters found in this inversion and try to relate them to physical properties of the subduction zone where the earthquakes occurred.

Of particular interest here are four recent earthquakes that were followed by devastating tsunamis and have been termed tsunami earthquakes in previous studies: the 1992 Nicaragua event, the 1992 earthquake near Flores Island, the 1994 Java earthquake and the 1996 event near the coast of Peru. The 1992 Nicaragua earthquake was the first tsunami earthquake to be captured by modern broadband seismic networks. This earthquake caused about 170 casualties and significant damage to the coastal areas of Nicaragua. In Flores, a 1992 field survey of the north coast of the eastern part of the island showed that the first wave attacked the coast within five minutes at most of the surveyed villages; in total almost 2000 people were killed on Flores Island and neighboring Babi Island. The local tsunami height reached as high as 26 meters (Tsuji et al., 1995). The 1994 Java earthquake occurred off the southeastern coast of Java, near the east end of the Java Trench in the Indian Ocean, at 1:18 am local time. This event generated a devastating tsunami that took the lives of more then 200 East Java coastal residents. Runup measured along the southeastern East Java coast ranged from 1 to 14 m, while runup measured along the southwestern coast of Bali ranged from 1-5 m. (Synolakis et al., 1994). The 1996 Peru earthquake struck at 7:51 am local time, approximately 130 km off the northern coastal region of Peru. It created a tsunami that reached Peru centering on the city of Chimbote. Effects of the tsunami were observed from Pascasmayo, in the department of La Libertad, to the Port of Callao near Lima (International Survey Team, 1997). The tsunami was recorded by mid-Pacific tide gauges, 60 cm at Easter Island and 25 cm at Hilo, Hawaii. The aftershock pattern ranged from 120 to 180 km offshore near the Peru-Chile trench parallel to the Peruvian coastline.

Method and Data

In our analysis, we use teleseismic P waveforms recorded at worldwide broadband stations, which we obtained from the IRIS data center. The method to determine the source spectra is described in detail in Houston and Kanamori (1986) and we will only briefly outline it here.

The moment rate (source) spectrum is given by:

$$\left|\widehat{M}(f)\right| = \frac{4\pi\rho\alpha^3 \cdot R_E \cdot exp(\pi f t^*(\Delta)) \cdot u(f)}{g(\Delta) \cdot R_{\theta\phi} \cdot C \cdot \left|\hat{I}(f)\right|} \qquad [1]$$

where ρ and α are the density and P wave velocity at the source, R_E is the radius of the Earth, $g(\Delta)$ is the geometrical spreading factor, $R_{\theta\phi}$ is the radiation pattern factor, C is the free surface receiver effect, $t^*(\Delta)$ is the attenuation parameter, $I(f)$ is the instrument response and $u(f)$ is the spectrum of the observed P waveform.

We correct for station response (usually only the gain needs to be considered because of the broadband nature of the stations) and for attenuation with a distance dependent t^*, *with* $t^*=0.7$ at 50 degrees. The correction for the radiation pattern is applied for P, pP and sP phases, but since these three phases are usually difficult to separate for shallow large earthquakes, the correction is applied for the combined phases following the method of Boore and Boatwright (1984) and Houston and Kanamori (1986). The receiver site correction is computed for P wave incidence at the free surface. These corrections are appropriate only at shorter periods (e.g., shorter than around 20 seconds). At the very long period end, we will use the seismic moment determined with the centroid moment tensor inversion, which uses very long period (3-7.5 mHz) surface wave data. To obtain the average moment rate function of the event, we average the corrected spectra in a logarithmic sense and obtain the standard deviation.
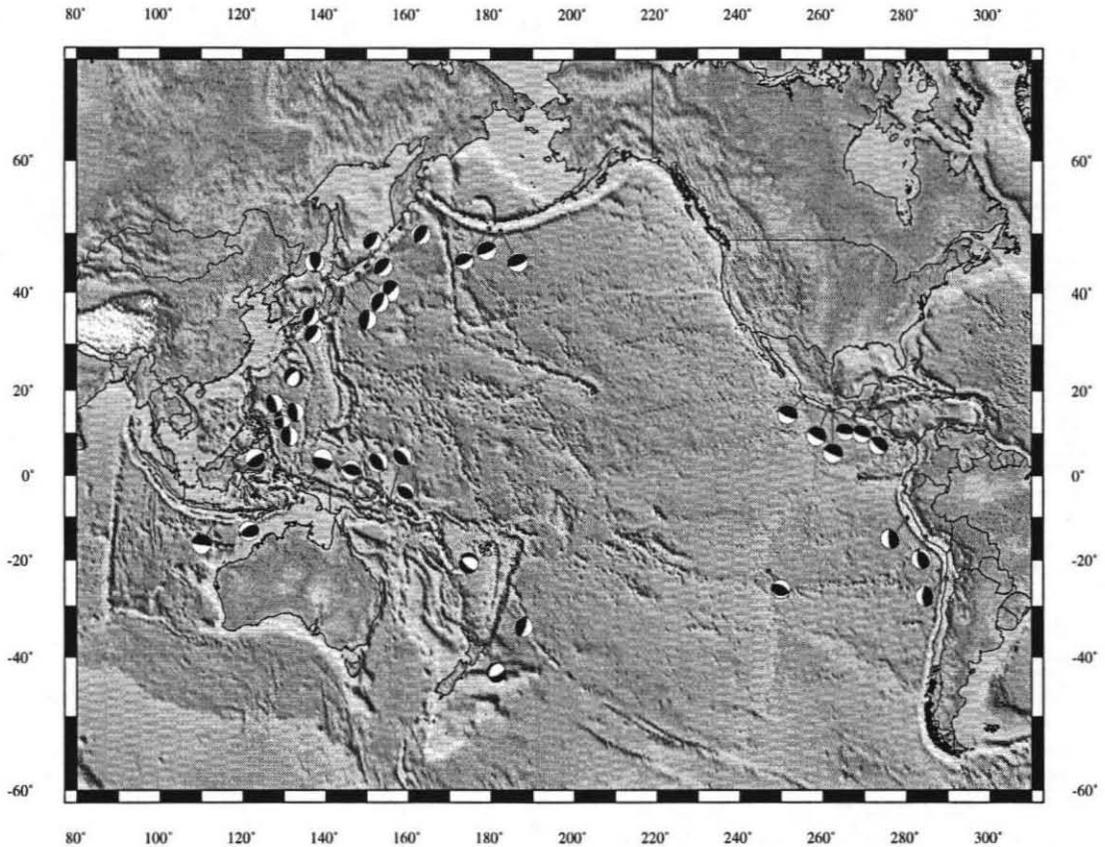
Figure 1: Earthquakes examined in this study. Focal mechanisms shown were computed using CMT inversion of very long period surface waves.

We examined the moment rate spectra for all shallow subduction zone events with moment magnitude greater than 7.0 (initially Harvard CMT moments were used in the selection process) in the time period 1992 until 1997 (Table 1 and Figure 1). Most of these earthquakes were thrust events, but we also examined several events with a normal mechanism and less shallowly dipping reverse mechanisms. We limited the time period of our investigation to after 1992, because of the limited availability of broadband data before that time, and chose to start with this year to include the 1992 Nicaragua event. In total, we examined 38 earthquakes, of which most occurred in the general region of south-east Asia.

Origin Time	NEIS Latitude	NEIS Longitude	CMT Depth	Centroid Time	CMT Moment	CMT Latitude	CMT Longitude	Strike	Dip	Slip	Event
920515070502	-5.9	147.3	36	11	8.2e+26	-6.15	147.19	275	42	77	New_Guinea
920902001600	11.7	-87.3	26	52	2.3e+27	11.34	-87.58	132	70	94	Nicaragua
921018151201	6.9	-77	20	-2	7.6e+26	6.97	-75.82	209	80	72	Colombia
921212052927	-8.2	121.9	20	21	5.2e+27	-8.43	122.38	91	41	118	Flores
930608130332	51.3	157.8	44	23	2.0e+27	50.73	158.08	37	58	96	Kamchatka
930712131715	43.2	139.4	15	19	4.9e+27	42.22	139.34	156	58	57	Sea_of_Japan
930910191254	14.6	-92.7	21	13	6.0e+26	14.02	-92.46	108	69	81	Chiapas
940602181737	-10.2	113.2	15	42	7.7e+27	-11.44	113.02	98	85	90	Java
941004132258	44.0	147.4	49	22	2.7e+28	43.20	147.50	50	73	121	Kuril_1
941009075539	43.9	148.0	37	5	6.4e+26	43.18	148.00	30	66	89	Kuril_2
941228121924	40.2	144.0	33	32	2.6e+27	40.36	143.04	9	75	89	Honshu
950205225107	-37.7	178.7	25	3	5.6e+26	-37.79	178.72	206	30	-126	New_Zealand.
950421003447	12.1	125.6	28	11	6.7e+26	12.09	126.02	1	70	98	Samar_0
950505035346	12.6	125.2	28	11	2.7e+26	12.67	125.72	352	70	97	Samar_1
950516201245	-22.9	169.7	23	15	3.6e+27	-22.73	169.67	133	60	-66	Loyalty
950703195050	-29.2	-177.7	33	11	6.3e+26	-29.30	-177.41	19	72	88	Kermadec
950730051121	-23.4	-70.1	31	32	1.2e+28	-24.02	-70.37	355	25	85	Chile
950816102728	-5.7	154.1	40	35	4.6e+27	-4.99	153.65	331	54	104	Solomon_1
950816231027	-5.7	154.1	50	25	1.0e+27	-6.22	155.46	126	31	80	Solomon_2
950914140431	16.8	-98.6	21	14	1.7e+27	16.36	-98.48	120	79	92	Guerrero_1
951009153551	18.9	-104.1	33	36	7.5e+27	18.58	-104.46	115	71	95	Jalisco
951018103726	27.9	130.3	20	7	4.3e+26	27.90	130.28	227	62	-61	Ryuku
951203180109	44.9	149.4	32	23	4.5e+27	44.43	149.81	43	64	90	Kuril_3
960101080511	0.7	119.9	21	7	2.8e+27	0.63	119.85	237	76	90	Sulawesi
960207213644	45.2	150.0	43	10	5.6e+26	44.81	150.25	32	63	79	Kuril_4
960217055933	0.5	135.8	13	26	2.5e+28	-0.70	136.18	122	8	109	Irian_Jaya
960221125104	-9.7	-79.7	22	23	1.7e+27	-10.09	-79.71	330	21	66	Peru_1
960225030816	16.0	-97.9	13	13	8.7e+26	15.35	-97.58	114	80	92	Oaxaca
960610040334	51.4	-177.8	33	23	3.6e+27	50.27	-177.59	67	70	89	Aleutians
960611182255	12.7	125.0	29	7	4.4e+26	12.76	125.42	339	70	91	Samar_2
960905081413	-22.3	-113.4	10	16	2.3e+26	-22.48	-113.14	96	35	72	Easter_0
961002094801	11.7	125.6	32	9	5.6e+25	11.94	126.26	355	70	92	Samar_3
961014232621	-7.0	155.5	33	9	1.8e+26	-7.13	155.17	126	42	95	Solomon_0
961018105024	30.6	131.1	34	4	0.9e+26	30.02	131.56	37	71	92	Kyushu_1
961019144442	31.9	131.4	30	1	1.0e+26	31.61	132.20	27	63	86	Kyushu_2
961112165943	-14.9	-75.5	43	31	3.5e+27	-14.71	-75.37	173	58	113	Peru_2
970326020857	51.3	179.6	30	11	1.1e+26	50.60	179.55	60	63	78	Rat_Islands
970719142204	15.8	-98.2	18	18	0.9e+26	15.50	-98.18	95	69	82	Guerrero_2

Table 1: Events used in this study.

As an illustration of our method, we present the results of our analysis for the June 2, 1994, event that occurred south of Java, Indonesia. As mentioned previously, this event caused hardly any damage due to ground shaking, but its tsunami height reached 14 meters and killed over 200 people. Data were available from more than 20 broadband seismic stations from the IRIS Data Center in a suitable distance range (30 to 100 degrees). The azimuthal and distance coverage as well as the data quality for this event were very good (Figure 2).
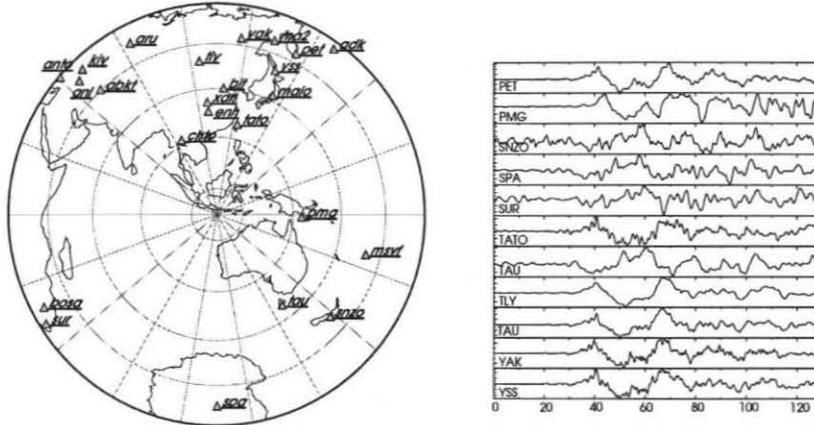
Figure 2: Event and station locations for the 1994 Java event (left).

Examples of P-wave data used for this event, aligned on predicted

IASPEI 91 travel time (right).

The source spectra for the different stations agree very well (a sample is shown in Figure 3a), and we obtained the averaged moment rate spectrum shown in Figure 3b.
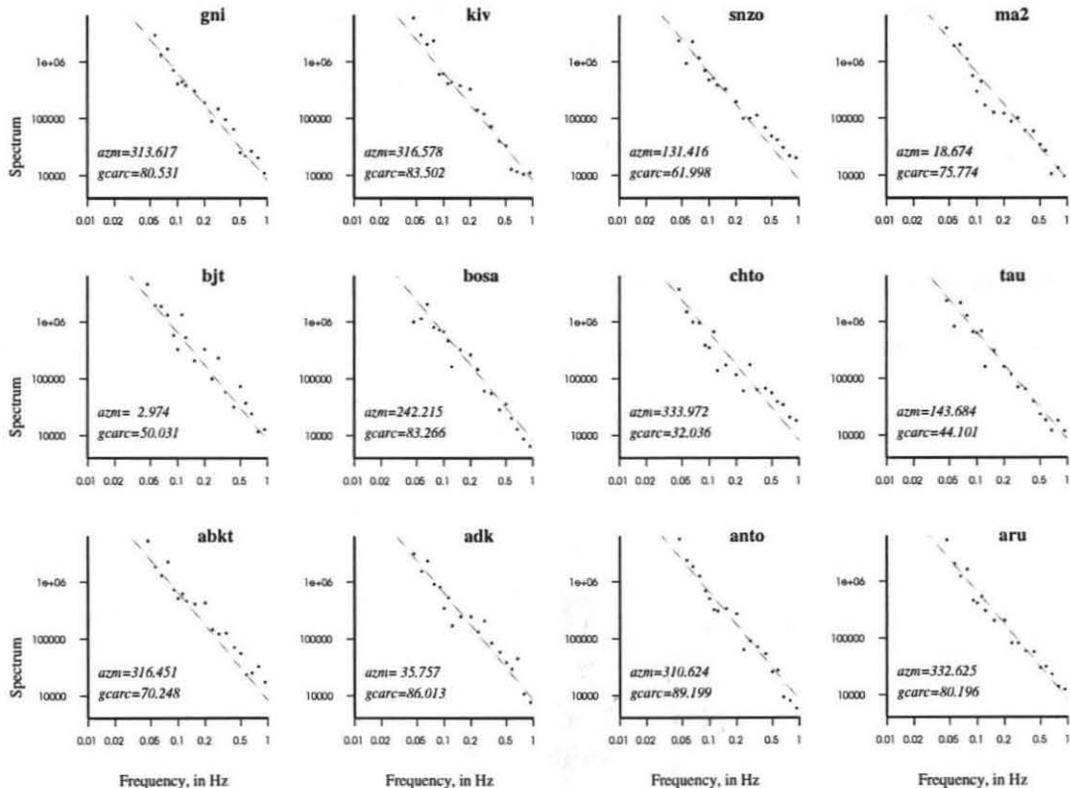
Figure 3(a): Sample of moment rate spectra determined from P-wave

recordings for the 1994 Java earthquake.
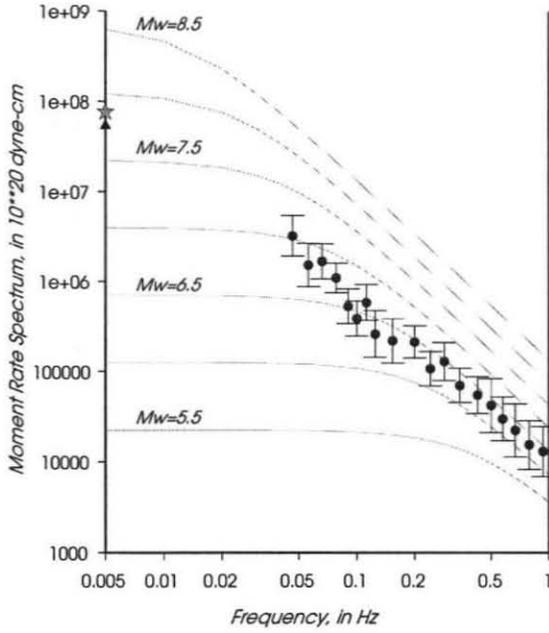
Figure 3(b): Averaged moment rate spectrum for the 1994 Java earthquake. Star indicates CMT moment determined in this study and triangle shows Harvard CMT moment. Grey reference curves are calculated for an ω^2-model with a stress drop of 30 bars and an S-wave velocity of 3.75 km/sec.

As these figures show, after the corrections described in equation [1] there are still some small variations of source spectrum with azimuth. Some of this may be due to directivity effects (especially for larger earthquakes), and in some cases there is a local station contribution. We checked all the single station spectra, and removed those which were in clear error, because of, for example, an incorrect gain or interference with another event.

For the Java event, it is clear from Figure 3(b) that the moment rate spectrum and total CMT moment are not fit well by a standard ω^2 model, as shown by the grey reference lines. In this model the moment rate function can be expressed as:

$$\hat{M}(f) = \frac{M_0 * f_0^2}{\left(f^2 + f_0^2\right)} \qquad [2]$$

Here f_0 represents the corner frequency, which can be expressed as:

$$f_0 = c \cdot \beta \cdot \left(\frac{\Delta\sigma}{M_0}\right)^{1/3} \qquad [3]$$

Here β represents the shear wave velocity near the source, taken to be 3.75 km/sec in the calculation of the reference curves, c=0.49, and $\Delta\sigma$ is the stress drop.

This "misfit" of the data to the reference model can be the result of many different factors, one obvious problem being the constants we have to choose (e.g., density and S-wave velocity near the source, as well as stress drop). Therefore, we found it to be more useful to compare moment rate spectra for different events.

Results: Source Spectral Characteristics

To facilitate direct comparison of the different events, we plot the values of the moment rate spectrum at four different frequencies as a function of the total moment as determined in the CMT inversion for all events in Figure 4. As a reference, we again plot curves computed for an ω^2 model, for different stress drops, which are shown by the numbers to the right of the corresponding grey curves.

The four earthquakes which are of particular interest, because of the anomalously high excitation of tsunamis, are the Java, Nicaragua, Flores and Peru_1 events. Of these group of earthquakes, the 1992 Flores event is the only one that does not show 'anomalous' behavior of the moment rate function, that is, this is the only earthquake which has an average release of energy for all periods as a function of its total moment. This observation is consistent with the hypothesis that the tsunami following the Flores Island event was not directly caused by the earthquake itself, but was an effect of landslides triggered by the quake (Tsuji et al., 1995; Hidayat et al., 1995). The evidence for this is in the observation of collapsed cliff faces and landslides on the island itself and its neighboring islands. The other three events in this group however, all show a low energy release at shorter periods with respect to their total moment as measured at longer periods and could be called 'slow' earthquakes. In the case of Nicaragua and Java, this is consistent for all periods; for the Peru_1 event this is less pronounced at the shorter periods, but obvious for moment release at a period of 22 sec (this may be caused by the relatively poor data for this event).
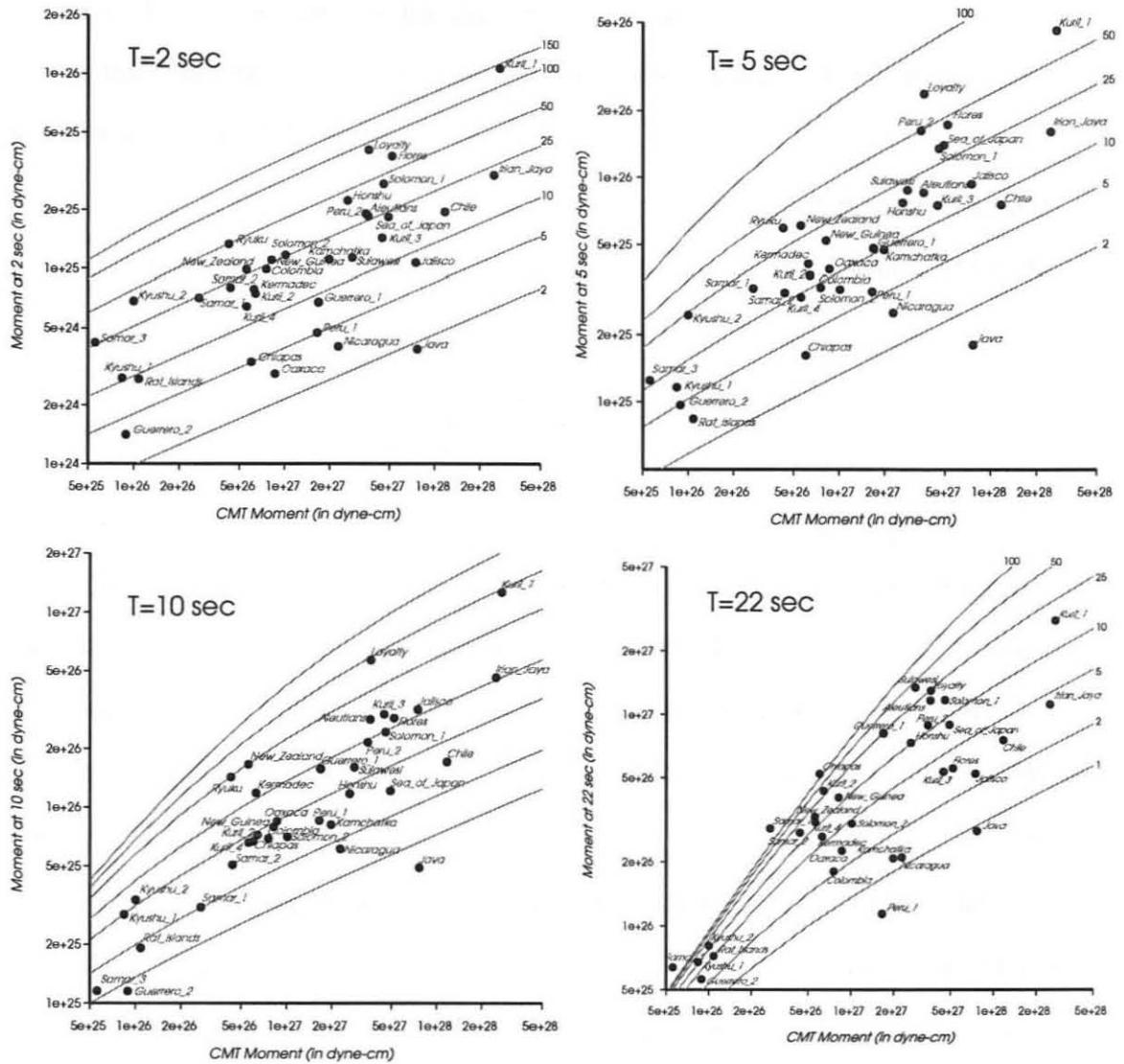
Figure 4: Moment rate values for chosen periods (2,5,10 and 22 sec) as a function of total moment as determined by CMT inversion of long period surface waves. Reference curves were calculated for an ω^2 model. Values next to the grey curves indicate stress drop used to calculate reference curve. Event names (Table 1) are given next to the corresponding moment rate values.

Also of interest is the comparison between events Peru_1 and Peru_2, two events which were located close to each other near the coast of Peru, but with clearly different frequency contents. An alternative (but essentially similar) interpretation of this figure is that this

group of three earthquakes has a low stress drop. As we can see from Figure 4, this analysis can be used as an accurate discriminant for tsunami earthquakes, and could be available within hours of an event, making it possible to release a tsunami warning in time for the teleseismic arrival of the water-waves.

Another parameter that we determined in our analysis is the value of spectral drop-off. To determine this value, we fit the determined moment rate values by a curve of the more general form of equation [2]:

$$\hat{M}(f) = \frac{M_0 * f_0^n}{(f^n + f_0^n)} \qquad [4]$$

Here n represents the spectral drop-off. In general, the value of M_0 was poorly constrained by this fit, because for most events the corner frequency was not reached within the measured frequency window, making the abscissa difficult to predict. However, the value for n was generally well-determined, and independent from the starting parameters of the fit. We have plotted the values for spectral drop-off thus obtained for all earthquakes in Table 1 in Figure 5.

The Nicaragua, Java and Peru_1 events, which were previously identified as having an anomalously low energy release at higher frequency, do not show any evidence for an anomalous value of spectral drop-off. In fact, these events are located very close to the median value for all shallow subduction zone earthquakes. This indicates that the energy release is consistently low for the examined frequency band, and there is no general difference in the source spectral shape of tsunami earthquakes versus regular earthquakes (thus, this can not be used as a discriminant). In general, the drop-off values for all examined shallow subduction zone events lie between 1.25 and 2.60, with an average value of 1.8, showing that an ω^2 approximation is fairly appropriate for most events. Another interesting observation can be made from Figure 5: it seems that there are regional trends in the spectral drop-off values, for example, the events in the central American subduction zone
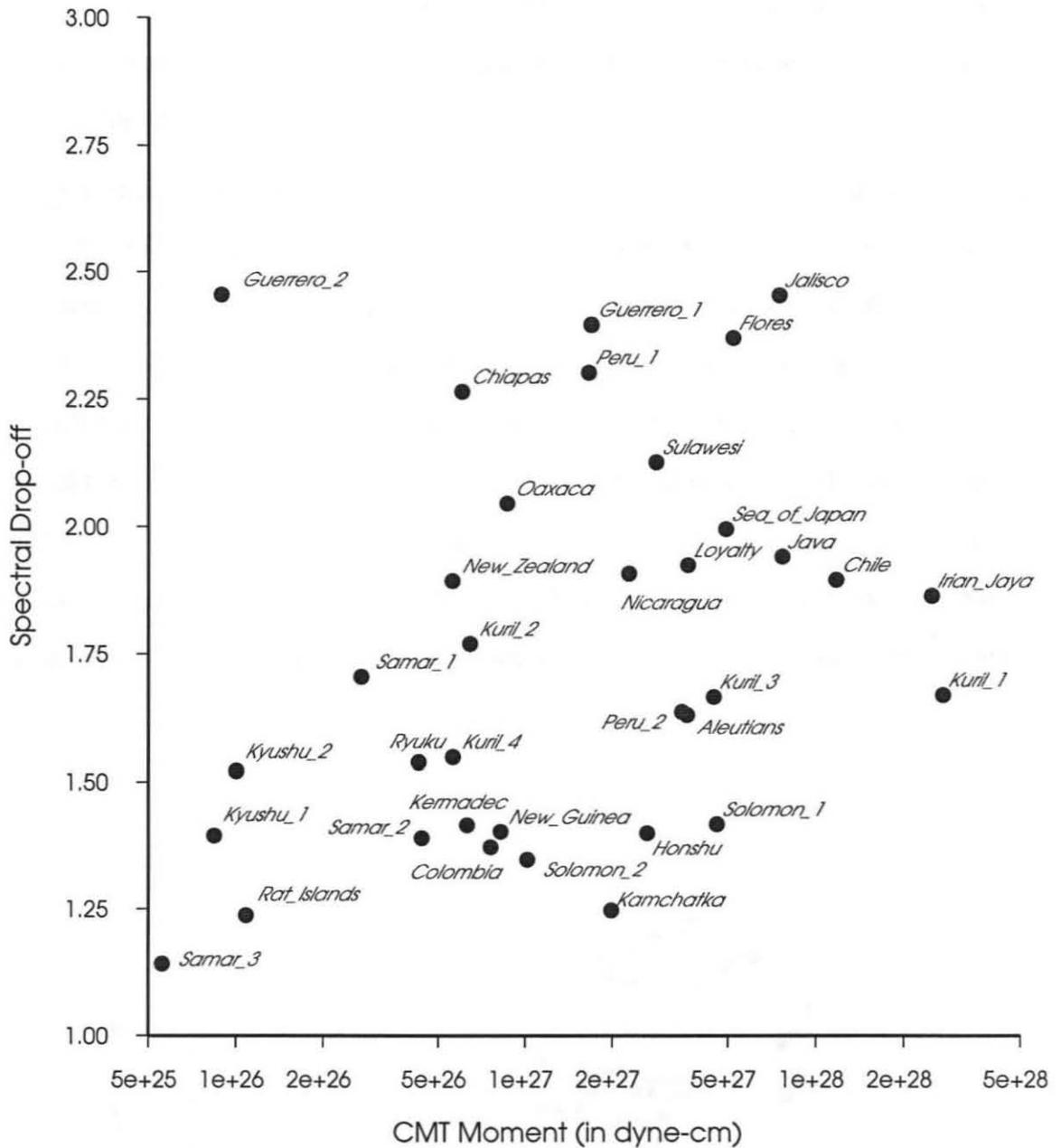
*Figure 5: Spectral drop-off values as a function of CMT total moment
determined by fitting the measured moment rate values by a function of
the form of equation [3]. Names of events as given in Table 1 are indicat-
ed next to the corresponding value.*

tend to have a relatively high drop-off, and the values for those events in the Kurils are all

close to 1.60. This could mean that there is a direct physical link between these values and

the related subduction zones. Of course, in the case of the Kuril Island events, some of the

earthquakes are actually aftershocks of the first event, so we might expect them to look similar, and more work needs to be done and more smaller events need to be examined before a final conclusion can be drawn.

Another parameter of interest in examining tsunami earthquakes is the source duration. In our CMT inversion a centroid time is determined, which gives a value comparable to half the source duration. Although the resolution of this calculation is not high for such long period surface waves, and will also be influenced by errors in origin time and location, it can still give a good indication of anomalous behavior of an event. In Figure 6, we have plotted the centroid time - origin time as a function of total moment. Although there is a large scatter of the plotted values, we can see a clear correlation of total moment with source duration, as is expected. Also obvious is the long source duration of both the Nicaragua as well as the Java event. A circa 100 sec source duration for the Nicaragua event has
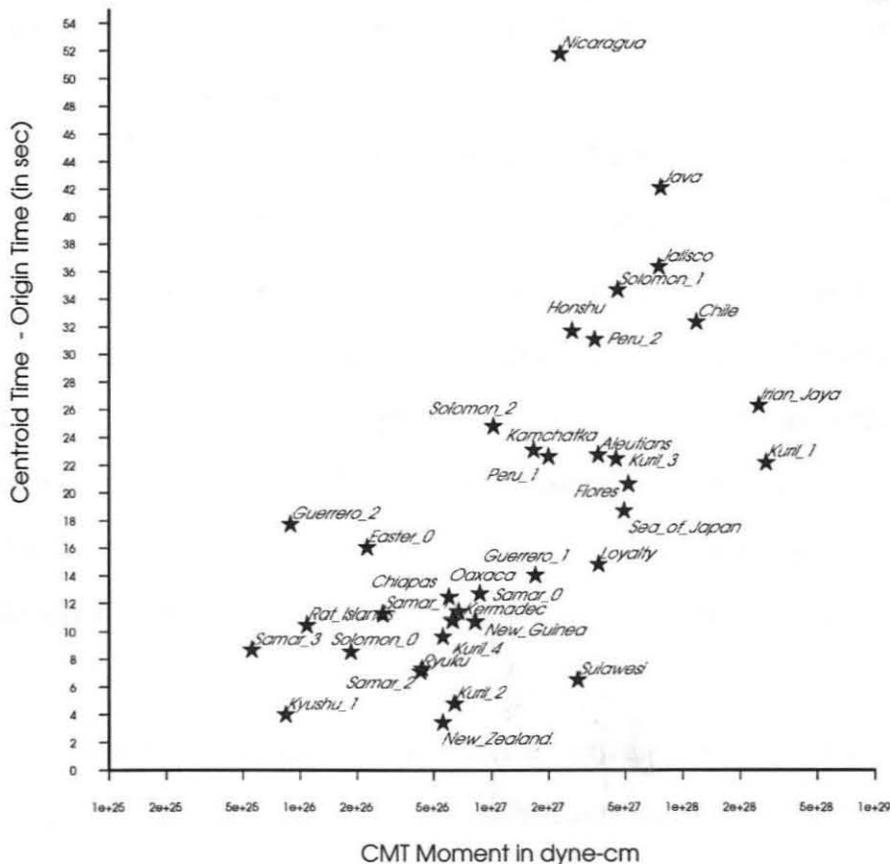
Figure 6: Centroid time as determined by long period CMT inversion - Origin time plotted as a function of CMT moment.

been found by many previous studies (e.g., Kanamori and Kikuchi,1993; Imamura et al., 1993 and Ihmle, 1996). The Peru_1 event, however, does not have an anomalously long source time function.

Future work in finding a faster discriminant for tsunami earthquakes could focus on determining an estimate of source duration using the P-wavetrain. Since tsunami earthquakes have a long source duration and low energy release in the 20 sec range, a high ratio of these two values could be used as an indicator of high tsunami generating potential of an event.

Proximity to Trench and Rupture Direction

To examine the event location and rupture direction, we plotted the centroid location from both our and Harvard's inversion (which may be more accurate because of its use of shorter period waves, and application of tomographic models for phase corrections) and the NEIS epicentral location on maps of sea floor topography. This topography was obtained using ship soundings to constrain the long wavelengths and Geosat-ERS-1 gravity anomalies to constrain the short wavelengths (Smith and Sandwell, 1997).

Figure 7 shows one of these maps for the Central American subduction zone, and includes the locations of the six earthquakes in this region that were investigated in this study. Since the NEIS epicentral location is determined using short period body waves (mostly direct P and S waves), we can interpret this location as representative of the start of the rupture. The centroid locations, measured at longer periods, show the centroid of moment release and thus the direction from NEIS location to centroid location indicated the rupture direction of the events.

All earthquakes in this region ruptured trenchward, with the centroids for Guerrero_2 and Nicaragua consistently located close to the trench. There is also some indication of the Jalisco and Oaxaca centroids being near the trench, but the two centroids do not agree here. Work by Pacheco et al. (1997), however, indicates that the Jalisco earthquake ruptured
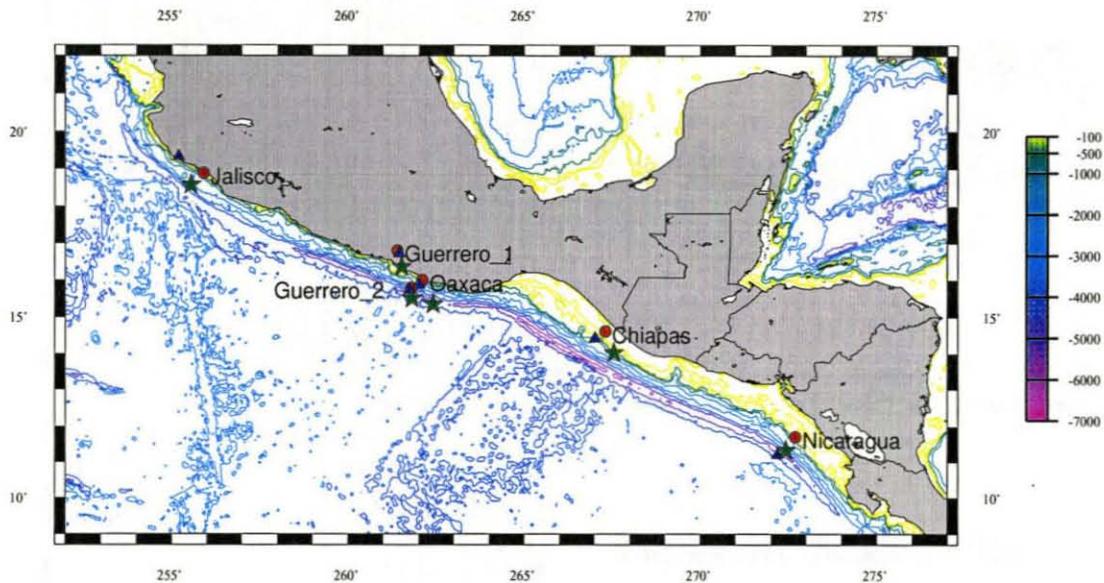
Figure 7: Map of the Central American subduction zone with contours of sea floor topography in meters from Smith and Sandwell, 1997. Red circles denote the NEIS epicenter, green stars show the centroid as determined in this study and blue triangles represent the Harvard centroid location.

unusually close to the trench. The Guerrero_2 and Nicaragua events were depleted in high frequency energy (Figure 4).

Figure 8 shows similar maps for both the South American as well as the Java trench. Again, the tsunami earthquakes both ruptured up-dip and their final centroids were located close to the trench itself. Another interesting observation is that all three tsunami events studied in this paper were located in areas where the trench is far removed from the coastline.

In general, most earthquakes in Table 1 were determined to have ruptured up-dip, or the locations were too close together to be any indication of rupture direction (for the majority). There was, however, one event that showed a clear seawards direction of rupture propagation; this was the December 28, 1994, earthquake near Honshu.
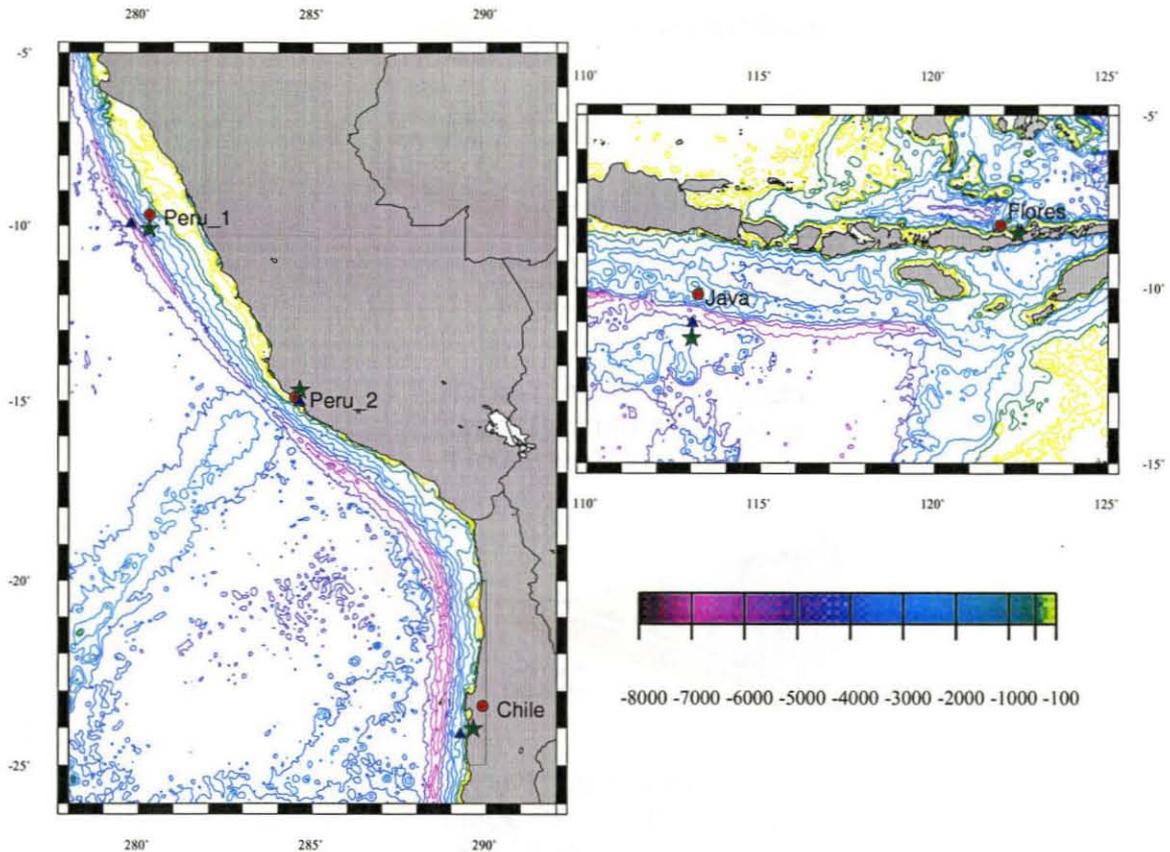
Figure 8: Contour maps of sea floor topography in meters for the South American and Java trenches. Symbols as in Figure 7.

Sediment Thickness

Because of the slow nature of the rupture of tsunami earthquakes, it has been suggested by many researchers that sediments may play an important role in the tsunamigenic potential of these events (Okal, 1988; Kanamori and Kikuchi, 1992; Ihmle, 1996; Tanioka et al., 1997). We obtained a global grid of sediment thickness for the National Geophysical data Center, to examine the relationship between tsunamigenic potential and sediment thickness more closely. However, this data-set has significant inaccuracies and errors and parts of it have been determined by extra- and interpolation, so our conclusions based on this data-set have to be tentative, until more accurate information is available. To supplement this data-base we will use more local data-sets, described in, e.g., von Huene and Scholl (1991) and

Type-2, Non-Accreting Margin
(19000 km)
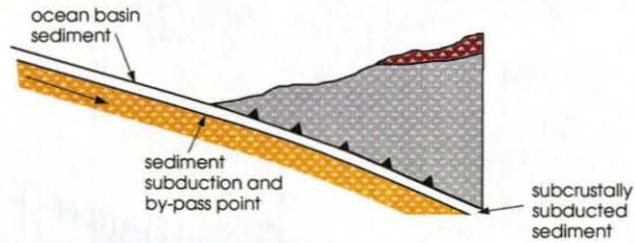
Type-1, Accreting Margin,
Small Prism (5-40 km wide)
(16000 km)
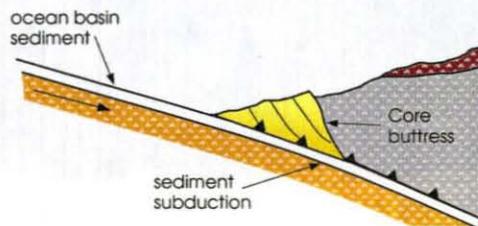
Type-1*, Accreting Margin,
Large Prism (>40 km wide)
(8000 km)
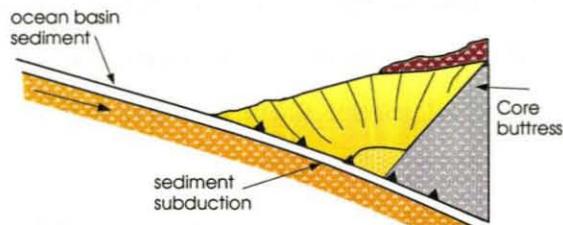
Figure 9 : Simplified diagrams of three types of continental margins

(adapted from von Huene and Scholl, 1991) : type 2 or nonaccreting

margins, type 1 margins with small to medium-sized prisms and type 1*

margins with large accretionary prisms. The approximate global lengths

of these margins is shown.

Hilde (1983).

The Nicaragua earthquake occurred near the Mid American trench, on the subduction

interface between the Cocos and North American plates. This area is located between the

Costa Rica and Guatemala trenches, which are described as type 2 margins, where the

classifications of convergent margins are according to Figure 9. From the NGDC sediment
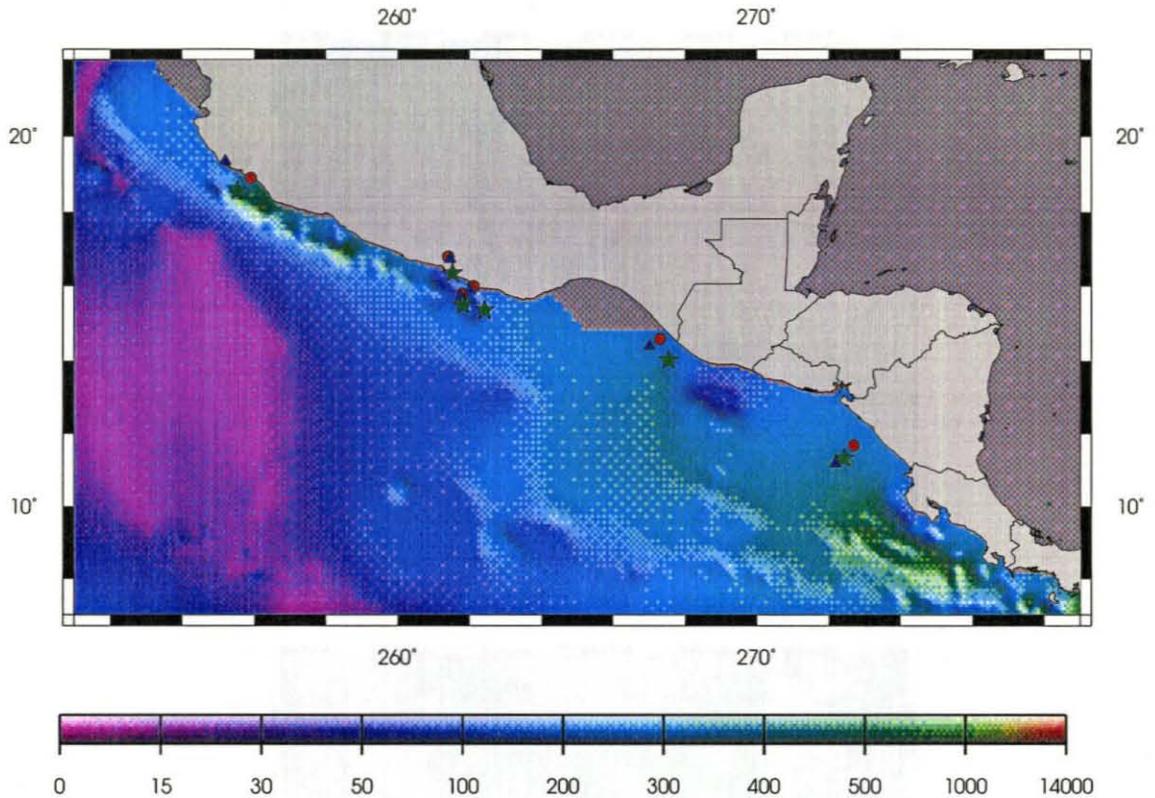
Figure 10 : Map of sediment thickness in meters from the sea floor to the

top of the acoustic basement for the middle America. Symbols are as in

Figure 7.

thickness database, it seems that, locally, there is a small size accretionary prism present

near the centroid of the Nicaragua event, between two local minima in sediment thickness

(Figure 10). The suggestion that this event occurred near a margin with only a small accre-

tionary prism (<5 km wide), and a thin sedimentary cover on the subducting oceanic crust,

is confirmed by the preliminary work of Walther and Flueh (1998), which was part of the

PACOMAR 3 project. This project conducted a ship survey along the Pacific coast of

Nicaragua in spring of 1996. The resulting geophysical dataset also shows slide scars at the

edge of the shelf, which may have formed during tsunamigenic earthquakes, and a highly

faulted oceanic crust adjacent to the trench (von Huene et al., 1998). This very strong horst

and graben structure of the oceanic plate, which even cuts up the seamounts as the crust is
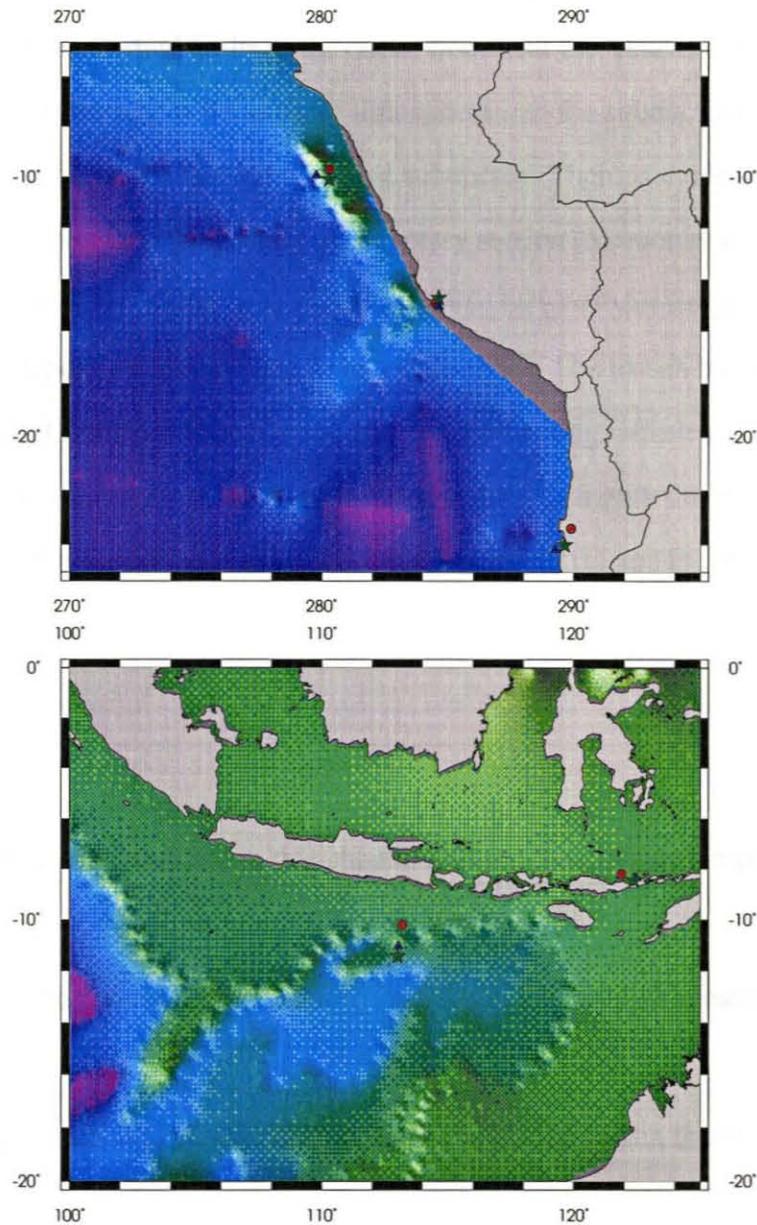
Figure 11: Sediment thickness maps for the Java and Peru events. Color bar and symbols as in Figure 10.

flexed, von Huene personal communication) allows for a lot of space for sediments to subduct (Walther, personal communication).

Both the Peru and Java continental margins near the centroid of the studied tsunami earthquakes are described as Type 1 margins by von Huene and Scholl (1991). The existence of only small accretionary prisms is confirmed by the sediment thickness maps of these

regions (Figure 11) and local studies of the area. Long range sidescan sonar swath images of the Java trench show normal faults in the ocean floor near the trench, resulting from the tension related to the bending of the oceanic lithosphere into the subduction zone (Masson et al., 1990) and areas of small seamounts being subducted. There is evidence for a small accretionary prism, and a thin subducting sedimentary section (Masson et al., 1991). Study of the Peru margin near the 1996 tsunami event showed large subducted grabens containing trench deposits (Hilde, 1983; Kulm et al., 1981). The trench has a small accretionary prism (13 km width) and a thin layer of subducting sediments (500 m) (von Huene et al., 1996). Studies to the south of this region show a highly developed horst and graben structure of the oceanic plate near the trench, possibly related to the subduction of the Nazca ridge.

Interpretation

The tsunami earthquakes described in this chapter seem to have several important factors in common:

1. Long source duration, slow rupture velocity, relatively low energy release at high frequencies.

2. Rupture propagates up-dip to very shallow depth (or possibly even the ocean floor surface).

3. The distance from the trench where the events occurred, to the coastline, is unusually large.

4. Subducting sedimentary layer, and only small size accretionary prism in trench.

5. Ocean floor near trench is highly faulted, indicative of strong horst and graben structures in the subducting slab.

In general, shallow subduction zones with a relatively young (< 100 m.a.) oceanic crust,

ocean basin
sediment

updip limit

downdip limit

Core
buttress

sediment
subduction

stable sliding of
unconsolidated sediments
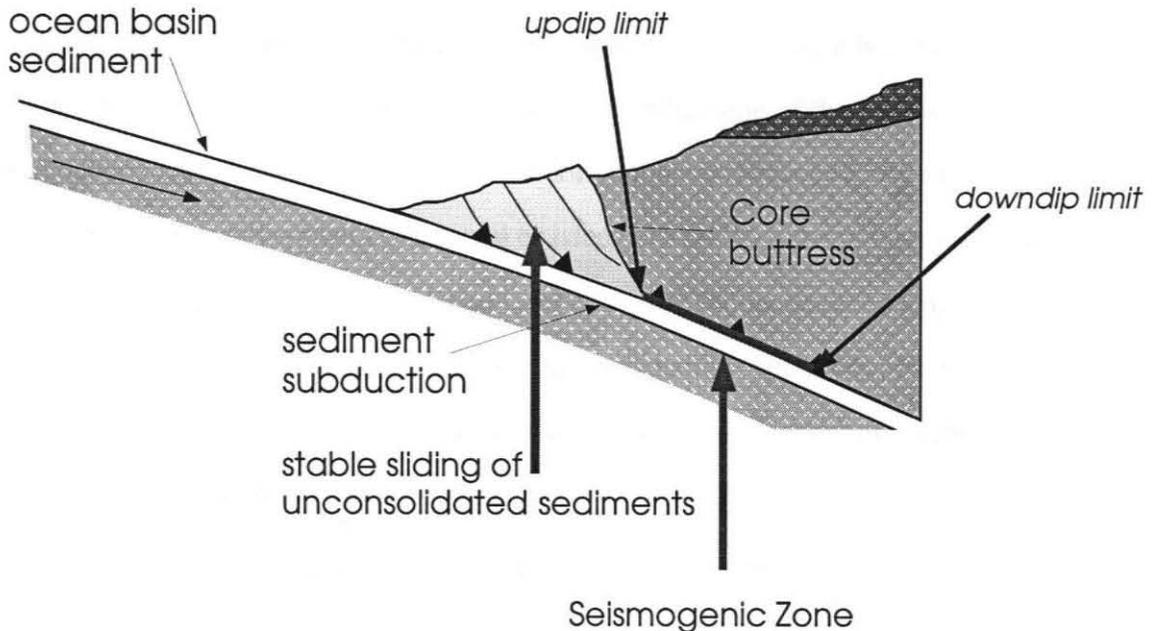
Seismogenic Zone

Figure 12: A simplified model of the seismogenic zone of subduction

thrust faults. The seaward updip part of the fault exhibits stable sliding

behaviour, as well as the part of the fault which is downdip of a critical

point.

where there exists strong coupling between the downgoing slab and the upper plate, can be

described by the following model (Figure 12). Earthquakes are only nucleated over a limit-

ed depth range, which is called the seismogenic zone, and constitutes a frictionally unstable

region. No nucleation takes place in the seaward updip portion and landward downdip of a

critical point (e.g., Byrne et al., 1988; Hyndman et al., 1997; and Scholz, 1998). No

earthquake can nucleate in the seaward shallow zone (which is commonly called

'aseismic') as a consequence of the presence of unconsolidated, granular sediments, which

form a stable-sliding (velocity strengthening) zone. In this zone, deformation is accommo-

dated in the form of creep. If earthquakes propagate into this stable region, a negative stress

drop will occur, resulting in a rapid stop to the rupture propagation. The third frictional

stability regime is the conditionally stable regime; earthquakes can propagate (indefinitely)

into such a region, provided that their dynamic stresses continue to produce a large enough

velocity jump; however, no earthquake nucleation can take place here. The subduction thrust reaches the transition from the upper stable zone to unstable behavior, which composes the updip limit of the seismogenic zone, when one of the following two conditions is met. Either the 'backstop' (or core buttress) is reached, that is, where the thrust first contacts overlying continental or island arc crust, or the temperature reaches the dehydration temperature of the smectite-illite transition for the smectite clays (100-150°C), present in most accreted sediments. Illite clays may exhibit stick-slip behavior after most free water is lost, whereas smectites will exhibit stable sliding even after most free water is expelled (Wang and Mao, 1979).

Two different factors may determine the down-dip limit of the seismogenic zone. At some depth a temperature is reached on the fault where the rocks start to behave plastically, and this critical temperature is about 300-350°C. Large earthquakes, initiated at less than this critical temperature, may still extend to about 450°C, defining an area of conditional stability, but below this depth stable sliding behavior takes over. An alternative downdip limit could be the forearc mantle, where the presence of serpentinites exhibits conditionally stable behavior (Hyndman et al., 1997).

Most earthquakes examined in this study agree with this simple model. The events nucleate in the seismogenic zone at about 20 or 30 km depth, propagate up-dip through the conditionally stable region of compacted, dehydrated sediments, but can not penetrate the stable-sliding region of the unconsolidated sediments, where a stable sliding friction regime holds. Thus, these earthquakes do not produce much shallow sea floor deformation and water displacement and do not cause great tsunamis. Since the rupture does not propagate through sediments for long periods of time, these earthquakes are not slow. This could be termed a 'regular' shallow subduction zone earthquake.

The events analyzed in this study have demonstrated that there are several exceptions to this simple model. The Jalisco earthquake, for example, ruptured close to the trench. However, this region of the middle American subduction zone seems to be depleted in

(a)

sediment

sediment
subduction

stable sliding of
unconsolidated sediments

(b)
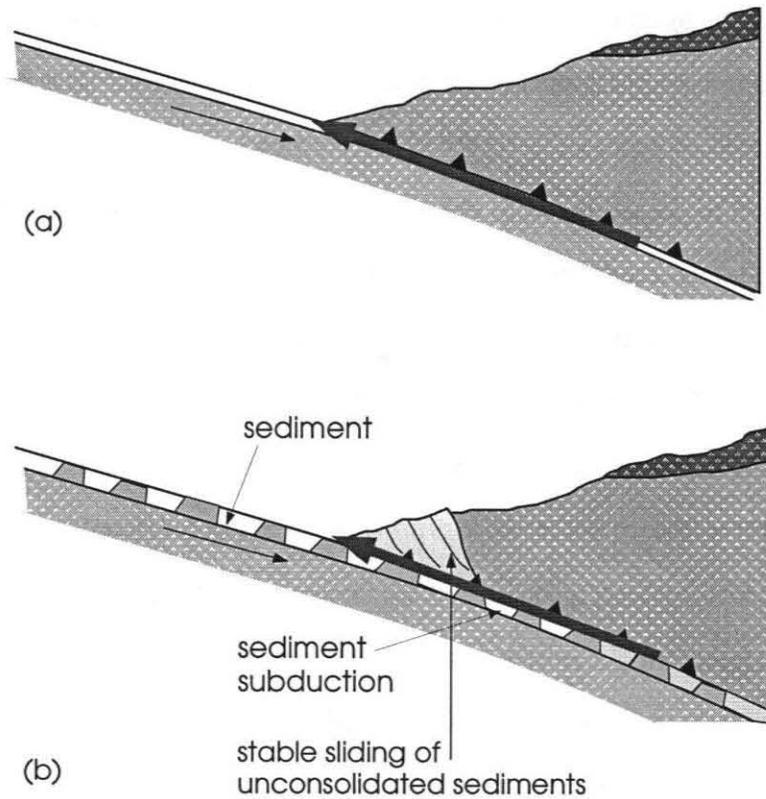
*Figure 13: Models for (a) shallow earthquakes in sediment-starved sub-
duction zones, (b) tsunami earthquakes, with rough subducting ocean
floor.*

sediments (Pacheco et al.,1997). This would make it possible for an earthquake to rupture

all the way to the ocean floor surface, unhindered by stable sliding sediments (Figure 13a).

The Nicaragua, Java and Peru earthquakes, however, also ruptured up to the trench,

although there are sediments being subducted. In these cases, an explanation may be found

in the model that Tanioka et al. (1997) proposed for the Japan trench region. In all three

regions, the ocean floor close to the trench was found to be highly faulted, suggesting that

the subducting plate is rough (exhibits a well-developed horst and graben structure). As

these structures are subducted with sediments in the graben part (but not covering the

horsts), the horsts can create enough contact with the overriding block to cause an

earthquake in the shallower part of the interface zone (Figure 13b). Since there is only a

small accretionary prism present near the trench in these regions, the earthquake can

breach the surface and generate great tsunamis. Although a large amount of slip at shallow depths at the plate interface occurred during the Nicaragua mainshock, very few aftershocks are located in this region (Ihmle, 1996). This suggests that although the rupture could propagate through this area, there is no or little nucleation of events possible in this region, similar to conditionally stable friction behavior. This may be because, in the shallowest part of the subduction zone, a thin layer of sediments still covers the top of the horsts, this would possibly support the propagation of a rupture, but will not nucleate earthquakes, and will also enhance the smoothness of the rupture. This thin layer may be scraped off and deposited in the grabens further down the trench or may quickly be compressed or dehydrated. The presence of sediments in the rupture zone also explains the slow character of these tsunami events. This is only possible in regions where the sediment transport is not so great as to cover the horsts with a thick layer of sediments, which would completely remove the contact zone with the overriding plate. Also, if the accretionary prism were large, the earthquake will not be able to break through to the surface. Of course, in case of a large accretionary prism, there would be the risk of massive slumping, which would also generate a great tsunami.

But why is the tsunami caused by the Nicaragua earthquake, for example, underestimated by its seismic moment (Imamura et al., 1993), whereas earthquakes like the event near Jalisco produce tsunamis seemingly consistent with their moment magnitude? We suggest that the displacement calculated from the seismic moment might be underestimated, because in the process of determining moment from seismic amplitudes and subsequently determining displacement from this moment, the elastic constants from the source area may not (correctly) be taken into account. Tsunami modelers may thus underestimate the tsunami caused by an event that ruptures into sediments (and is slow) because this displacement is not representative of the true earthquake displacement (Satake, 1994).

Conclusions

We have examined the source spectra of all recent large shallow subduction zone earthquakes. We found that moment rate values calculated from teleseismic P-waves for the 1992 Nicaragua and Java earthquakes, as well as the 1996 event offshore of Peru, demonstrated that these events released relatively little energy in the high frequencies with respect to their seismic moment. These three earthquakes also directly caused tsunamis greater than would be expected from their moment, and can thus be called 'tsunami earthquakes'. Other earthquakes in this dataset which were followed by great tsunamis, either did not cause them directly (the Flores Island tsunami was most likely caused by a triggered landslide), or did not cause disproportionately great tsunamis (the 1994 Kuril Island event).

Examination of the centroid location and epicenter of all these events showed that almost all events ruptured updip and that the three tsunami events ruptured close to the trench, possibly even to the ocean floor itself. Ocean floor survey results suggest that in all three regions, the ocean floor close to the trench is highly faulted, there exists only a small accretionary prism and a thin layer of sediments is being subducted.

Most examined earthquakes seem to conform to the simple model of shallow subduction thrust faulting : the rupture is initiated in the unstable friction regime, where the sediments have been dehydrated and compacted, and ruptures up-dip, where its propagation is stopped by the stable region of unconsolidated sediments. In the case of sediment starved subduction zones, it is possible for the earthquake to rupture all the way to the surface (and to be nucleated at shallower depth). In the case of tsunami earthquakes, the rough surface of the subducting ocean floor (the horsts) makes contact with the overriding plate. The thin layer of sediments is subducted in the grabens. This makes it possible for the earthquake to be nucleated at a shallow depth and propagate up to the trench. These earthquakes will propagate through sediments, making the rupture process slow. The amount of sediments

being subducted, and that being scraped off to form the accretionary prism, has to be relatively small for this model to work. If a large accretionary prism is formed, the stable sliding part of the shallow subduction zone might be too great for the earthquake to be able to break through to the surface, and in case of a thick layer of subducting sediments, the horst structures might be completely covered, so that there are no contact zones with the overriding plate.

We suggest that the relatively great tsunami excitation with respect to their moment of these tsunami earthquakes can be explained by two factors. First, because the slip occurs at shallow depth, the water displacement will be relatively great. And, second, these earthquakes may excite greater tsunamis than earthquakes with the same moment and slip distribution with depth in sediment starved trenches, because the moment as determined with a standard model for the elastic parameters does not represent and underestimates the true displacement of the ocean floor, because of the sediment rich source region of the event.

References

Boore, D.M. and J. Boatwright, Average body-wave radiation coefficients, Bull. Seismol. Soc. Am., 74, 1615-1621, 1984.

Byrne, D.E., Davis, D.M. and L.R. Sykes, Loci and maximum size of thrust earthquakes and the mechanics of the shallow region of subduction zones, Tectonics, 7, 833-857, 1988.

Hidayat, D., Barker, J.S. and K. Satake, Modeling the seismic source and tsunami generation of the December 12, 1992 Flores island, Indonesia, earthquake, Pure Appl. Geophys., 144, 537-554, 1995.

Hilde, T.W.C., Sediment subduction versus accretion around the Pacific, Tectonophys., 99, 381-397, 1983.

Houston, H. and H. Kanamori, Source spectra of great earthquakes, Bull. Seismol. Soc. Am., 76, 1, 19-42, 1986.

Hyndman, R.D., Yamano, M. and D.A. Oleskevich, The seismogenic zone of subduction thrust faults, Isl. Arc, 6, 244-260, 1997.

Ide, S., Imamura, F., Yoshida, Y. and K. Abe, Source characteristics of the Nicaraguan tsunami earthquake of September 2, 1992, Geophys. Res. Lett., 20, 863-866, 1993.

Ihmle, P. F., Frequency-dependent relocation of the 1992 Nicaragua slow earthquake, an empirical Greens-function approach, Geophys. J. Int., 127, 75-85, 1996.

Imamura, F., Shuto, N., Ide, S., Yoshida, Y. and K. Abe, Estimate of the tsunami source of the 1992 Nicaragua earthquake from tsunami data, Geophys. Res. Lett., 20, 863-866, 1993.

International Survey Team, (http://www.geophys.washington.edu/tsunami/Peru/peru.html),, 1997.

Kanamori, H., Mechanism of tsunami earthquakes, Phys. Earth Planet. Inter., 6, 346-359, 1972.

Kanamori, H. and M. Kikuchi, The 1992 Nicaragua earthquake: a slow earthquake associated with subducted sediments, Nature, 361, 714-716, 1993.

Kulm, L.D., Prince, R.A., French, W., Johnson, S. and A. Masias, Crustal structure and tectonics of the central Peru continental margin and trench. In : L.D. Kulm, J. Dymond, E.J. Dasch and D.M. Hussong (Editors), Nazca Plate : Crustal formation and Andean Convergence, Geol. Soc. Am., Mem., 154, 445-468, 1981.

Masson, D.G., Milsom, J. and A.J. Barber, Recent tectonics around the island of Timor, eastern Indonesia, Mar. and Petr. Geol., 8, 35-49, 1991.

Masson, D.G., Parson, L.M., Milsom, J., Nichols, G., Sikumbang, N. et al., Tectonophys., 185, 51-65, 1990.

Okal, E.A., Seismic parameters controlling far-field tsunami amplitudes : A review, Nat. Hazards, 1, 67-96, 1988.

Piatenesi, A., Tinti, S. and I. Gavagni, The slip distribution of the 1992 Nicaragua earthquake from tsunami run-up data, Geophys. Res. Lett., 23, 37-40, 1996.

Satake, K., Mechanism of the 1992 Nicaragua tsunami earthquake, Geophys. Res. Let., 21, 2519-2522, 1994.

Satake, K., Linear and nonlinear computations of the 1992 Nicaragua earthquake tsunami, Pure and Appl. Geophys., 144, 455-470, 1995.

Scholz, C.H., Earthquakes and friction laws, Nature, 391, 37-42, 1998.

Smith, W.H.F. and D.T. Sandwell, Global sea-floor topography from satellite altimetry and ship depth soundings, Science, 277, 1956-1962, 1997.

Synolakis et al., Damage, conditions of East Java tsunamis of 1994 analyzed, EOS, 76.26, 1995.

Tanoika, Y., Ruff, L. and K. Satake, What controls the lateral variation of large earthquake occurrence along the Japan trench, Isl. Arc, 6, 261-266, 1997.

Tsuji, Y., Matsutomi, H., Imamura, F., Takeo, M., Kawata, Y., Matsuyama, M., Takahashi, T. and P. Sunarjo Harjadi, Damage to coastal villages due to the 1992 Flores island earthquake tsunami, Pure Appl. Geophys., 144, 481-524, 1995.

von Huene, R. and D.W. Scholl, Observations at convergent margins concerning sediment subduction, subduction erosion, and the growth of continental crust, Rev. of Geophys., 29, 279-316, 1991.

von Huene, R., Pecher, I.A. and M.A. Gutscher, Development of the accretionary prism along Peru and material flux after subduction of Nazca Ridge, Tectonics, 15, 19-33, 1996.

von Huene, R., Weinrebe, W., Ranero, C., Heeren, F., Walther, C. and G. Stehr,

PACOMAR 3, (http://www.geomar.de/sci_dpmt/geodyn/d_so107_pac.html), 1998.

Walther, Ch. H. E. and E.R. Flueh, From Cocos ro Carribean plate- geophysical investigations at the Pacific coast of Nicaragua, EGS abstract volume, 287, 1998.

Appendix A:

Splitting Results for the BANJO, SEDA and

PISCO Networks

event	phase	Φ(E)	t(E)	pol. az.	Φ(T)	t(T)	pol. az.
stc1 : 82±1.5; 1.05±0.05							
3410337556	ScS	null/83±5	null/1.55±0.5	-87.2			
3611732525	SKS	80±7.5	1.15±0.20	53.259	80±5	1.15±0.20	53.053
0010659548	SKKSac	-87±15	1.85±0.45	-40.619	87±12	1.90±0.524	-46.398
0062237380	SKKSac	77±13	1.15±0.25	-49.693	85±9	1.10±0.20	-46.219
0210847299	PKS	74±9.5	1.05±0.1	-58.675	83±5	1.05±0.15	-44.077
0362251104	SKS	54±11.5	1.70±0.425	35.054	-82±18	0.90±0.55	47.583
0410145045	SKS	71±22.5	1.15±2.6	39.528	-83±16	1.00±0.575	47.247
0540519024	SKKS	83±21	1.05±0.35	-62.022	78±12	1.00±0.275	-65.489
0540527395	PKS	73±12.5	0.95±0.175	-67.935	-79±7.5	1.30±0.25	-47.856
1181630008	SKKSac				-81±20	0.70±0.475	-43.716
1750658065	PKS	87±5.5	1.15±0.175	62.310	90±3.5	1.10±0.15	65.669
1841950501	SKS	78±7	1.05±0.175	52.945	88±12	0.85±0.25	56.543
2281624268	PKS	-88±10.5	1.10±0.175	56.268	-72±10.5	1.00±0.20	63.929
2350706027	SKKSac	83±3.5	1.15±0.14	-81.455	76±7.5	0.85±0.175	-85.845
stc2 : 86±2; 0.90±0.075							
0362251104	SKS	83±22.5	1.00±1.95	46.536	85±22.5	1.00±1.675	47.357
0540519024	SKKS						-64.381
0540527395	PKS						64.267
1250353476	SKKS	-72±15	1.30±0.375	61.586	-70±13	1.30±0.35	64.267
1750658065	PKS	62±10.5	0.95±0.125	69.392	-67±4.5	0.90±0.125	65.281
1841950502	SKS						
1922146398	SKKS						77.439
2281624268	PKS						63.532
2350706027	SKKS	null	null	-85.954	null	null	85.491
st01 : 78±1.5; 0.75±0.075							
1190711304	ScS	null	null	83.116			
1190711304	S	-5±11.5	2.00±0.125	-66.133			
1300636287	ScS	null	null	88.116			
1600526307	S	-29±6.5	1.2±0.075	28.815			
1610125533	S	-30±8.5	1.15±0.05	21.571			
1690325196	SKS	89±15.5	1.45±0.325	46.944	82±9.5	1.45±0.35	39.809
2021836317	SK(K)S						
2021836317	SKKSdf (2)	-70±22.5	0.5±2.225	-31.678	-81±22.5	0.5±1.725	-33.774
2711639522	SKKS				null	null	87
2890510033	SKKSac	-67±8	0.60±0.125	-38.265	-73±5.5	0.55±0.075	-41.2
2930115163	ScS	null	null	87.0			
3002220311	SKS	79±4.5	1.05±0.15	56.643	80±3	1.05±0.15	57.945
3192018113	SKKS						-3.5
3611732525	SKS	75±6	0.90±0.1	45.461	85±8.5	0.80±0.15	52.631
0062237380	SKKS						-45.2
1181630008	SKKSac						-42.93
1750658065	PKS	85±13	0.70±0.30	72.138	79±6	0.90±0.60	65.118
1841950501	SKS	76±18.5	0.75±0.35	53.704	81±20	0.65±0.30	56.133
1922146398	SKKS				null	null	76.650
2281624268	PKS	73±8	1.80±0.525	59.387	76±7	1.65±0.60	63.353
2350706027	SKKSac	65±22.5	0.70±0.65	89.460	75±6	0.95±0.20	-85.681
1841950501	SKS	-72±10	1.50±0.25	55.172	-73±7.5	1.50±0.225	54.696
2091429122	SKS	-73±11	1.15±0.2	62.847	-73±7.5	1.15±0.175	62.898

event	phase	Φ(E)	t(E)	pol. az.	Φ(T)	t(T)	pol. az.
			st02 : 87±2.5; 0.60±0.10				
1040328269	SKS	-40±21.5	0.9±1.45		-29±3	3.65±0.2	35.067
1102335301	SKS	-81±7.5	0.6±0.05		-67±6	0.55±0.05	65.906
1190711304	ScS	null	null	87.375			
1300636287	ScS	null	null	77.246			
1560109314	SKKS	-69±22.5	4±3.975	-59.83	-69±3	4±-4.0250	-60.188
1560109314	SKKS(2)	-31±22.5	1±2.475	-69.54	-2±22.5	1.15±2.55	-60.188
1600033165	ScS	null	null	24.347			24.347
1690325196	SK(K)S	87±9	1.1±0.175	46.721	82±8.5	1.1±0.175	39.553
1810923217	PKS	66±8.5	1.15±0.25	49.843	74±7	0.85±0.25	56.531
1940235558	SKS				null	null	60.230
1941145260	SKKS	54±12.5	1.85±0.4	27.166	58±6	1.75±0.3	31.245
2021836317	SK(K)S				null	null	-33.128
2021836317	SKKS (2)				null	null	-33.128
2051755421	SKS	73±5.5	2.25±0.575	60.313	73±2	2.25±0.35	59.939
2311002518	ScS	79±4.5	1.55±0.175	60.955			
2711639522	SKKS				-70±5.5	1.45±0.4	-4.5305
3002220311	SKS	77±12	0.95±0.35	61.354	73±4	1.15±0.3	57.687
3002220311	SK(K)S (2)	81±22.5	1.8±9250	70.024	74±6	2.10±0.62	57.687
3611732525	SKS	-87±21	0.55±0.30	58.7	70±8	1.00±0.275	52.386
1750658065	PKS	82±7.5	0.80±0.225	65.208	82±4.5	0.80±0.175	64.687
1831746314	SKS	-85±18	0.75±0.25	59.772	-88±11	0.80±0.175	58.544
1922146398	SKKS				null	null	77.104
2350706027	SKKS				null	null	-85.835
			st03 : -70±11.5; 0.20±0.05				
0902240535	SKS	-83±22	0.4±0.325		-90±19.5	0.45±0.225	61.445
0902240535	SKKS						
1102335301	SKS	null	null	77.502	null	null	65.750
1190711304	ScS	-78±21.5	0.55±0.25	79.608			
1300636287	ScS	null	null	-86.606			
1600033165	ScS	-19±7	1.3±0.15	18.189			
1690325196	SK(K)S				null	null	39.359
1810923217	PKS				null	null	56.413
1940235558	SKS				null	null	60.060
2021386317	SK(K)S				null	null	-32.296
2021836317	SKKS (2)				null	null	-32.296
2051755421	SKS	-40±22.5	0.75±1.625	73.437	76±16.5	1.15±0.5	59.769
2890510033	SKKSac				null	null	-40.4
3002220311	SKS	-55±22.5	0.5±0.675	56.781	-51±22.5	0.6±0.575	57.515
3241659064	SKS				null	null	49.5
3410337556	ScS				null	null	83.7
3611732525	SKS				null	null	52.209
0062237380	SKKSac				null	null	-44.2
			st04 : 84±4; 0.55±0.05				
1300636287	ScS	null	null	88.720			
1491411517	SKKSdf				null	null	81.4
1560109314	SKKS	70±11.5	1.1±0.275	-45.488	59±5	1.4±0.25	-53.919
1690325196	SKS	-64±16	0.85±0.325	42.171	-70±22.5	0.65±0.575	39.196
1810923217	PKS	90±16	0.5±0.175	62.393	81±7	0.6±0.15	56.046
1940235558	SKS	-45±22.5	1.1±1.05	62.271	-52±22.5	0.85±0.875	60.008
2021836317	SK(K)S	-83±21.5	0.55±0.45	-31.951	-80±18.5	0.55±0.35	-31.229
2021836317	SKKS						
2051755421	SK(K)S				null	null	59.714
2311002518	ScS	73±4	1.55±0.225	55.081			
2711639522	SKKSac				null	null	83.0
2890510033	SKKS	-82±11	0.60±0.10	-36.800	-88±8.5	0.65±0.125	-39.759
2980054347	PKS						56.028
3002220311	SKS	84±12	0.55±0.10	54.027	-85±9	0.45±0.125	57.395

event	phase	Φ(E)	t(E)	pol. az.	Φ(T)	t(T)	pol. az.
3410337556	ScS	72±22.5	1.70±1.25	45.667			
3460741554	ScS	76±7	1.70±0.175	45.667			
3611732525	SKS	73±13	0.70±0.20	48.439	84±10.5	0.55±0.10	52.068
0020202163	ScS	71±5	1.10±0.20	55.064			
0731256306	ScS	84±7.5	0.85±0.10	37.626			
0782353245	SKKS						45.441
1321512231	ScS	-88±22.5	1.0±2.25	75.648			
1750658065	PKS	88±7.5	0.55±0.10	62.372	-88±9	0.50±0.10	64.657
1841950501	SKS						55.586
st05 : -87±4; 0.55±0.05							
0902240535	SKS	-89±8.5	0.6±0.15		84±5	0.7±0.125	61.063
1190711304	ScS	null	null	-69.809			
1300636287	ScS	null	null	88.396			
1600033165	ScS	null	null	6.0860			
1690325196	SKS				null	null	38.947
1810923217	PKS	72±7.5	1.65±0.325	49.602	76±4.5	1.6±0.25	56.453
1940235558	SKS	77±22.5	1.25±1.175	58.428	80±22.5	1.1±0.975	59.606
2021836317	SK(K)S				null	null	-30.890
2021836317	SKKS (2)				null	null	-30.890
2311002518	ScS	-85±4	0.85±0.15	77.119			
2741635228	SK(K)S	-86±22	0.80±1.25	65.596	72±7	1.75±0.5	58.617
2930115163	ScS	null	null	79.243			
2980054347	PKS	78±13.5	0.95±0.225	42.026	90±9	0.85±0.225	56.432
3002220311	SKS	-82±12.5	0.55±0.075	61.151	89±6	0.6±0.1	57.124
3192018113	SKKS	-80±22.5	1.20±0.875	-6.334	-82±7	1.30±0.45	-8.513
0731256306	ScS	-75±9	0.85±0.1	57.446			
1130508033	SKKS	88±22.5	1.10±1.225	59.554	-89±16	1.05±0.475	60.728
1321512231	ScS	-74±10.5	0.85±0.25	89.800			
1362012457	SKS				76±13	1.50±0.575	55.043
1750658065	PKS	85±11	0.90±0.20	60.391	88±6.5	0.85±0.175	64.047
1801224039	SKS	87±22.5	0.65±0.625	59.522	84±9.5	0.70±0.20	57.918
1841950501	SKS	74±22.5	1.10±1.725	53.945	77±22.5	1.00±0.925	55.349
st06 : -63±3.5; 0.65±0.075							
0902240535	SKS	-54±12.5	0.8±0.15		-66±11.5	0.7±0.15	60.881
0902240535	SKKS	-60±17	1±0.3		-55±9	1.05±0.325	60.881
1190711394	ScS	-84±6	1.5±0.275	77.255			
1240637379	SKS				null	null	59.335
1300636287	ScS	-68±19	0.45±0.175	86.772			
1560109314	SKKS	50±22.5	1.8±1.175	-52.900	49±3	1.9±0.35	-54.143
1600033165	ScS	-28±21	0.45±0.35	12.908			
1690325196	SKS	-69±22.5	0.55±2.25	38.249	-67±22.5	0.6±2.275	38.793
1810923217	PKS	65±7	1.85±2.175	55.903	65±2.5	1.85±0.375	56.789
1940235558	SKS				null	null	59.325
2021836317	SK(K)S				null	null	-30.801
2021836317	SKKS				null	null	-30.801
2051755421	SKS	-65±19.5	1.35±1.35	61.466	-67±15	1.35±0.425	59.034
2311002518	ScS	-86±6	1.25±0.15	62.021			
2331556018	PKS	-58±22.5	0.8±1.5	11.252	-69±4.5	0.95±0.15	-3.414
2820755381	SKKS				null	null	-41.540
2890510033	SKKS	77±22.5	0.75±2.375	-38.471	76±20.5	0.75±0.375	-39.734
2930115163	ScS	73±4	2.15±0.175				
3002220311	SKS	-52±9	0.70±0.125	66.031	-77±9.5	0.55±0.075	56.946
3410337556	ScS	null	null	76.788			
3460741554	ScS	-61±13	1.15±0.20	69.651			
3611732525	SKS	-61±10.5	0.70±0.175	57.308	-73±10	0.60±0.125	51.668
0020202163	ScS	-86±6	1.30±0.15	65.874			

event	phase	Φ(E)	t(E)	pol. az.	Φ(T)	t(T)	pol. az.
				st07			
0902240535	SKS	-52±22.5	0.7±0.875		-60±18	0.6±0.25	
1471303556	SKKS				-71±16	1.05±0.40	-27.002
1750658065	PKS				null	null	63.006
1841950501	SKS				null	null	54.965
				st08 : -78±1; 1.00±0.075			
0902240535	SKS	-77±9	1±0.175		-83±7.5	1.05±0.15	60.548
0902240535	SKKS	-68±16	0.95±1.55		-78±15	0.95±0.375	60.548
0960703277	SKS-	-44±22.5	2.75±3.05		-63±4	2.85±0.275	63.948
1062309338	SKS	48±22.5	2.55±3.25		46±22.5	2.5±3.225	53.280
1102335301	SKS	-88±14	1.4±.0.375		-89±4.5	1.5±0.25	64.875
1190711304	ScS	null	null	78.058			
1300636287	ScS	-19±19	0.65±0.25	-79.052			
1440400463	SKKSac	-74±22.5	1.30±	-55.770	-73±10.5	1.35±0.425	-54.611
1600033165	ScS	4±5	3.8±0.375	23.017			
1810923217	PKS	-55±12.5	1.3±0.325	68.506	-63±7	1.15±0.25	56.805
1940235558	SKS	-69±14	1.0±0.32	65.296	-85±12.5	1.05±0.225	58.925
2052157301	SKS	-73±16	1.8±0.2	-15.310	-65±3.5	1.75±0.2	-3.1749
2051755421	SKS	-67±19.5	0.95±0.375	65.466	-80±17	0.95±0.3	58.634
2080955557	SKS-	-77±15.5	1.75±0.175	-42.961	80±7.5	4.00±3.075	49.386
2311002518	ScS	-86±8.5	1.05±0.175	59.056			
2711639522	SKKSac	-73±22.5	0.95±0.7	-5.1336	-78±7.5	1.05±-0.275	-10.813
3410337556	ScS	-55±7.5	0.55±0.05	74.349			
3460741554	ScS	-86±16.5	1.25±0.3	64.268			
3611732525	SKS	-82±14.5	1.00±0.20	48.927	-78±11.5	1.05±0.25	51.330
0362251104	SKS	-68±22.5	1.00±1.275	47.420	-75±22.5	0.85±1.275	45.896
0782353145	SKKS				77±22.5	0.40±2.225	42.269
0981745181	SKKS				null	null	-79.422
1100845105	SKKS				72±19	1.20±0.70	43.697
1250353476	SKKS	-78±13.5	1.10±0.20	58.578	-78±7	1.10±0.175	58.461
1321512231	ScS	-72±19.5	1.00±0.25	69.170			
				st09 : -79±3; 1.05±0.075			
1190711304	ScS	null	null	-71.238			
1300636287	ScS	null	null	-80.860			
1491411517	SKKSac	null	null	-88.937	null	null	82.462
1550057535	SKS	-82±22.5	1.2±1.975	-23.68	-50±17.5	1±0.45	-3.8329
1690325196	SKS	-65±22.5	1.1±1.7	48.727	88±18	0.70±0.325	38.241
1710944467	SKS	64±22.5	1.8±1.625	31.351	-86±18.5	1.35±0.625	55.412
1810923217	PKS	-46±12.5	0.85±0.2	70.797	-63±13.5	0.65±0.2	56.9
1940235558	SKS	-67±20.5	1.2±0.475	66.934	-81±16	1.2±0.475	58.683
1941145260	SKKS	null	null	16.244	null	null	26.218
2021836317	SKKS	80±22.5	1.85±2.9	-21.758	74±6	2.5±0.775	-28.998
2051755421	SKS	-81±20	1.1±0.35	69.505	87±8	1.3±0.3	58.391
2741635228	SKS	-46±17	1.55±0.225	79.111	-74±7.5	1.3±0.2	57.696
2812144092	SKKS				-71±22.5	1.35±1.025	32.895
3002220311	SKS	-55±7.5	1.25±0.15	66.078	-67±5.5	1.1±0.125	56.415
3002220311	SK(K)S (2)	-67±22.5	0.65±1.425	61.724	-83±17.5	0.65±0.25	56.415
3611732525	SKS	-69±6.5	1.45±0.15	54.51	-72±3.5	1.40±0.125	51.149
0062237380	SKKS	-66±11.5	2.30±0.45	-38.347	-70±8	2.20±0.45	-41.928
0140649238	SKS	-74±15	1.15±0.225	60.659	-79±8.5	1.15±0.225	55.501
0362251104	SKS	-64±11	1.70±0.425	51.965	-77±10	1.35±0.25	45.720
0410145045	SKS	-64±5	1.35±0.15	53.365	-83±11.5	1.05±0.225	45.377
0540519024	SKKS				-73±12	1.55±0.475	-48.372
0542103021	SKS	-48±10.5	1.00±0.2	66.679	-67±10.5	0.70±0.175	58.045
0972206580	SKS	-58±16.5	1.20±0.325	72.631	-65±12	1.15±0.275	69.120
0981745181	SKKS				81±5	1.75±0.325	-79.388
1250353476	SKKS	-67±9.5	1.30±0.25	55.679	-66±6.5	1.30±0.225	57.333
1750658065	PKS	-64±12	0.90±0.225	63.243	-64±9	0.90±0.20	62.827
1801224039	SKS	-69±13.5	1.30±0.20	61.286	-73±6.5	1.30±0.175	57.028
1841950501	SKS	-72±10	1.50±0.25	55.172	-73±7.5	1.50±0.225	54.696

event	phase	Φ(E)	t(E)	pol. az.	Φ(T)	t(T)	pol. az.
2091429122	SKS	-73±11	1.15±0.2	62.847	-73±7.5	1.15±0.175	62.898
st10 : -71±4; 0.85±0.075							
1102335301	SKS				null	null	64.403
1190711304	ScS	null	null	-86.469			
1491411517	SKKSac				null	null	83
1560109314	SKKS				null	null	-48.197
1810923217	PKS				null	null	57.316
1940235558	SKS	-82±20.5	0.95±0.475	64.351	85±16	1.2±0.5	58.259
2021836317	SKKS	74±22.5	3.95±3.95	-26.358	73±4/null	4.0±1.075/null	-28.718
2051755421	SKS	80±17.5	1.7±0.5	56.178	81±4	1.7±0.275	57.970
2051755421	SKKS(2)	-75±9	1.5±0.25	78.191	-89±5	1.7±0.275	57.790
2311002518	ScS	-75±10	1.0±0.15	73.782			
2421942482	SKKSac				null	null	18.114
2711639522	SKKSac				null	null	-12.7
3002220311	SKS	-78±6.5	0.90±0.125	53.993	-75±4.5	0.90±0.125	56.163
3002220311	SK(K)S (2)	-51±11	1.10±0.20	75.223	-72±15	1.00±0.375	56.163
3611732525	SKS	-67±5.5	0.90±0.1	54.876	-72±3.5	0.85±0.075	50.901
0010659548	SKKSac	76±12	1.30±0.275	-44.705	79±11.5	1.25±0.325	-42.364
0062237380	SKKSac	74±10	1.55±0.25	-50.477	-89±11	1.40±0.30	-41.910
0362251104	SKS				-82±22.5	0.65±1.125	45.491
0410145045	SKS				-75±20.5	1.05±0.525	45.148
0440011477	SKS				-76±17	1.00±0.375	45.543
0542103021	SKS				-54±22.5	0.65±0.75	58.042
0782353145	SKS				null	null	40.893
0972206580	SKS	-84±8.5	1.10±0.125	58.788	-59±11.5	1.10±0.25	68.864
1110009562	SKKSac	-53±9	1.95±0.425	61.029	-64±10	1.50±0.45	53.377
1471303556	SKKS				null	null	-26.048
2091429122	SKS	-56±11.5	1.10±0.25	61.436	-54±5.5	1.15±0.20	62.643
st11 : -75±4; 0.70±0.075							
1190711304	ScS	null	null	-86.469			
1300636287	ScS	null	null	-73.789			
1550057535	SKKS	45±22.5	2.5±3.225	-31.198	60±11	2.85±3.4	-5.5373
1560109314	SKKS	-80±10.5	1.8±0.65	-66.433	-69±3.5	2.1±0.325	-47.989
3002220311	SKS	-63±20	1.15±0.30	57.998	-66±10.5	1.1±0.20	55.859
1250353476	SKKS	-65±12	1.15±0.325	51.069	-64±7.5	1.15±0.30	51.861
1471303556	SKKS						-25.897
1750658065	PKS	-61±22.5	0.80±0.825	62.400	-61±16.5	0.80±0.275	61.502
1841950501	SKS	-62±19	0.80±0.35	55.451	-65±17	0.75±0.25	54.214
1922146398	SKKS						79.492
2080551180	PKS	-70±5	1.10±0.325	-61.051	-64±2	1.30±0.20	-51.592
2091429122	SKS	-60±22	0.95±0.425	60.652	-57±10.5	1.00±0.325	62.389
st12 : 85±4.0; 0.85±0.075							
1190711304	ScS	null	null	-75.987			
1600526307	ScS(2)	-84±8.5	1.15±0.1	-24.432			
1810923217	PKS	-18±22.5	0.95±0.95	-75.683	-86±13	0.7±0.2	58.226
1821012413	SKS	-75±22.5	2.8±3.1	75549	86±10.5	3.45±0.85	54.649
2021836317	SKKS	65±6	3.60±1.25	-8.12	75±4.5	1.2±0.3	-28.095
2311002518	ScS	-59±17.5	1.1±0.2	89.057			
3002220311	SKS				-72±10	1.00±0.20	55.503
3002220311	SK(K)S (2)	-51±22.5	0.80±2.375	82.181	-89±12	1.05±0.5	55.503
3611732525	SKS	-73±14	0.95±0.225	51.706	-74±9	0.95±0.2	50.339
0062237380	SKKS						
1721528515	SKS				null	null	17.080
1750658065	PKS	-71±11.5	0.75±0.125	67.226	-78±7	0.75±0.125	60.640
1841950501	SKS	-64±19.5	1.00±0.50	52.490	-61±15.5	1.05±0.425	53.906
1922146398	SKKS				null	null	81.086
2080551180	PKS	-82±7	0.80±0.10	-40.481	87±6.5	0.80±0.125	-51.768
2091429122	SKS	-70±11	0.90±0.20	53.276	-56±12.5	1.10±0.475	62.062
st13 : 82±1.5; 0.80±0.05							
0362251104	SKS	49±21.5	2.50±0.95	37.145	60±15	1.35±0.625	44.715

event	phase	Φ(E)	t(E)	pol. az.	Φ(T)	t(T)	pol. az.
0410145045	SKS	-60±9.5	1.55±0.425	45.459	-62±7	1.40±0.375	44.370
0731256306	ScS	88±11.5	0.70±0.175	51.095			
0782353145	SKKS						28.0
0972206580	SKS	76±22.5	1.30±1.10	59.760	-68±18.5	0.60±45	68.125
0981745181	SKKS	74±22.5	0.70±0.90	-84.735	78±7	0.75±0.225	-79.944
1110009562	SKKS						47.5
1260159076	SKKS						71.0
1841950501	SKS	73±15.5	1.10±0.375	49.971	88±17	0.80±0.325	53.679
1922146398	SKKS						78.7
2091429122	SKS	-89±22.5	0.75±1.15	54.529	-54±18.5	0.95±0.525	61.877
2350706027	SKKS	72±22.5	0.60±0.575	88.637	81±22.5	0.95±0.675	-86.704
2360155346	SKKS				null	null	-86.612
2410725486	SKS				null	null	-12.962
st14 : 81±1.5; 1.40±0.05							
3611732525	SKS	85±11	1.20±0.175	53.166	81±4.5	1.25±0.175	49.317
0362251104	SKS	64±21	1.65±0.85	39.779	85±13.5	1.20±0.375	43.950
0410145045	SKS	68±10	1.45±0.275	38.995	84±10.5	1.20±0.225	43.602
0440011477	SKS	-62±19.5	1.55±0.35	58.291	-88±9	1.20±0.225	43.992
0440843398	SKKSac						22.0
0542103021	SKS						57.3
0701521107	SKKS						-37.1
0731256306	ScS	84±6.5	1.45±0.125	56.456			
0782353145	SKKSac	88±20.5	1.35±0.50	33.727	-89±16	1.40±0.45	35.159
1260159076	SKKSac				null	null	71.337
1750658065	PKS				76±5.5	1.40±0.475	59.379
1721528515	SKS	80±15	1.40±0.35	21.563	74±8.5	1.30±0.275	16.092
1801224039	SKS	66±22.5	1.90±2.475	34.136	84±12	1.55±0.45	54.596
1841950501	SKS	-89±16	1.20±0.30	56.417	83±6.5	1.35±0.225	52.920
1922146398	SKKSac				null	null	78.627

Table of measured single event splitting parameters for the BANJO
array. Result of stack is given after station name. Entries for which only
event and phase information are given were used in stack, but did not
produce consistent splitting measurements. Φ(E) and t(E) are results
using the method which maximizes the linearity of the signal, Φ(T) and
t(T) were obtained by minimizing the energy on the transverse
component.

event	phase	Φ(E)	t(E)	pol. az.	Φ(T)	t(T)	pol. az.
chit : -5±11; 0.80±0.20							
1190711394	ScS	null	null	85			
1491411517	SKKS	null	null	71	null	null	85
1560109314	SKKS	-45±22.5	1.68±1.78	-65	-38±22.5	1.36±1.30	-60
1690325196	SKS	null	null	60	null	null	39
1810923217	PKS	null	null	68	null	null	57
2021836317	SKKS(1)	-2±12	0.92±0.22	-35	1±8.5	0.92±0.18	-33
2021836317	SKKS(2)	-4±10.5	1.36±0.28	-34	-2±6.5	1.32±0.22	-33
2311002518	ScS	90±4.5	2.84±0.22	-74			
3002220311	SKS	null	nul	68			
3611732525	SKS	null	null	70	null	null	52
0062237380	SKKSac	11±2.52	1.08±2.30	-37	-18±22	1.48±1.56	-45
0362251104	SKS						47
0540519024	SKKS	null	null	-68	null	null	-61
0540527395	PKS	null	null	-68	null	null	-47
0542103021	SKS	null	null	54	null	null	58
chuq : -60±5; 1.15±0.14							
1102335301	SKS	-62±15.5	1.08±0.20	71	-68±8.5	1.04±0.20	66
1190711394	ScS	null	null	-72			
1300636287	ScS	null	null	87			
1810923217	PKS	-55±5	0.92±0.20	47	-50±3.5	1.00±0.14	55
1940235558	SKS	-54±22.5	1.40±1.56	61	-54±17	1.40±0.58	61
1941145260	SKKS	null	null	29	null	null	32
2021836317	SKKS(1)	null	null	-46	null	null	-32
2021836317	SKKS(2)	null	null	-25	null	null	-32
2051755421	SKS	-64±22.5	1.04±1.12	60	-64±13.5	1.04±0.30	61
3002220311	SKS	-74±10	0.92±0.16	55	-70±8	0.92±0.16	58
3611732525	SKS	-62±9.5	1.24±0.28	54	-64±6.5	1.2±0.22	53
0062237380	SKKS	null	null	-34	null	null	-43
0210847299	PKS	-57±22.5	2.32±3.18	82	-82±11.5	0.88±0.22	-42
0540527395	PKS	null	null	-48	null	null	-44
0542103021	SKKS				null	null	58
coll : -60±5; 1.00±0.08							
1102335301	SKS	-57±17.5	1.36±0.42	56	-49±6	1.52±0.28	67
1240637379	SKS	-80±21.5	1.08±0.28	42	-58±6.5	1.44±0.24	62
1491411517	SKKS	-24±16	1.44±0.34	88	-50±18	0.84±0.38	75
1560109314	SKKS	null	null	-56	null	null	-51
1690325196	SKS	-81±22.5	1.28±1.14	36	-77±10.5	1.36±0.36	40
1810923217	PKS	-46±7.5	1.28±0.20	66	-53±4.5	1.20±0.26	54
1940235558	SKS	-74±22.5	1.16±1.48	66	-82±12.5	1.24±0.32	62
2021836317	SKKS	-55±21.5	0.64±0.26	-34	-50±10	0.76±0.26	-31
2051755421	SKS	-49±22.5	0.96±1.02	69	-67±10.5	0.76±0.14	61
2311002518	ScS	-17±11.5	0.64±0.12	-75			
lajo : -76±5; 0.48±0.10							
1300636287	ScS	null	null	83			
1560109314	SKKS				null	null	-51
1810923217	PKS	-81±9	0.36±0.12	21	-55±4.5	3.36±3.66	55
1940235558	SKS	-75±22.5	0.65±1.55	64	-88±22.5	0.75±1.025	61
1941145260	SKKS	64±16	1.25±0.20	27	70±8	1.20±0.20	32
2021836317	SKKS	89±22.5	0.40±0.575	-28	77±22.5	0.60±0.55	-31
2051755421	SKS	84±21.5	0.95±0.325	58	87±18	0.90±0.35	61
2311002518	ScS	88±4	1.40±0.125	63			
0540527395	PKS	-76±22.5	0.72±0.82	-46	-71±16	0.80±0.36	-44
poop :63±7; 1.25±0.34							
1300636287	ScS	null	null	79			
1690325196	SKS	-43±22.5	1.20±1.28	75	68±16.5	1.16±2.56	39
1810923217	PKS	null	null	64	null	null	55
2021836317	SKKS	null	null	-26	null	null	-31
2051755421	SKS	76±10	1.48±0.24	48	86±8.5	1.32±0.32	60

event	phase	Φ(E)	t(E)	pol. az.	Φ(T)	t(T)	pol. az.
chit : -5±11; 0.80±0.20							
2311002518	ScS	82±7	1.88±0.24	63			
3002220311	SKS	79±4	1.16±0.16	59	78±3	1.20±0.16	58
3611732525	SKS	68±19.5	0.96±0.38	51	70±15.5	0.88±0.40	52
0020202163	ScS	-84±8	1.12±0.30	82			
0540527395	PKS	44±6.5	2.44±0.32	-66	null	null	-45
0062237380	SKKS	null	null	-53	null	null	-43
sica : -58±4; 0.80±0.16							
1190711394	ScS	-83±10.5	1.04±0.34	80			
1300636287	ScS	null	null	78			
1491411517	SKKS				null	null	76
1810923217	PKS	-50±4	1.00±2.34	49	-47±1.5	1.08±0.16	54
2021836317	SKKS	null	null	-29	null	null	-31
2311002518	ScS	-78±7	0.80±0.14	80			
3002220311	SKS	-75±10	0.72±0.14	47	-67±	0.76	58
3410337556	ScS	-86±10.5	1.44±0.48	83			
3611732525	SKS	-65±16	0.88±0.32	51	-63±11	0.92±0.32	53
0020202163	ScS	82±12.5	0.80±0.12	32.150			
0062237380	SKKS	null	null	-42	null	null	-42
0362251104	SKS	null	null	43	null	null	47
uyun : 25±10; 0.72±0.12							
3002220311	SKS	23±12	0.64±0.12	68	6±10.5	0.68±0.14	57
3611732525	SKS	12±7	0.76±0.10	62	-4±6	0.88±0.16	52
0062237380	SKKS	null	null	-42	null	null	-45

Table of measured single event splitting parameters for the SEDA array.

event	phase	$\Phi(E)$	t(E)	pol. az.	$\Phi(T)$	t(T)	pol. az.
PUJI : -61±15; 0.50±0.40							
0902240535	SKS	-51±22.5	0.55±2.3	65	-61±15	0.5±0.40	62
PVAQ : 22±8; 0.50±0.10							
0682328077	SKS	16±16	0.45±0.15	67	8±14.5	0.50±0.125	66
0902240535	SKS	28±10	0.50±0.075	-66	21±8	0.45±0.10	61
PMIC : 73±2; 1.25±0.30							
0902240535	SKS				73±2	1.25±0.30	66
PPAR null with 66							
0682328077	SKS	null	null	64	null	null	66
P001 : -12±5; 1.40±0.20							
0902240535	SKS	-10±4	1.30±0.20	67	-12±.5	1.40±0.20	61
P009 : null with 63							
0682328077	SKS	null	null	58	null	null	65
0902240535	SKS	null	null	66	null	null	61
P012 : -14±7.5; 1.2±0.43							
0902240535	SKS	-14±22.5	1.20±1.20	60	-14±7.5	1.20±0.43	65
P013 : null with 65							
0682328077	SKS	null	null	64	null	null	65

Table of measured single event splitting parameters for the PISCO

array.

Appendix B:

Additional Maps of the Area

of the Bolivia Orocline
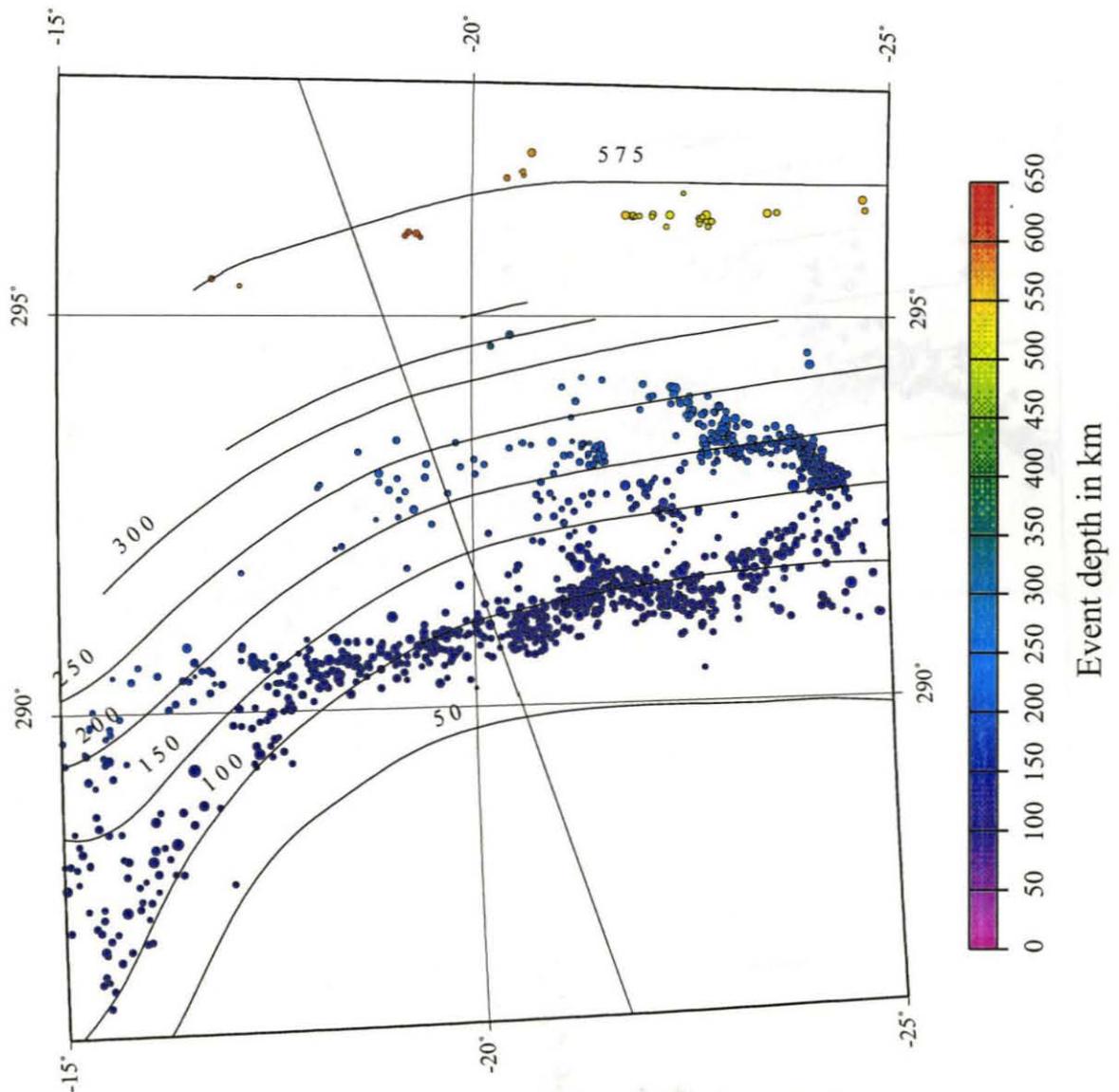
Figure B1: Map with the relocated earthquakes deeper than 100 km

from the catalog of Engdahl et al.. (1998).
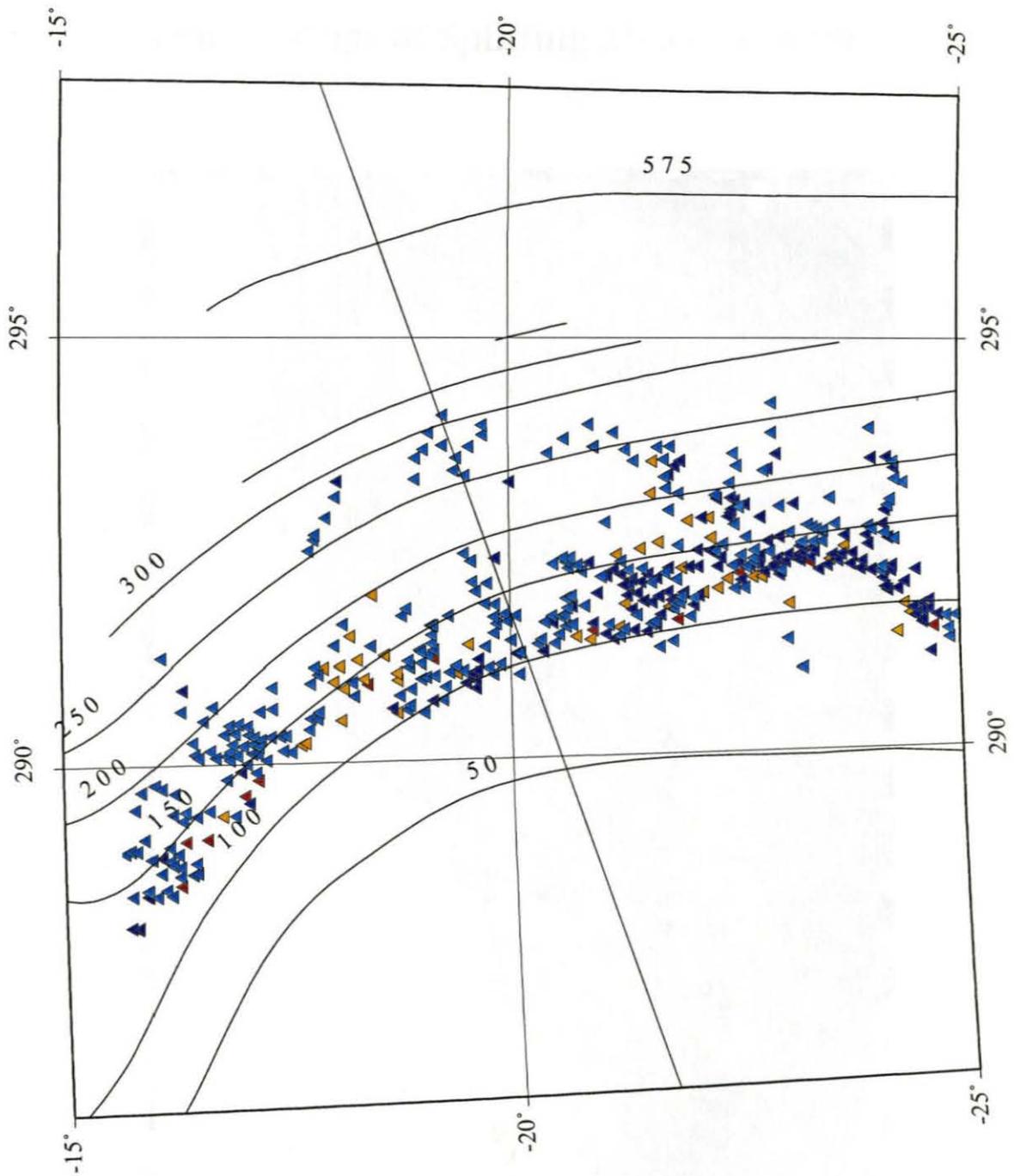
Figure B2: Map of volcanoes. Red color indicates active volcanoes, orange, holocene centers, light blue are "younger" appearing centers on Landsat TM and dark blue are "older" appearing centers on Landsat TM.

Appendix C:

Detailed Maps of Splitting Measurements
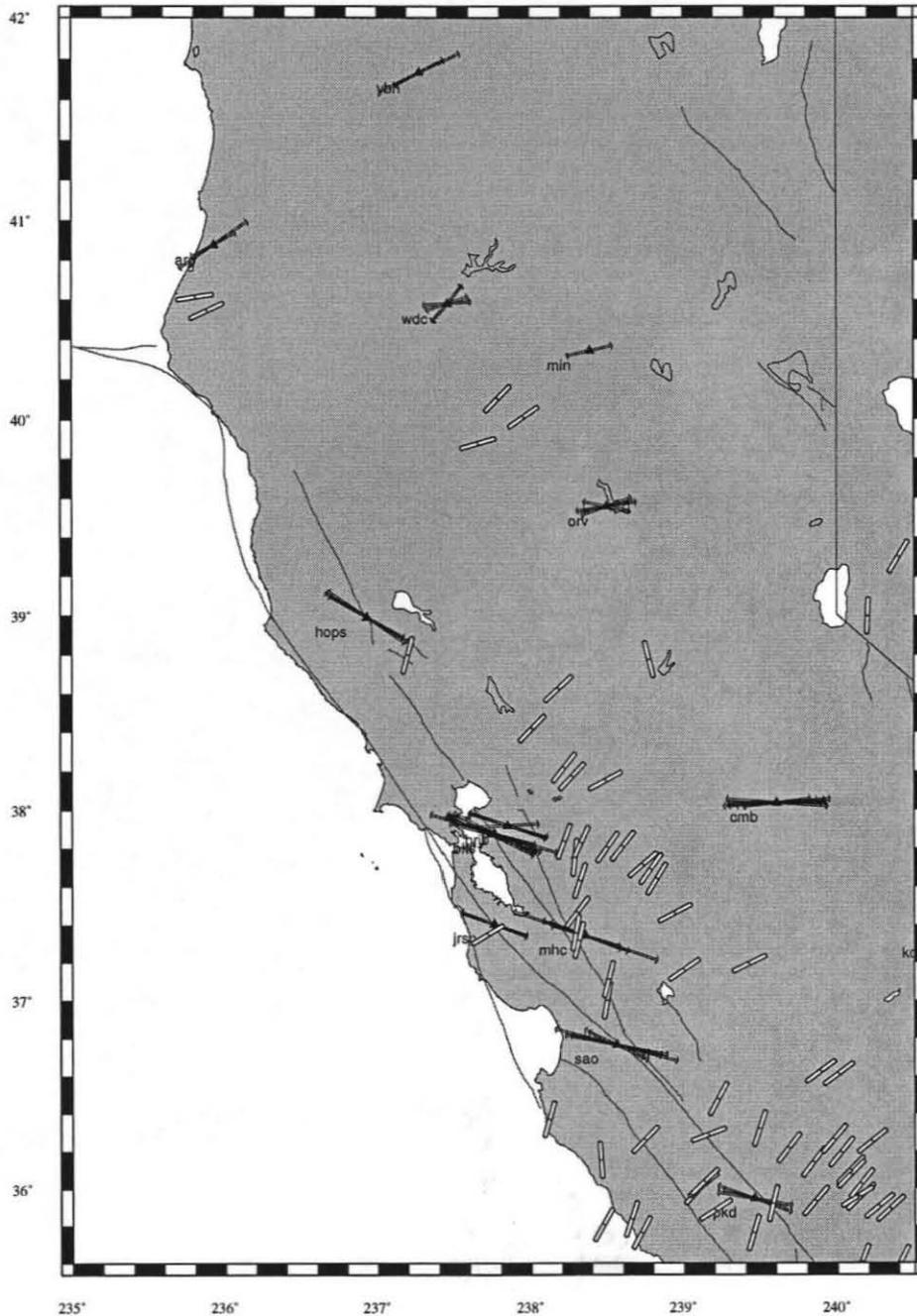
Figure C1: Northern California area splitting measurements and WSM

stress indicators. Symbols as in Figure 4 (Chapter 3).
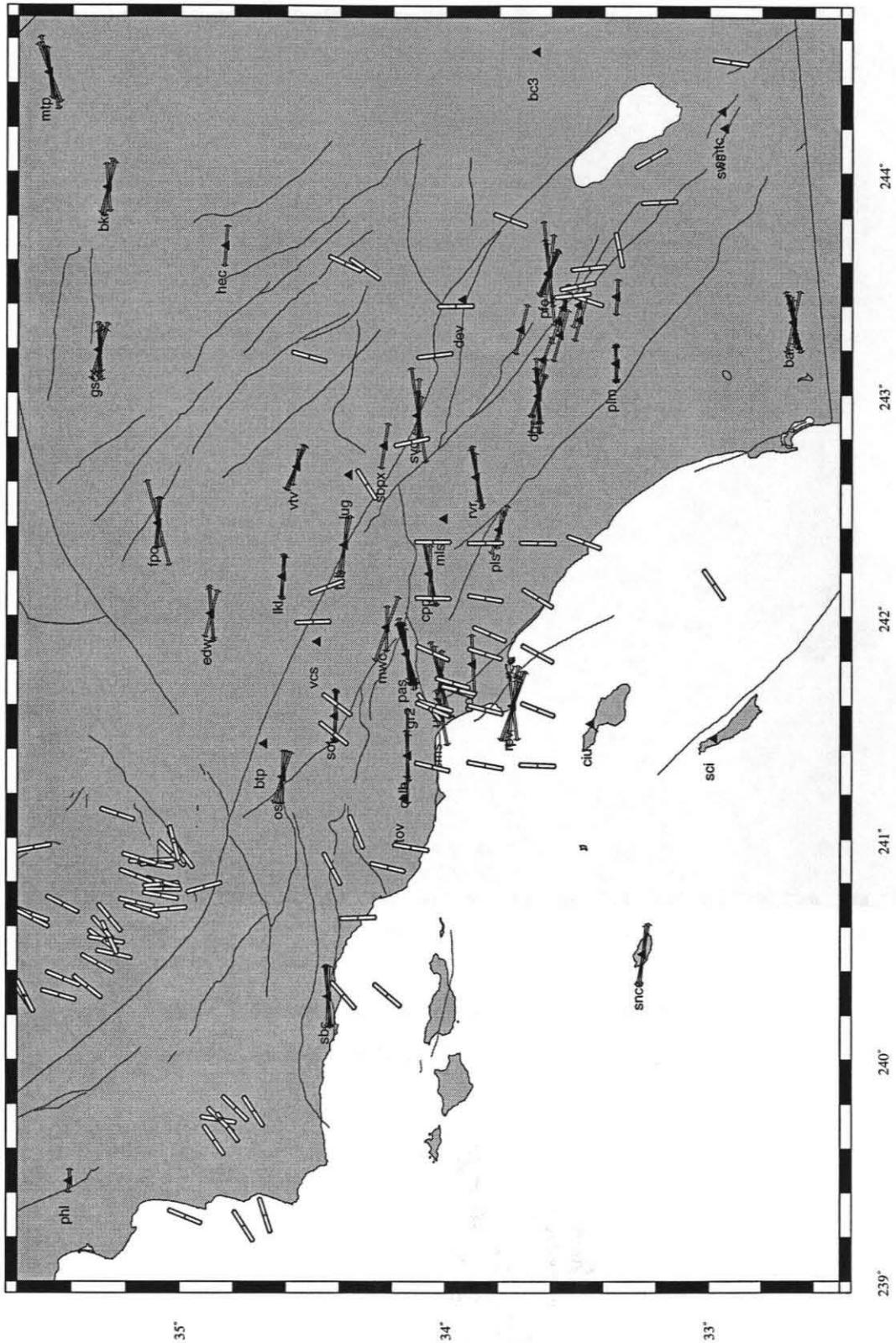
Figure C2: Southern California area splitting measurements and WSM stress indicators. Symbols as in Figure 4.
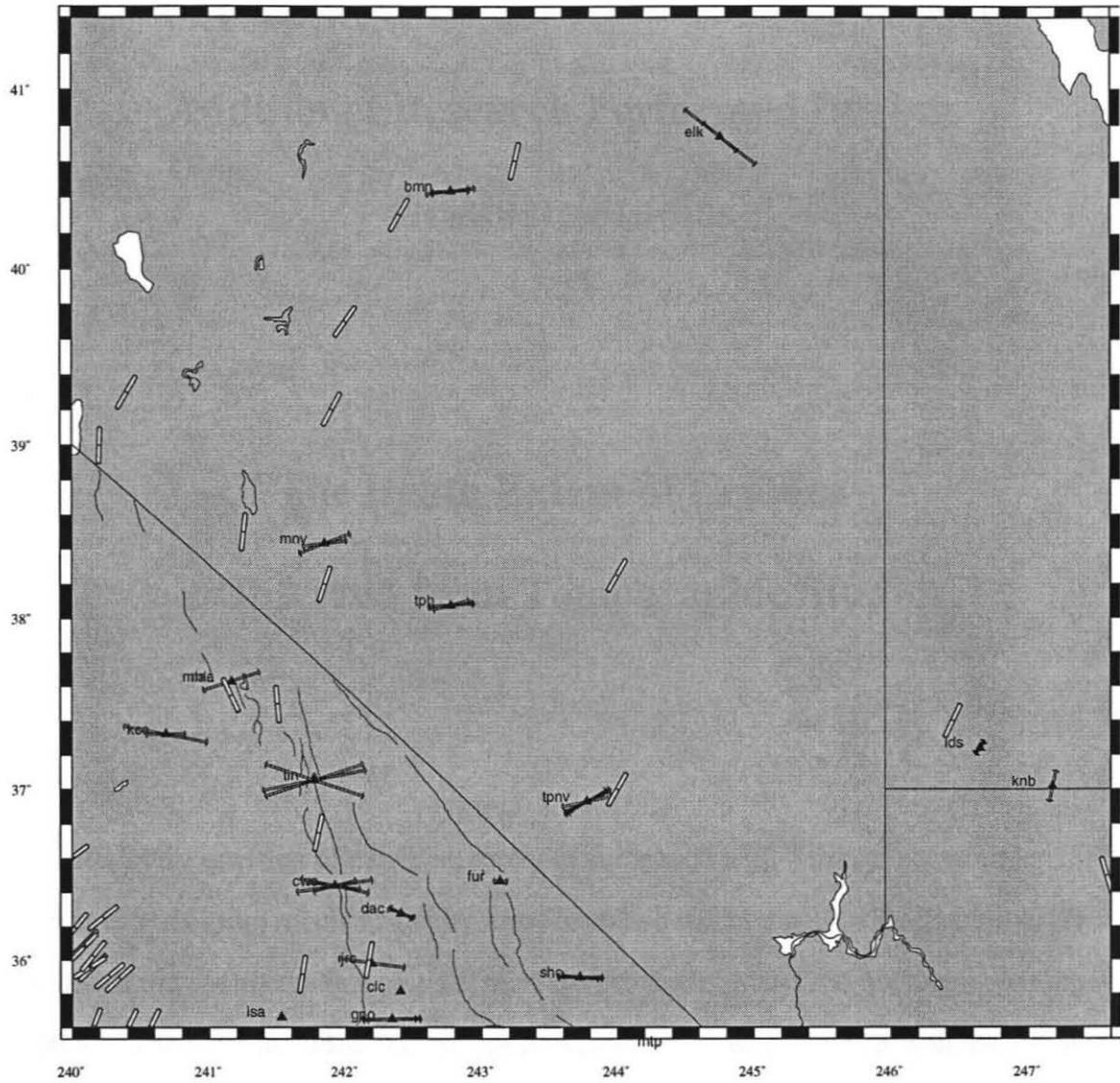
Figure C3: Eastern area splitting measurements and WSM stress indicators. Symbols as in Figure 4.

Additional Research Performed During Graduate Studies

I.

The Depth Extent of Cratons

as Inferred from Tomographic Studies

Abstract

We address the question of the depth extent of the mantle high-velocity zones under ancient cratons using seismic velocity maps from two recent mantle tomographic studies. We divide old continents into two different age provinces, 800-1700 Ma and older than 1700 Ma. The areas included in these age provinces are cross-correlated with the tomography at different depths to quantify the global occurrence of high-velocity anomaly (HVA) extensions beneath cratons. There are statistically significant HVAs underlying the oldest cratons down to a depth of 250 km. There is no significant consistent correlation between tomography and the areas of the younger cratons. The different cratons of the older age province are shown to have correlated HVAs extending to depths varying from less than 100 km to 450 km deep. An in-depth study of the North American shield shows that there is no significant difference in the average velocity anomaly beneath the Early Proterozoic and the Archean part of the shield, whereas the Middle Proterozoic part does not contain any statistically significant HVA. The mantle under Early Precambrian crust is distinctly

different from mantle elsewhere. We propose two different hypotheses to explain these results: I. cratons of Early Proterozoic age or older contain ancient and deep physically attached roots, or II. these cratons contain a small 'permanent' physical root which induces cold downwellings beneath it. A root thickness of about 200 km can be explained by an FeO-poor, olivine-rich mineralogy, while a requirement of high-strength probably demands, in addition, a volatile-poor composition. Different root depths for cratons of similar age may be related to their location in the various supercontinents in which they were involved, and their subsequent deformational history, or they may represent different snapshots in time of transient 'roots', such as thermal boundary layers.

Reference

Polet, J. and D.L. Anderson, Depth extent of cratons as inferred from tomographic studies, Geology, 23, 205-208, 1995.

II.

Automated CMT Inversion

Using Long Period Surface Waves

We automatically determine source mechanisms of earthquakes using long period (150-350 sec) surface wave data. This automatic process is initiated when e-mail from the NEIC is received, which gives the origin time and hypocenter of an earthquake. The data for two stations (Pasadena (PAS) and Columbia (CMB)) is obtained through continuous

telemetry to the Seismo Lab. Additional waveform data is retrieved through the SPYDER-system (IRIS DMC). As soon as three-component data for at least five stations has become available, the source mechanism of the event is determined (following the method by Kawakatsu, JGR 94, 1989). This solution is automatically distributed through e-mail and is put on the worldwide web (*http://www.gps.caltech.edu/~polet/autoCMT.html*) This method has been successfully applied since June 1995. Usually the CMT solution is deter-mined within 3 hours after the occurrence of an event. Since these solutions are determined using long period surface waves, source mechanisms for earthquakes with magnitudes greater than 6.5 are especially well determined, even with the minimum allowed amount of data (five three-component seismograms). In the future we hope to be able to determine the approximate origin time and location of events greater than 6.5 or so within the Seismo Lab with a teleseismic "Gutenberg" program, with sufficient accuracy to enable a faster determination of reliable source mechanisms. This would be done using the continuous datastream available for several TERRAscope stations as well as CMB.

Reference

Polet, J. and H. Kanamori, Automated CMT inversion using long period surface waves, Fall AGU abstract volume, 1995.